X-ray absorption studies on lithium manganese oxide thin films deposited by atomic layer deposition

Heta-Elisa Nieminen

M. Sc. Thesis

Thin Films and Other Nanostructured Materials

Department of Chemistry

University of Helsinki

09 / 2018

HELSINGIN YLIOPISTO
HELSINGFORS UNIVERSITET
UNIVERSITY OF HELSINKI
MATEMAATTIS-LUONNONTIETEELLINEN TIEDEKUNTA
MATEMATISK-NATURVETENSKAPLIGA FAKULTETEN
FACULTY OF SCIENCE

Tiedekunta – Fakultet – Faculty Faculty of Science	Koulutusohjelma – Utbildningsprogram – Degree programme Chemistry	
Tekijä – Författare – Author Heta-Elisa Nieminen		
Työn nimi – Arbetets titel – Title X-ray absorption studies on lithium manganese oxide thin films deposited by atomic layer deposition		
Työn laji – Arbetets art – Level M.-Sc. Thesis	Aika – Datum – Month and year 09/2018	Sivumäärä – Sidoantal – Number of pages 96

Tiivistelmä – Referat – Abstract

Lithium ion batteries (LIBs) are used as power sources in most of portable devices, electronic cars and many other applications today. As the industry demands for smaller devices, new focus has raised for nanostructured electrodes and all solid state batteries. LIBs are rechargeable batteries, which means that Li^+-ions migrate between anode and cathode reversibly. For the battery to work, the electrodes need to be stable when Li^+-ions are intercalated and removed from the structure. $LiMn_2O_4$ is a promising material for a cathode, because the three-dimensional manganese oxide network enables intercalation of additional lithium ions also beyond the 1:1 Li:Mn stoichiometry resulting in structures in the range of $Li_xMn_2O_4$, $0 \leq x \leq 2$. The non-stoichiometric behavior improves the specific capacity of the battery compared to other possible lithium intercalation cathode materials like $LiCoO_2$ and $LiNiO_2$.

Atomic layer deposition (ALD) is a gas phase thin film deposition technique where the precursors are led to react on the surface one by one. Because no chemical reaction is taking place in the gas phase, the film growth is highly controllable and the resulting films have excellent purity and high uniformity and conformity. ALD is superior thin film deposition technique even on top of 3D structures and when depositing ultra-thin films. This makes it excellent technique to deposit electrode materials for LIBs.

X-ray absorption spectroscopy (XAS) measures the absorption of the material as a function of x-ray energy. With a tunable light source it is possible to study a selected electron core shell of a specific element. XAS gives then information on the electronic structure as well as the local crystal structure of the selected atom in the material. Therefore, XAS is an excellent technique for studying the intercalation and de-intercalation processes of $LiMn_2O_4$.

The literature part of this thesis describes the synthesis of $LiMn_2O_4$ thin films and the behavior of the material as a working cathode in LIB. The focus is especially on XAS studies on $LiMn_2O_4$. The experimental part involves a study on ALD grown β-MnO_2 and $Li_xMn_2O_4$, $0 \leq x \leq 1$, thin films with XAS, X-ray diffraction (XRD), X-ray reflectivity (XRR), time-of-flight elastic recoil detection analysis (TOF-ERDA), residual stress measurements and X-ray photoelectron spectroscopy (XPS). The aim of the study was to define how and where Li^+ -ions intercalate in the β-MnO_2 structure. To clarify the intercalation process, K and L core shells of manganese and K core shell of oxygen were studied with XAS. Samples were prepared at 225 ˚C by using earlier known ALD processes. First β-MnO_2 film was deposited and then lithium was added by pulsing LiO^tBu and H_2O alternately on to the β-MnO_2 film. The films were annealed after the deposition, however the lithium intercalation was observed to start already during the $LiO^tBu - H_2O$ pulsing sequence. For the lithium intercalation mechanism, it is proposed that in the beginning the Li^+-ions penetrate only to the top part of the β-MnO_2 film and a lithium deficient non-stoichiometric phase $Li_xMn_2O_4$, $0 < x < 0.5$, is formed. When the lithium concentration exceeds $x \approx 0.5$ in $Li_xMn_2O_4$, the phase changes from the tetragonal pyrolusite to the cubic spinel, which enables Li^+-ions to migrate throughout the whole film. Annealing in air after deposition seemed to convert the phase completely to the pure cubic spinel $LiMn_2O_4$.

Avainsanat – Nyckelord – Keywords
Lithium ion battery, LIB, Atomic layer deposition, ALD, X-ray absorption spectroscopy, XAS, thin film, lithium manganese oxide, intercalation

Säilytyspaikka – Förvaringställe – Where deposited
E-thesis

Muita tietoja – Övriga uppgifter – Additional information

Contents

Abbreviations

2θ	Angle between incident beam and detector
$2\theta_{\alpha}$	Angle between $2\theta_{\beta}$ and detector
$2\theta_{\beta}$	Azimuthal angle
$2\theta_{\chi}$	In-plane 2θ measurement
ALD	Atomic layer deposition
acac	Acetylacetonate
BB	Bragg Brentano focusing optics
CBD	Chemical bath deposition
CVD	Chemical vapor deposition
d	Sample thickness
DOS	Density of states
E_s	Young's modulus of a substrate
EXAFS	Extended x-ray absorption fine structure
FE-SEM	Field emission scanning electron microscopy
$\hbar$	Planck's constant
HZB	Helmholtz-Zentrum Berlin
I_o	Intensity of the incident beam
IS	Ionized sputtering
I_t	Intensity of the transmitted beam

JT effect	Jahn-Teller effect
Li(thd)	2,2,6,6-trimethyl-3,5-heptanedionato lithium(I)
LIB	Lithium-ion battery
LiO^tBu	Lithium tert-butoxide
MBE	Molecular beam epitaxy
m_e	Mass of an electron
$(MeCp)Mn(CO)_3$	Methylcyclopentadienyl manganese(I) tricarbonyl
$Mn(CpEt)_2$	Bis(ethylcyclopentadienyl)manganese(II)
$Mn(thd)_3$	Tris(2,2,6,6-tetramethyl-3,5-heptanedionato)manganese(III)
MS	Magnetron sputtering
MSS	Molten salt synthesis
NEXAFS	Near edge x-ray absorption fine structure
PA-ALD	Photo-assisted atomic layer deposition
PE-ALD	Plasma-enhanced atomic layer deposition
PEG	Polyethylene glycol
PGM	Planar grating monochromator
PLD	Pulsed laser deposition
PSA	Parallel slit analyzer
PSC	Parallel slit collimator
PTB	Physikalisch-technische Bundesanstalt

PVD	Physical vapor deposition
q	Photoelectron wavenumber
R_0	Radii of curvature of the substrate before thin film deposition
R_1	Radii of curvature of the substrate after thin film deposition
RF	Radio frequency
SC	Scintillator counter
SP	Spray pyrolysis
TEY	Total electron yield
t_f	Thickness of the thin film
TFY	Total fluorescence yield
TOF-ERDA	Time-of-flight elastic recoil detection analysis
t_s	Thickness of the substrate
V	Cation vacancy in lithium manganese oxide structure
ν_s	Poisson's ratio of the substrate
XANES	X-ray absorption near edge structure
XAS	X-ray absorption spectroscopy
XPS	X-ray photoelectron spectroscopy
XRD	X-ray diffraction
XRR	X-ray reflection
$\Delta\Omega$	Solid angle

ε	Photon energy
$\mu(\varepsilon)$	Absorption coefficient
$\mu_0(\varepsilon)$	Absorption coefficient for free atoms
$\mu_\chi(\varepsilon)$	Absorption coefficient for atoms in a lattice
σ_f	The stress in thin film
$\chi(q)$	Quantity that describes the absorption process
ω-scan	Rocking-curve measurement
ω_κ	Angular frequency of the photon beam

1 Introduction

Lithium ion batteries (LIBs) are used as power sources in a wide range of applications today. LIBs are providing power for transport in electronic and hybrid cars and bicycles, and in portable devices like laptops, smartphones and tools. New focus has raised from small scale microbatteries as the industries demands smaller devices. This has led to a development of new concepts for lithium ion batteries like nanostructured electrodes and all solid state devices.

$LiMn_2O_4$ is a promising candidate for cathode material in LIBs. It has an ability to intercalate lithium ions reversibly through its three dimensional manganese oxide network. $LiMn_2O_4$ has therefore higher specific capacity compared to layered structures. The material is also non-toxic and relatively cheap and easy to synthesize. The challenge with $LiMn_2O_4$ is that the material experiences capacity fading rather easily. Fundamental understanding of the intercalation process of lithium ions may help to overcome the disadvantage of the material.

All solid state batteries require thin film deposition of the cathode material, for example $LiMn_2O_4$. One of the promising techniques for depositing $LiMn_2O_4$ is atomic layer deposition (ALD). ALD is a gas phase deposition technique where the precursors are led to react on the surface one by one. The reaction occurs only between the precursor gas molecules and the adsorbed surface molecules so that ideally new atomic or molecular layers are formed one at a time. The self-limiting surface reactions make the thickness of thin films highly controllable even to atomic scale. Because the precursors are supplied alternately and no chemical reaction is taking place in the gas phase, the films have excellent purity and they grow on top of 3D structures with high uniformity and conformity. This makes ALD a good technique to deposit thin films for solid state batteries.[1,2]

X-ray absorption spectroscopy (XAS) is an excellent technique for studying the intercalation and de-intercalation processes of $LiMn_2O_4$. With XAS it is possible to get information on the electronic structure as well as the local crystal structure of a specific element in a material. Usually the K and L core shells of transition metal and the L core shell of oxygen are studied for transition metal oxides. XAS measurement gives altogether element specific detailed information about the atom itself and also about the number and arrangement of the neighboring atoms.

This thesis describes $LiMn_2O_4$ as a material and especially XAS studies on the intercalation/de-intercalation process in a working cathode in batteries. In the experimental part, the local and electronic structure of manganese together with electronic structure of oxygen are studied at various stages of the intercalation process for $LiMn_2O_4$ thin film grown by ALD.

Literature review

2 Lithium-ion batteries

A typical lithium-ion battery consists of two electrodes (anode and cathode) and an organic electrolyte in between (Figure 1). The electrodes are usually a carbonaceous anode and a transition metal oxide cathode. Lithium ion batteries are rechargeable i.e. secondary batteries.

In a fully charged battery, lithium ions are on the anode and when the battery is discharging the ions migrate to the cathode. When the battery is recharging the same process occurs vice versa. Electric energy is released and stored during the reversible cycles. The electrochemical reactions that take place on the anode and $LiMn_2O_4$ cathode are in Figure 1.[3-5]

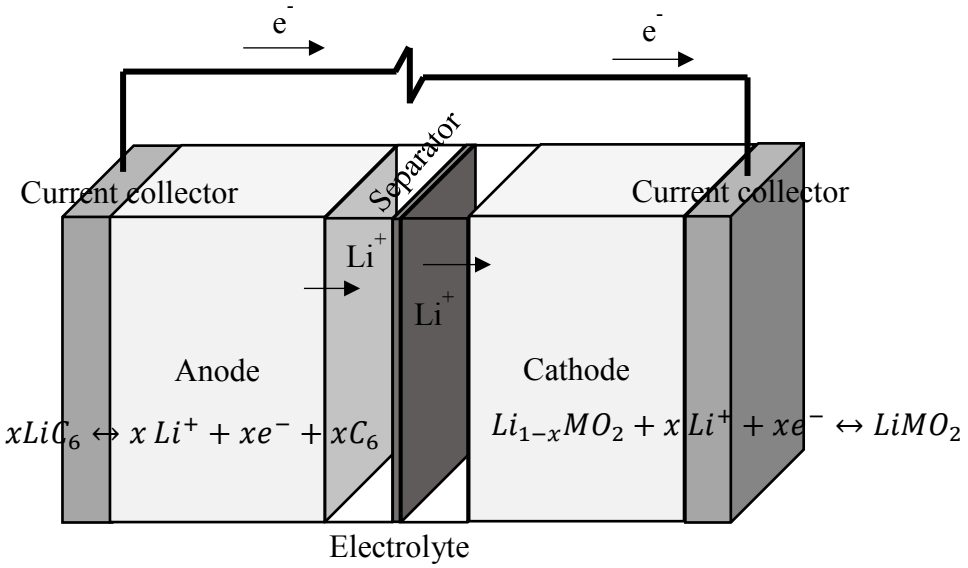

Figure 1. A schematic presentation of a discharging lithium ion battery.

An all solid state lithium-ion battery works in principle in the same way as a traditional LIB. The difference is that the electrolyte is also a solid material. Without liquid the batteries are believed to have longer cycle life, higher energy density, lower cost and smaller size compared to the traditional liquid-electrolyte LIBs. The solid state batteries are also safer

because they are non-flammable. One of the challenges in the solid state batteries relates to the effectiveness of the electrode-electrolyte interface and the fundamental understanding of the interfacial as well as the intercalation processes during the charge and discharge.[6]

Lithium is a prior element for batteries, thanks to its high specific capacity and low electronegativity, which can lead to high voltage cells and further on to high energy density batteries. Li metal was first used as an anode in the LIBs, but because of the safety issues alternative options for anodes were searched. A good alternative for Li metal is a material that can irreversibly intercalate Li-ions. Materials that contain carbon are commonly used anode materials nowadays. That is because carbon is said to have the best combination of a good cycling behavior and a large specific capacity.[7-9]

Lithium intercalating anodes however need strongly oxidizing positive cathode. Such cathode materials are for example $LiCoO_2$, $LiNiO_2$ and $LiMn_2O_4$. $LiMn_2O_4$ is a prior material compared to the other two, because $LiMn_2O_4$ has an ability to intercalate second lithium ion forming a $Li_{1+x}Mn_2O_4$ structure and also an ability for lithium extraction to form a $Li_{1-x}Mn_2O_4$ structure. The non-stoichiometric behavior improves the specific capacity of the battery by 10 % compared to the other two materials. Manganese is also abundant and the synthesis of bulk $LiMn_2O_4$ is easy, which lower the costs of the electrodes.[9,10] Because of the promising properties of $LiMn_2O_4$ as a cathode, the material is under a lot of investigation for thin film solid state batteries. The intercalation process of lithium to manganese oxide sheds fundamental understanding of the working principle of the $LiMn_2O_4$ cathode material.

3 Spinel $LiMn_2O_4$

The reversible lithium exchange is a must have property for LIBs to work. For $LiMn_2O_4$ this means that the [Mn – O] framework cannot collapse even when Li^+ is removed from the structure. Because manganese can form a variety of oxides and Li^+ ion is highly mobile small ion, the structure of $Li_xMn_2O_4$, $0 < x < 2$, can be rather complex.

The stoichiometric $LiMn_2O_4$ has a cubic spinel structure (Figure 2). It crystallizes in a space group Fd3m. The lithium ions have oxidation state +1 and the average oxidation state of manganese ions is +3.5, meaning that the structure has 1:1 relation of Mn^{3+} and Mn^{4+} ions. The large oxygen anions arrange in a cubic closed packed structure leaving two possible

interstitial sites to the metal cations. The sites are denoted by the Wykoff symbols as tetrahedral 8a and octahedral 16d.[11] In the stoichiometric cubic spinel $LiMn_2O_4$ the lithium ions occupy the 8a sites and are hence tetrahedrally coordinated. The manganese cations fill the 16d sites and are octahedrally coordinated.

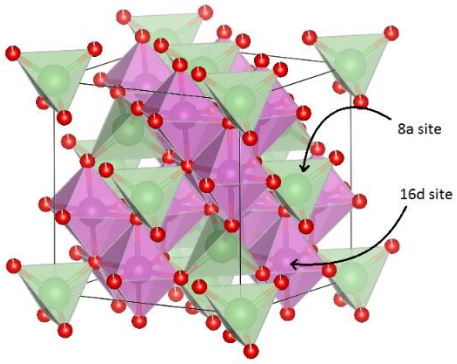

Figure 2. The cubic spinel structure of $LiMn_2O_4$. The red atoms represent oxygen, the green atoms in tetrahedrons are lithium and purple inside octahedrons are manganese. The 8a and 16d interstitial sites are presented.

The spinel lithium manganese oxide compounds have several stable phases in air. Figure 3 is a phase diagram of the spinel Li-Mn-O system. In addition to the stoichiometric cubic spinel $LiMn_2O_4$, the structure can be lithium deficient or it can have an excess amount of lithium $Li_{1\pm x}Mn_2O_4$ ($0 < x$), it can be cation mixed $Li[Li_xMn_{2-x}]O_4$ ($0 < x < 1/3$), manganese rich $Li_{1-x}Mn_x[Mn_2]O_4$ ($0 < x < 0.1$) or manganese deficient $LiMn_{2-x}O_4$ ($x = ¼$). The oxygen may take part on balancing the charge when lithium is migrating, resulting in an oxygen deficient phase $Li_{1+x}Mn_{2-x}O_{1-\delta}$.[12-14]

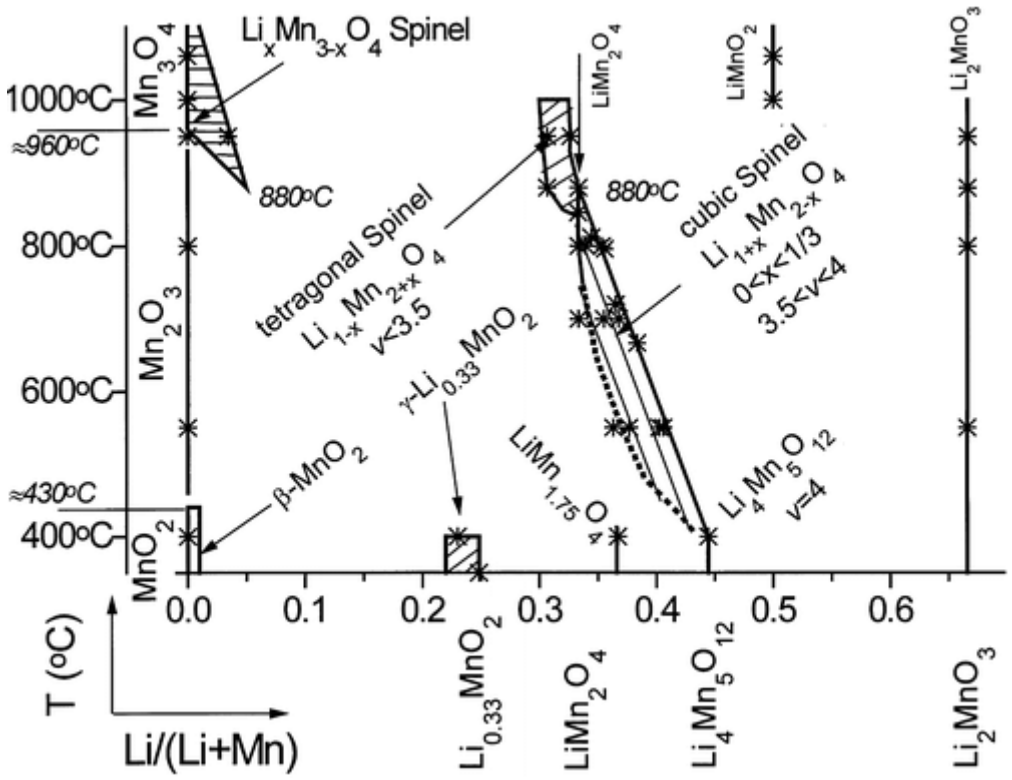

Figure 3. A phase diagram f a spinel Li-Mn-O system. Reprinted with permission from Chemistry of Materials, Vol. 11, J.M. Paulsen, J.R. Dahn, Phase diagram of Li−Mn−O spinel in air, pages no. 3065. Copyright 1999 American Chemical Society.

3.1 Lithium insertion to different manganese oxides

Manganese forms compounds at every oxidation state between -3 and +7. The most common oxidation states are +2, +3 and +4. All of these appear as oxides: MnO, MnO_2, Mn_2O_3 and Mn_3O_4. From the LIB point of view few manganese oxides have good enough cyclability for being a cathode material in batteries. The major challenge for the manganese oxides is to prevent the structure from collapsing even when lithium is extracted.

MnO_2 has at least six different crystal structures: α-MnO_2, β-MnO_2, γ-MnO_2, δ-MnO_2, λ-MnO_2 and ε-MnO_2 all of which lithium has been intercalated to.[15-17] Figure 4 presents the structures of MnO_2 phases. The missing λ-MnO_2 is a result of removing lithium from spinel $LiMn_2O_4$ without breaking the Mn_2O_4 framework. The additional atoms in between the layers in the δ-MnO_2 are sodium, calcium or potassium.

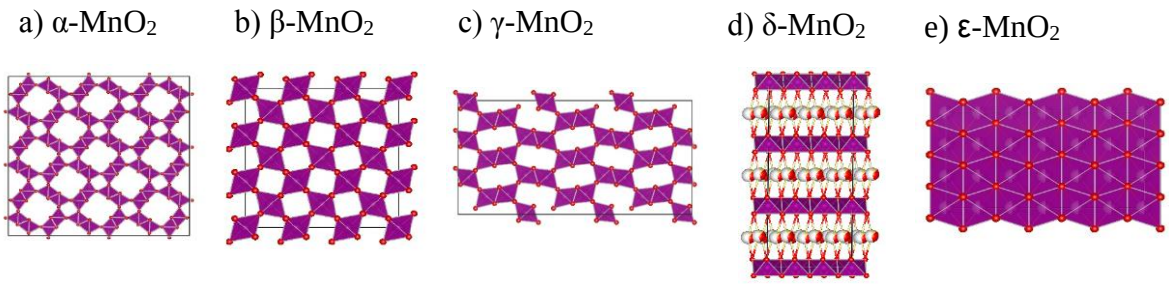

Figure 4. The crystal structures of various MnO_2 phases.

α-MnO_2 is able to intercalate a significant amount of lithium through its (2 x 2) channels. However, the cycling performance of this phase is rather poor. The framework of α-MnO_2 collapses because the manganese and oxygen ions displace into the diffusion channels to stabilize the structure. To prevent from collapsing, α-MnO_2 can be doped with cations, like Ba^{2+}, K^+ and Na^+ or water and the lithium intercalation takes place through ion exchange reactions.[13]

Lithium ions can enter to the square channels in the rutile structure of β-MnO_2. The phase cannot store significant amount of lithium, but it undergoes a phase change to spinel [Mn_2O_4] framework quite rapidly. The initial interstitial site of entered Li^+ is sharing edges with Mn^{3+} ions, which causes a strong repulsive force. If the cations transform to cubic close backed structure, the sites are only sharing corners. This is energetically favorable and the driving force for the rutile-spinel transformation.[13,18]

γ-MnO_2 consist of domains that resemble β-MnO_2 and ramsdellite structure. It has (1 x 1) and (2 x 1) channels that are able to intercalate lithium. The preparation methods of γ-MnO_2 however usually leave some water into the structure and it must be removed by heating. If the γ-MnO_2 contains mostly the ramsdellite-MnO_2 structure, it can intercalate more lithium. The heating that removes the water increases the β-MnO_2 parts and hence decreases the cycling ability of γ-MnO_2. Lithium intercalation causes also the structure to swell anisotropically which is too severe change for prolonged electrochemical cycling.[13]

ε-MnO_2 phase is said to have the highest potential for lithium intercalation due to the ideal interstitial features of the structure.[19] However, the layered structure collapses if it loses all the interstitial atoms and hence the capability to cycle lithium is usually poor. That is why ε-MnO_2 are not often interesting for lithium battery applications.[13]

3.2 Jahn-Teller distortion

Jahn-Teller effect (JT effect) means the geometrical distortion of a molecule or ion when it removes its ground state energy degeneracy. This geometrical distortion lowers the overall energy of the molecule. Jahn-Teller theorem says that the effect occurs in any structure that has spatially degenerate energy states. In spinel $LiMn_2O_4$ the Mn^{3+} ions are Jahn-Teller active and Mn^{4+} ions are not. This means that the Mn^{3+}-O bonds stretch and distort the cubic structure of $LiMn_2O_4$.[20]

$LiMn_2O_4$ has a 1:1 critical balance of the active and non-active JT ions so a possible phase change from the cubic to tetragonal structure occurs already when cooling down from around 10 °C.[14,21-26] The low temperature phase is a bit controversial though, since changes to tetragonal $I4_1/amd$[14,21,23,25] and orthorhombic Fddd[22,24,26-28] have been detected.

The JT activity of Mn^{3+} ions is said to be one of the main reasons for the capacity fading in the $LiMn_2O_4$ cathode material in LIBs. If the material contains tetragonal or orthorhombic parts, Li^+ ions cannot intercalate into the structure using the same pathways as in the phase-pure cubic spinel. The effect has been suppressed for example by coating or doping $LiMn_2O_4$ powder.[29,30]

4 Synthetization of $LiMn_2O_4$

4.1 Powders

Powder synthetization techniques are divided to mechanical methods and chemical methods. A common factor for powder synthesis throughout all techniques is that to obtain homogeneous $LiMn_2O_4$ an excess amount of lithium containing source is mixed compared to manganese source. This is needed to prevent lithium deficient compositions. In this thesis powder synthetization is discussed briefly and the main focus is set to the thin film deposition in the following section.

Mechanical synthetization methods include solid state reactions and ball milling. Phase pure spinel $LiMn_2O_4$ powder has been synthesized with solid state reaction from Li_2CO_3[ref. 31-33] with MnO_2[ref. 31,32] and $Mn(CH_3COO)_2$[ref. 33], from $LiNO_3$[ref. 32,34] with MnO_2[ref. 32] and

$Mn(CH_3COO)_2$[ref. 34] and from LiOH[ref. 35] with $Mn(CH_3COO)_2$[ref. 35]. The mixtures were calcined at 500 – 800 °C for several hours with some intermittent grinding to improve the properties of the $LiMn_2O_4$ powder.[31,34] The $LiMn_2O_4$ powder was synthesized with ball milling from Li_2CO_3 and MnO_2[ref. 36] as well as from $Li_2C_2O_4$ and $Mn(CH_3COO)_2$[ref. 37] and Li_2O_2 and Mn_2O_3[ref. 38,39] powders. The synthetizations were made at 300 – 900 °C in air.

Chemical synthetization methods include sol-gel, Penchini, sonochemical and microwave assisted method as well as molten salt synthesis (MSS), hydrothermal synthesis, chemical bath deposition (CBD), combustion and spray pyrolysis (SP). All of the chemical preparation methods result to a phase pure spinel $LiMn_2O_4$.

The $LiMn_2O_4$ powder was synthesized with sol-gel method using $Li(CH_3COO)$[ref. 40-46], LiOH[ref. 47-49] or $LiNO_3$[ref. 50,51 or Li_2CO_3[ref. 52] as a lithium source together with $Mn(CH_3COO)_2$[ref. 40-50] or $Mn(NO_3)_2$[ref. 51,53] as manganese source. The synthetizations were made in 100 – 200 °C and post-synthesis annealing was performed in all synthesis methods. Pechini method is a variation of a sol-gel technique. The method uses polymer matrix to obtain oxide materials with extremely small particle size. The $LiMn_2O_4$ has been synthesized by Pechini method from $LiNO_3$ and $Mn(CH_3COO)_2$.[54]

A manganese sources MnO_2[ref. 47,55,56] and $Mn(NO_3)_2$[ref. 57-59] have been used with lithium sources Li_2CO_3[ref. 55] and $LiNO_3$[ref. 57] in microwave assisted method and with LiOH[ref. 47,56,58,59] in hydrothermal synthesis. $LiNO_3$[ref. 60-62], LiOH[ref. 63] and Li_2CO_3[ref. 64] have been used as lithium sources also in SP together with variety of manganese compounds; $MnCO_3$[ref. 63], $Mn(NO_3)_2$[ref. 60,62] and $Mn(CH_3COO)_2$[ref. 61,64]. $LiMn_2O_4$ was synthesized with MSS from eutectic mixture of LiCl, Li_2CO_3 and $Mn(CH_3COO)_2$[ref. 65] or LiCl, Li_2CO_3 and $MnCl_2$[ref. 66]. $Li(CH_3COO)$ and $Mn(CH_3COO)_2$ were the sources in CBD and in combustion method of $LiMn_2O_4$.[ref. 67,68] $LiMn_2O_4$ has been done also from $LiNO_3$ and $Mn(NO_3)_2$[ref. 69,70 and Li_2CO_3 and $MnCO_3$[ref. 71] with combustion synthesis.

Other than spinel phase $LiMn_2O_4$ powders have also been prepared. For example tetragonal $LiMn_2O_4$ nanoparticles were done with sonochemical method by first coating Mn_3O_4 nanoparticles with LiOH. $LiMn_2O_4$ nanoparticles were obtained after calcination of LiOH-Mn_3O_4 particles.[72] Truncated octahedral $LiMn_2O_4$ powder was synthesized from $LiNO_3$ and $Mn(NO_3)_2$ with calcination process.[73]

4.2 Thin films

$LiMn_2O_4$ thin films have been prepared with a variety of techniques, which are in this thesis divided to liquid phase methods, gas phase physical vapor deposition (PVD) and chemical vapor deposition (CVD) techniques. In PVD methods the material which will be deposited already exists, while in CVD methods the material does not exist previously, but is synthesized during the process from gaseous precursors.

4.2.1 Liquid phase methods

4.2.1.1 Sol-Gel

In sol-gel techniques the liquid precursor (sol) gradually transforms to a biphasic liquid/solid system (gel) after poly-condensation reaction. The rest of the liquid phase is removed resulting in a thin film. In a dip-coating technique the substrate is immersed to a sol multiple times with constant speed. After each dip excess liquid drains off and the film deposits itself on the substrate. The remaining solvent is evaporated in between every immersion. In a spin coating technique a small amount of sol is placed on top of a flat substrate. When the substrate is rotated the centrifugal force spreads the sol over the whole substrate and a film is formed.

$LiMn_2O_4$ has been deposited by the sol-gel dip coating and spin coating methods. Usually the precursors used for preparing the sol have been Li(acac)[74,75] (acac = acetylacetonate) or $Li(CH_3COO) \cdot 2H_2O$[(ref. 76-81)] and $Mn(CH_3COO)_2 \cdot 4H_2O$[(ref. 74,76-81)] or $Mn(acac)_2$[(ref. 75)] dissolved in ethanol. The ethanol solution has then been mixed to a solvent which usually has been acetic acid or tartaric acid[81] solution with 1,5-pentanediol[74], 1-butanol[75] or chitosan[76,78,80].

$LiMn_2O_4$ films were deposited on TEC7 FTO glass[74], $Pt/Ti/SiO_2/Si$ with polystyrene 3D microspheres[75] and Pt substrate[81] by dip coating in air at room temperature. The substrate withdrawal speed was 5 – 15 cm/min[74] and 30 – 60 min post deposition annealing was done at 400 °C[74,75].

$LiMn_2O_4$ has been deposited on Pt[76,78,81] and Pt coated silicon[80] substrates with spinning speeds of 2500 – 4000 rpm[76]. The film was then dried at 150 – 350 °C[76] and calcined at 400 – 900 °C[78]. The spinel phase crystallinity was highest for the films that were calcined at 700

°C according to XRD measurements (Figure 5). At higher calcination temperatures XRD showed Mn_3O_4 impurity phase. [78]

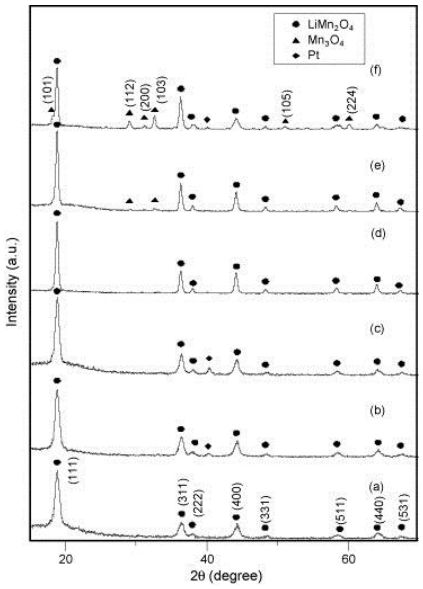

Figure 5. XRD of $LiMn_2O_4$ thin film calcined at different temperatures for 1 h a) 400 °C, b) 500 °C, c) 600 °C, d) 700 °C, e) 800 °C and f) 900 °C. Reprinted from Journal of Power Sources, Vol 159, Fu-Yun Shih, Kuan-Zong Fung, Effect of annealing temperature on electrochemical performance of thin-film $LiMn_2O_4$ cathode, pages 179-185, Copyright 2006, with permission from Elsevier.

4.2.1.2 Electrodeposition

Electrodeposition i.e. electroplating takes place in a three or two electrode system where the film is deposited on a conductive substrate with cathodic reduction reaction from aqueous electrolyte solution. The system contains working electrode, which is the substrate, a counter electrode, which is the source of the metal ions, and a reference electrode.

$LiMn_2O_4$ synthesis was done by first depositing a manganese oxide thin film by electrodeposition and intercalating lithium by dipping the manganese oxide film into 0.03 M LiOH solution and sintering 12 h at 750 °C. The manganese oxide film was electrodeposited on anode Au substrate from $MnSO_4 \cdot 5\ H_2O$ and sulfuric acid solution the pH of which was adjusted to 2.3 at 40 °C. The deposition was done under 1.7 V cathodic polarization by oxidation of Mn^{2+}. The resulting $LiMn_2O_4$ films were composed of 50 nm nanoparticles.[82]

4.2.1.3 Spray Pyrolysis

In spray pyrolysis (SP) the liquid precursor is sprayed to a heated substrate where the particles impact, spread and undergo thermal decomposition to produce a thin film. A precursor liquid is prepared by dissolving $Li(CH_3COO)$[83,84] and $Mn(CH_3COO)_2$[83,84] to deionized water. Methanol[84] or polyethylene glycol (PEG)[83] were added to improve the viscosity of the solution. The PEG acted also as a polymeric complexing agent for combining the cations and as a combustion fuel. The precursor liquid was pulsed at 420 °C to stainless steel substrate with 20s pulses and with 240s intervals[83] or at 320 °C to stainless steel substrate with 15s pulses and 100s intervals[84]. Post-deposition annealing was performed at 450 – 800 °C.

Both processes resulted in a phase pure spinel $LiMn_2O_4$ according to XRD measurements (Figure 6). Post-deposition annealing improved the crystallization so that the peaks in XRD become sharper and more intense. The SEM photograph reveal 400 – 700 nm particle size for the process done with methanol when only around 90.7 nm in the process done with PEG.

a)

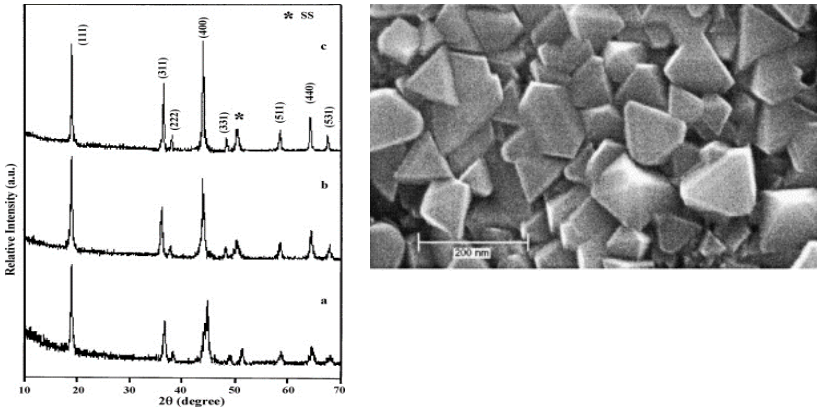

b)

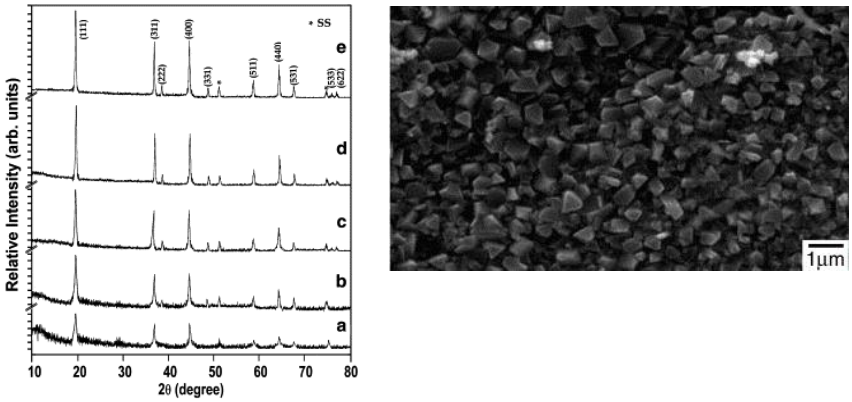

Figure 6. a) XRD diffractogram of $LiMn_2O_4$ thin film prepared with PEG and annealed at (from bottom up) 450, 500 and 600 °C. On the right SEM photograph of $LiMn_2O_4$ thin film annealed at 600 °C. Reprinted from Journal of Alloys and Compounds, Vol. 489, 2, Karthick et al., Nanocrystalline $LiMn_2O_4$ thin film cathode material prepared by polymer spray pyrolysis method for Li-ion batter, pages 674-677, 2010 with permission from Elsevier. b) XRD diffractogram of $LiMn_2O_4$ thin film prepared with methanol (from bottom up) as deposited at 320 °C and annealed at 500, 600, 700 and 800 °C. On the right SEM photograph of $LiMn_2O_4$ thin film annealed at 700 °C. Reprinted from Thin Solid Films, Vol. 516, 23, Subramania et al, Preparation and electrochemical behavior of $LiMn_2O_4$ thin film by spray pyrolysis method, pages 8295-8298, Copyright 2008 with permission from Elsevier.

4.2.2 Physical vapor deposition methods

4.2.2.1 Sputtering

Sputtering is a method where the material is ejected from a target and condensed to a substrate creating a thin film. The material is excluded from the target by bombarding it with ions. The target is negatively charged so it creates a plasma glow. The electrons flow from

the target into the plasma environment, collide with the inert gas atoms and ionize them. After the collision the positively charged gas ions bombard the negatively charged target with very high velocity and sputter off neutral atoms from the target. The sputtered atoms transfer and condense on a substrate.

Magnetron sputtering (MS) uses a magnetic field to catch electrons from the target and trap them onto circular paths. The process increases the ionization efficiency and hence the deposition rate. Radio frequency (RF) sputtering uses an electrical potential alternating at radio frequency. The alternating electrical potential prevents a charge build up on the target which could terminate the deposition process. If the deposition conditions are modified in a way that the system creates a second plasma region in between the target and a substrate, the sputtered atoms can ionize on their way to the substrate. This method is called ionized sputtering (IS).

Polycrystalline $LiMn_2O_4$ thin films have been deposited with MS and IS from pure $LiMn_2O_4$ target to Ti/Si(100) and stainless steel substrates at 130 °C. The film was deposited at 1.3 Pa Ar pressure. Post-deposition annealing was done at 600 °C for 1 h in air.[85]

Phase pure spinel $LiMn_2O_4$ thin film has been deposited with RF sputtering by using always a $LiMn_2O_4$ target with 80 – 120 W[86,87] rf power. The depositions have been made on silicon[86-90], stainless steel[86-88,90], Al[(ref. 89)], $Si/SiO_2/Ti/Au$[(ref. 91)], $Si/TiN/SiO_2/Pt$[(ref. 92)] substrates with Ar[(ref. 87,88,90,92)] or O_2/Ar[(ref. 89,91)] as the working gas. The substrate temperatures varied from 200 to 400 °C and depositions on a substrate at room temperature have been made as well.[89] Films were often annealed after the deposition.

In addition to annealing, some films were treated in an oxygen plasma to modify the surface morphology and to enhance capacity properties of the cathode. In Chen et al.[86,87] study the plasma treatment did not change the crystal structure, but improved the crystallinity of the films (Figure 7a). It also made clear particles on the surface of the films agglomerate into smoother undistinguishable grains (Figure 7b). After the plasma treatment the films exhibit less capacity fading than in the untreated films (Figure 7c).

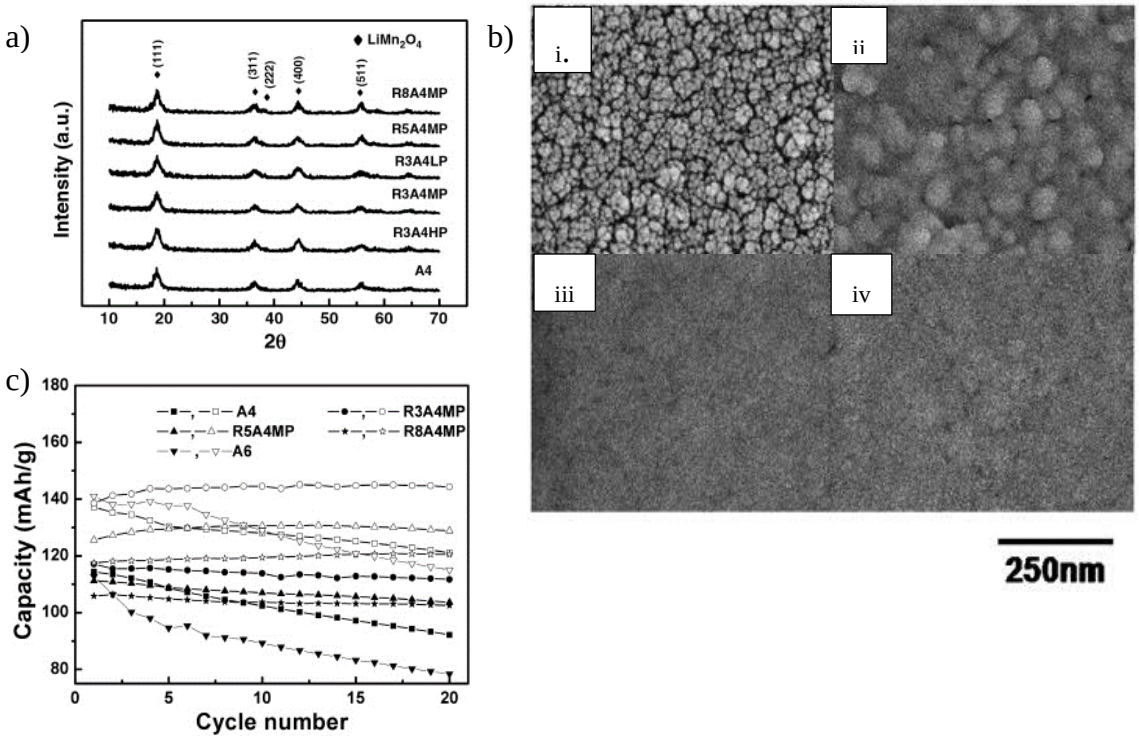

Figure 7. The effect of oxygen plasma treatment to a) crystallinity b) morphology (i. A4, ii. R3A4LP, iii. R5A4MP and iv. R8A4MP) and c) discharge capacity at voltage range 4.5 V – 3.0 V (filled marks) and 4.5 V – 2.0 V (open marks). A4 is a sample annealed in 400 °C, R3A4HP, R3A4MP, R3A4LP are A4 samples treated with rf power of 30 W under 1 x 10^{-1} Torr, 1 x 10^{-2} Torr and 1 x 10^{-3} Torr pressure respectively, R5A4MP and R8A4MP are A4 samples under 1 x 10^{-2} Torr treated with rf power of 50 W and 80 W respectively. Reprinted from Thin Solid Films, Vol. 517, 14, Chen et al, Modification of low temperature deposited $LiMn_2O_4$ cathodes by oxygen plasma irradiation, pages No. 4192-4195, Copyright 2009 with permission from Elsevier.

4.2.2.2 Pulsed Laser Deposition

In pulsed laser deposition (PLD) thin films are deposited utilizing laser ablation technique. A high-power pulsed laser beam is focused to a target and the target material evaporates and a laser plume is ejected from the target surface. The plume expands from the target in perpendicular direction and the species condense on the substrate forming a thin film.

Spinel $LiMn_2O_4$ films have been deposited by PLD on Si[ref. 93-96], Pt[ref. 97-99], Au[ref. 97-99], Pt/Ti/SiO_2/Si(100)[ref. 100], stainless steel[ref. 93,94,101,102] and $SrTiO_3$ (100)[ref. 102] substrates using Li-Mn-O pellets[96-99] or stoichiometric $LiMn_2O_4$[ref. 93,95,98,100-103] as target materials. The deposition temperatures were in between 300 and 627 °C for most of the studies[93,97-99,101], but depositions at lower temperatures (100 – 300 °C) has been done as well.[96] The

oxygen pressure was at around 10 – 33 Pa[97-99]. The laser power was 1.0 J cm^{-2} (ref. 97-99) or 160 mJ[93,94,100,101] with 10 Hz frequency in every deposition.

Different temperature - oxygen pressure combinations were tested by Tang et al[94] (Figure 8). The film deposited at 623 °C and 200 mTorr of oxygen had a mixture of $LiMn_2O_4$ and Mn_3O_4 phases, the film deposited under same temperature but with 100 mTorr oxygen pressure was phase pure spinel $LiMn_2O_4$. The film deposited at 400 °C and 200 mTorr pressure also had the spinel phase, but the peaks in diffractogram were broad compared to the samples deposited at higher temperature. When the deposition temperature was only 200 °C, the film was amorphous.[104]

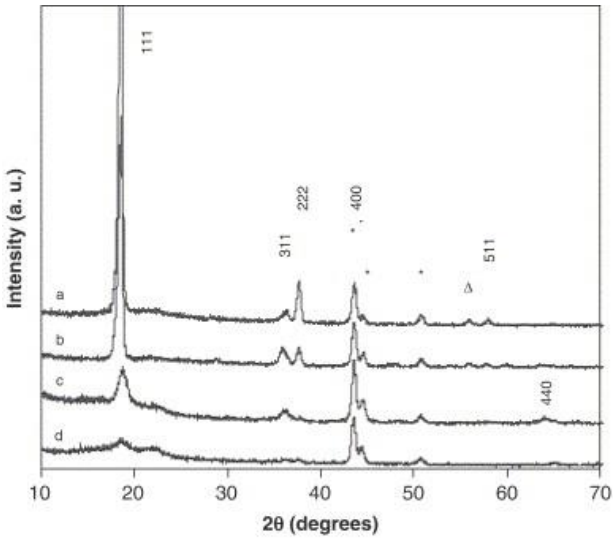

Figure 8. XRD diffractograms of $LiMn_2O_4$ thin films deposited with PLD at a) 623 °C and 200 mTorr, b) 623 °C and 100 mTorr, c) 400 °C and 200 mTorr and d) 200 °C and 200 mTorr. Reprinted from Journal of Solid State Chemistry, Vol. 179, 12, Tang et al, Comparative study of $LiMn_2O_4$ thin film cathode grown at high, medium and low temperatures by pulsed laser deposition, pages No. 3831-3838, Copyright 2006 with permission from Elsevier.

$LiMn_2O_4$ has been deposited with PLD also by using certain multilayer technique.[105] In this study $LiMn_2O_4$ and Li_2O targets were used alternately to produce multilayers to compensate the lithium loss in the films.

4.2.3 Chemical vapor deposition methods

In chemical vapor deposition the precursor gases are led to react in a heated substrate surface to produce a desired thin film. The reaction can occur also already on the gas phase. The possible by-products are removed from the reaction chamber with a gas flow.

$LiMn_2O_4$ has been prepared by CVD onto aluminum foil, nickel-rich steel foil and silica slide substrates. The precursors were $(MeCp)Mn(CO)_3$ (MeCp = methylcyclopentadienyl) and Li(thd) (thd = 2,2,6,6-tetramethyl-3,5-heptanedionato). The deposition temperature needed to be above 650 °C to achieve single phase $LiMn_2O_4$, at lower temperatures the deposited film was a mixture of Li_2MnO_3, MnO and $LiMn_2O_4$ phases.[106]

Spinel $LiMn_2O_4$ has been prepared also with a "mist CVD" technique. The aqueous precursor solutions are ultrasonically atomized and the aerosol particles are then led to react on silica glass substrate to produce a $LiMn_2O_4$ thin film. The precursors were 0.033 M lithium acetate and 0.06 M manganese acetate. The deposition was done at 200 °C. The films were sintered at 600 – 800 °C for 1 h after deposition.[107] The as-deposited films were phase pure spinel $LiMn_2O_4$ and the crystallization of the films increased when the films were annealed (Figure 9a). As shown in field emission scanning electron microscopy (FE-SEM) images (Figure 9b), the as-deposited films were dense and smooth with about 200-300 nm grain size. The films got thinner from about 1 μm to 750 nm when they were sintered at 700 °C. [107]

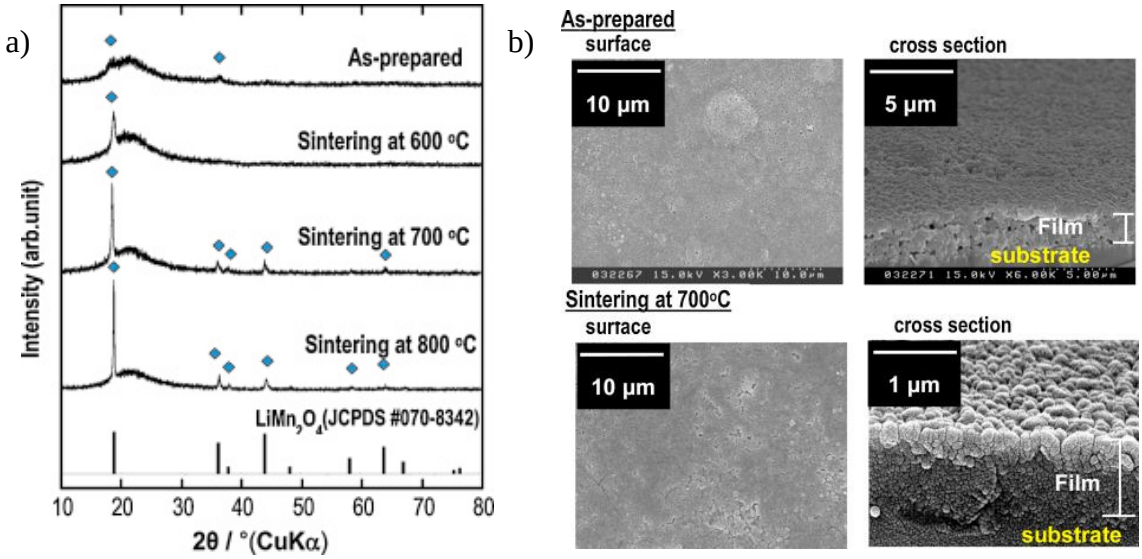

Figure 9. a) X-ray diffractogram of chemical vapor deposited $LiMn_2O_4$ and after sintering at 600, 700 and 800 °C. b) FE-SEM images of as-deposited $LiMn_2O_4$ and at 700 °C sintered $LiMn_2O_4$. Reprinted from Materials Research Bulletin, Vol. 53, Tadanaga et al, Preparation of $LiMn_2O_4$ thin films for thin film lithium secondary batteries by a mist CVD process, pages no. 196-198, Copyright 2014, with permission from Elsevier.

4.2.3.1 Atomic Layer Deposition

In the ALD growth process a gas precursor is pulsed to react with the surface. When suitable reaction time has passed, the reaction chamber is purged with an inert gas. The purge removes all unreacted precursor and the side products from the surface reaction. Then a second gas precursor is pulsed to react with the monolayer generated by the first precursor. Finally, the residue of the second precursor is purged away together with possible side products from the reaction. After the second purge the surface is similar as in the beginning, only one atomic or molecular layer thicker. The four-step reaction cycle is ready to start again, and it is repeated until the film has a desired thickness. The surface reaction can be activated in a conventional way by heating, with plasma or with ultraviolet radiation or visible light. These techniques are called thermal ALD, plasma-enhanced ALD (PE-ALD) and photo-assisted ALD (PA-ALD), respectively.

$LiMn_2O_4$ thin films can be deposited with ALD by separate insertion of lithium into a manganese oxide film. Lithium can be inserted by ALD[108] or with electrochemical methods[109]. MnO_2 is reported to be the most stable oxide phase in thin films deposited by ALD, but other manganese oxides have been deposited successfully as well.[110]

The β-MnO_2 have been deposited with traditional thermal ALD and with PE-ALD. In thermal ALD the most common precursors used are $Mn(thd)_3$ and O_3. [110-112] The depositions have been done with these precursors at temperatures between 150 – 250 °C. PE-ALD depositions have been done using $Mn(thd)_3$ and NH_3, H_2, O_2 and H_2O plasma gases as precursors.[112] The depositions were done at temperatures between 150 – 250 °C.

MnO_2 films have been deposited on a variety of substrates, since the substrate has an effect on the crystallization of MnO_2. Thermal atomic layer depositions have been done on amorphous substrates: soda-lime glass, Si(100) with native oxide, Kapton™ foil, as well as to single-crystal substrates: α-SiO_2(001), α-Al_2O_3(012), α-Al_2O_3(001), muscovite(001), MgO(100), NaCl(100), KCl(100), KI(100), KBr(100).[113,114] Depending on the substrate the phases of α-MnO_2 (NaCl(100), KCl(100) and KBr(100) substrates)[114], β-MnO_2 (α-Al_2O_3(012), muscovite(001)[114], MgO(100) and α-SiO_2(001) substrates) and ε-MnO_2 (α-Al_2O_3(001) substrate)[113,114] were obtained. In addition a possibly new β'-MnO_2 phase was identified.[114]

Mn_3O_4 and α-Mn_2O_3 have been deposited using $Mn_2(CO)_{10}$ and O_3.[115] The depositions were done at low temperatures: 60 – 100 °C and 120 – 160 °C, respectively. MnO has been deposited from $Mn(CpEt)_2$ (CpEt = ethylcyclopentadienyl) and H_2O.[108,116] The deposition was done at temperatures of 100 – 300 °C. When the MnO films were exposed to O_3, 22 Å of the surface of the film oxidized to MnO_2.[117] An assumption is that the slow bulk diffusion of Mn and O limits the depth of conversion from MnO to MnO_2. If the O_3 post-treatment was done with $Mn(CpEt)_2$ pulses, a self-limiting multilayer of crystalline Mn_5O_8 was produced. Mn_5O_8 has an intermediate composition of MnO and MnO_2.

Lithium insertion has been done with ALD into MnO and MnO_2 films, which were deposited as described earlier.[110,116] The lithium insertion into MnO was done by pulsing LiO^tBu (lithium tert-butoxide) and H_2O or $LiN(SiMe_3)_2$ and H_2O as subcycles in between the MnO deposition cycles.[108] The deposition temperature was 250 °C for the LiO^tBu process and 200 °C for the $LiN(SiMe_3)_2$ process. The MnO films deposited with LiO^tBu or $LiN(SiMe_3)_2$ were non-uniform, amorphous and showed hardly any lithium content.

When combining MnO_2 deposition process with Li(thd) and O_3 subcycles at 225 °C, highly uniform $Li_xMn_yO_z$ films were produced. The stoichiometric $LiMn_2O_4$ phase was achieved already with 1.0 % Li(thd)-O_3 subcycles (Figure 10).[108] The films were phase pure spinel $LiMn_2O_4$ according to the XRD results.

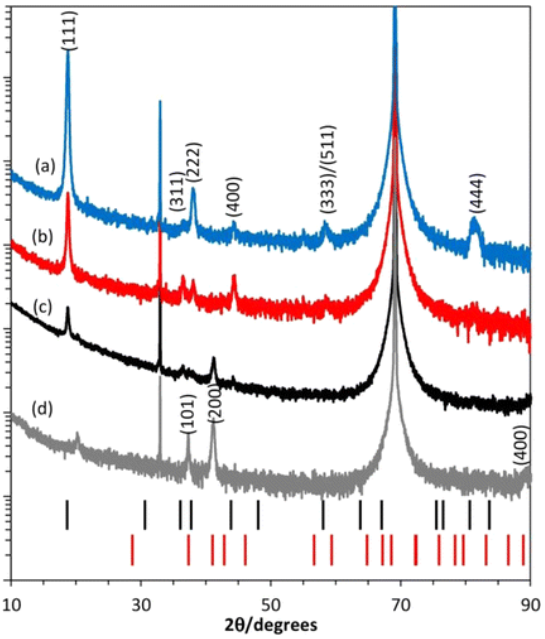

Figure 10. XRD of $Li_xMn_2O_4$ thin films with a) 5.0 % b) 1,7 % and c) 1 % LI(thd)-O_3 subcycles and d) β-MnO_2. Reprinted with permission from The Journal of Physical Chemistry, C, Vol 118, Miikkulainen et al, Atomic layer deposition of spinel manganese oxide by film-body-controlled lithium incorporation for thin-film lithium ion batteries, pages 1258-1268, 2014. Copyright 2014 American Chemical Society.

Lithium insertion into MnO_2 was tested also after the MnO_2 deposition.[108] Li(thd) and O_3 or LiO^tBu and H_2O were pulsed after the MnO_2 deposition at 225 °C. The post-deposition treatment also converted the whole MnO_2 film into $LiMn_2O_4$.

Atomic layer deposited MnO thin films have been converted to $LiMn_2O_4$ with electrochemical conversion.[109] A 0.10 M Li_2SO_4 aqueous electrolyte was used. The pH of the electrolyte was varied and the effect of the pH to the conversion depth was studied. In a mildly acidic solution (pH ≈ 6) the conversion depth from MnO to $LiMn_2O_4$ was ≤ 20 nm, whereas at pH ≈10 the conversion depth was as high as 200 nm.

4.3 $LiMn_2O_4$ Nanorods

The cubic spinel $LiMn_2O_4$ has gained great interest as a 3D battery material, because the structure enables lithium intercalation from every direction. The 3D intercalation pathways are more versatile and appealing than for example layered structure. The $LiMn_2O_4$ has been synthesized not only as thin films but also as nanorods.

$LiMn_2O_4$ 1D nanorods have been done by first synthesizing MnO_2[ref. 118,119], MnOOH[ref. 120-122] or Mn_2O_3[ref. 123] nanorods and then converting them to $LiMn_2O_4$. $MnSO_4$ was dissolved and mixed with ammonium persulfate[118] or $NaClO_3$[ref. 119] and hydrothermally reacted in stainless steel autoclave.[118,119] The MnO_2 product was filtered, washed and dried. For MnOOH, $MnCl_2$[ref. 121] and NaF[ref. 121], ethanol[120] or PEG 400[122] were mixed with $KMnO_4$ in water and reacted at 120 – 160 °C.[120-122]

The nanorods were converted to $LiMn_2O_4$ by dissolving LiOH in ethanol[118-120] or acetone[121,122] and reacting that with MnO_2 or MnOOH. The reaction was carried out in a furnace at elevated temperature[121,122] or by stir-drying at room temperature[118-120]. If the reaction was done at room temperature, the product was annealed to receive the $LiMn_2O_4$ nanostructures. The Mn_2O_3 nanorods were porous and they were converted to $LiMn_2O_4$ by adding LiOH to nanopores. After solid state reaction single-crystalline $LiMn_2O_4$ nanorods were formed (Figure 11a-b). [123] Nanorods formed with Li:Mn molar ratio of 1.2:1 at 750 °C showed excellent electrochemical performance as a cathode and the rod-like morphology preserved even after 1000 electrochemical cycles (Figure 11c).

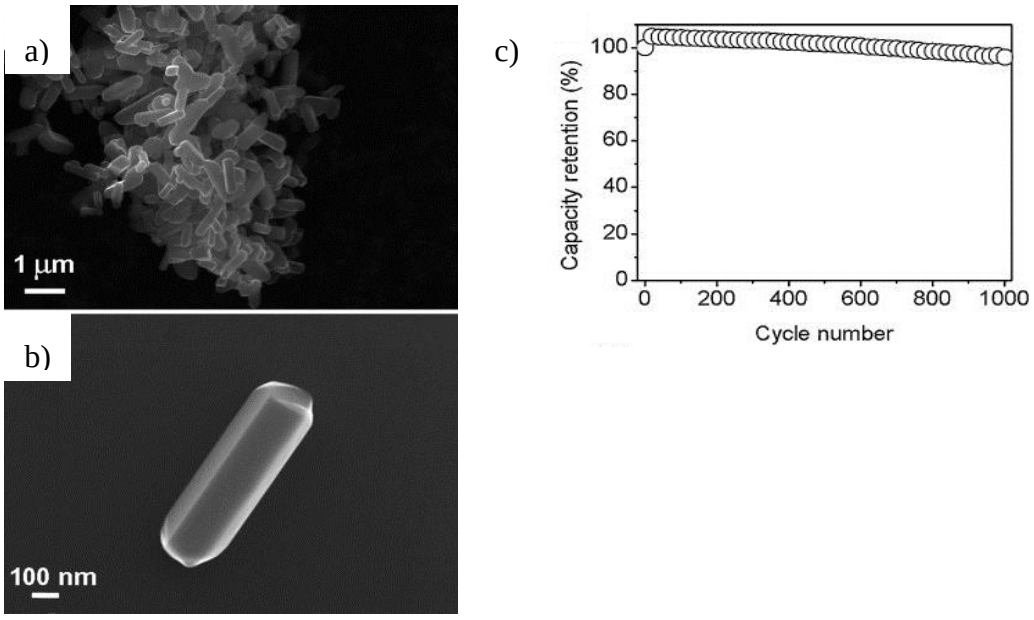

Figure 11. FE-SEM image of $LiMn_2O_4$ nanorods a) medium-magnification b) high-magnification. c) Cycling performance of $LiMn_2O_4$ nanorods. Reprinted with permission from Chemistry – A European Journal, Vol 20, 51, Xiuqiang et al, Synthesis of single-crystalline spinel $LiMn_2O_4$ nanorods for lithium-ion batteries with high rate capability and long cycle life, pages no. 17125 – 17131, Copyright 2014, John Wiley and Sons.

5 X-ray absorption spectroscopy

5.1 Synchrotron light source

A synchrotron light source is a combination of a particle accelerator, which contains a linear particle accelerator and a circular booster, a storage ring and the experiment stations which are called beamlines (schematic illustration in Figure 12). Electrons are accelerated to relativistic speeds on the linear particle accelerator and the booster and are then moved to the storage ring to travel a circular path with constant energy. The path of the traveling electrons is guided by magnetic fields. The magnets can either bend the electron beam (bending magnet) or force it to an oscillating path (wiggler and undulator). The traveling electrons are producing electromagnetic waves i.e. light, which point to the tangential directions of the circular path. The light is directed to a beamline and on to the sample.[124]

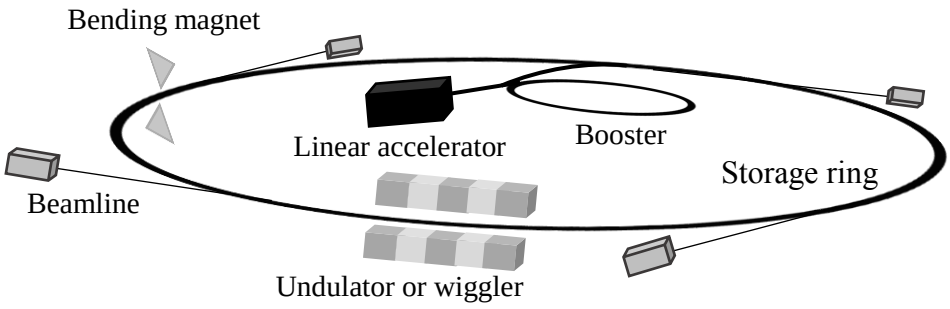

Figure 12. A schematic presentation of a synchrotron light source.

Synchrotron radiation has superb properties when compared to other x-ray sources. The radiation has high brilliance, high level of polarization, small angular divergence and its energy is widely tunable for different purposes. That makes synchrotron radiation an excellent tool for example for x-ray absorption spectroscopy (XAS).[124]

5.2 X-ray absorption

When x-rays come to contact with the sample, an x-ray photon may be absorbed to an atom and excite one of its electrons to a continuum leaving an electron hole to the initial core shell (Figure 13a). The process is called photoelectric absorption. The core shell hole may be filled with an electron from the outer shells of the atom. When an electron fills the core hole, it can emit either a fluorescence photon or another electron, Auger electron, from the other core shells at the same time (Figure 13b and c). These processes are called fluorescence emission and Auger emission, respectively.

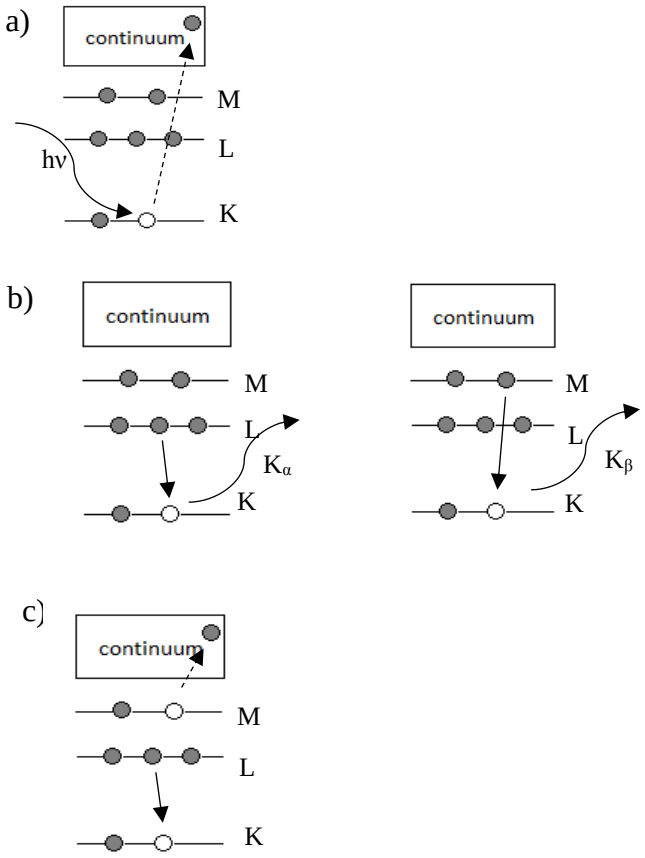

Figure 13. a) A schematic presentation of photoelectric absorption, b) a fluorescent x-ray emission from either L or M shell and c) Auger electron emission.

5.3 X-ray absorption spectrum

A measured x-ray absorption spectrum can be divided to three regions (Figure 14). The first part is a pre-edge region, which is the part before the energy threshold for the absorption. This part of the spectrum is usually flat and shows only background. In some cases it may have peaks which come as a result of excitation to the atom's first unoccupied energy state. The second part of the spectrum is called x-ray absorption near edge structure (XANES) or near edge x-ray absorption fine structure (NEXAFS). The third part of the spectrum is the oscillating curve after the absorption edge and is called extended x-ray absorption fine structure (EXAFS).

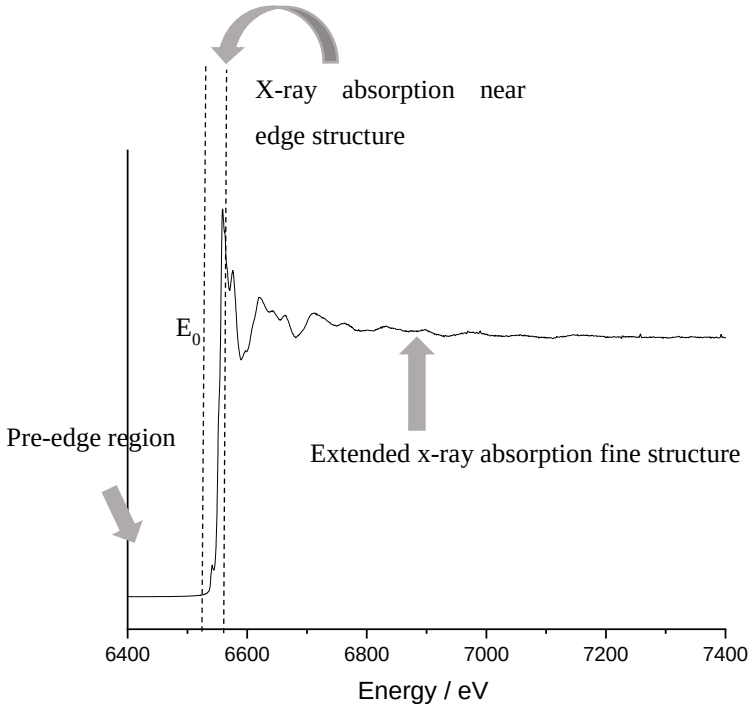

Figure 14. An x-ray absorption spectroscopy curve marked with the pre-edge, XANES and EXAFS regions.

5.3.1 X-ray absorption near edge structure (XANES)

The x-ray absorption near edge structure is the absorption edge of the material. In the XANES energy range, electrons are excited to unfilled or partially filled energy states and hence the technique probes the density of states (DOS) of the unfilled energy states.[125] The energy of the absorption edge, E_0 in Figure 14, varies depending on the element as well as

on the environment of the absorbing atom. Hence the energy of the adsorption edge is element specific and even oxidation state specific.

5.3.2 Extended x-ray absorption fine structure (EXAFS)

The extended x-ray absorption fine structure is the oscillating part of the XAS spectrum above the absorption edge. In this part, the liberated photoelectron propagates away from the primary atom as a spherical wave. The photoelectron is backscattered by the neighboring atoms which creates interference between the out-going and backscattering waves producing the oscillation pattern. The mechanism is illustrated in Figure 15.

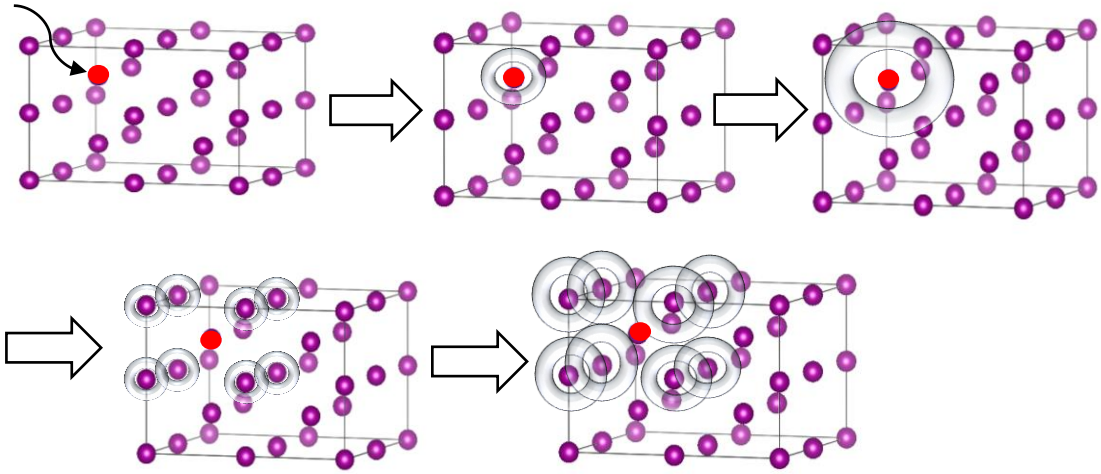

Figure 15. Schematic presentation of the EXAFS process. The excited electron of the first atom has high enough energy to escape from the atom's sphere and propagate until it meets the neighboring atoms. The photoelectron is then scattered from the neighboring atoms. The backscattered wavefunctions interfere with the out-going waves and produce oscillating EXAFS spectrum.

Since EXAFS is produced by the whole crystal structure of the material, the measurement gives information about the bond lengths and coordination of the atoms.[124,126] It is found that the measurements are not accurate if the sample is amorphous or highly disordered since the intensity of the peaks is lowered because of the disorder. With the help of XANES it is possible however to determine the structure of even a disordered sample.[127-130]

Some major advantages arise when using synchrotron light for the x-ray absorption measurements. The synchrotron light facilities provide tunable high energy incident beams,

so even electrons with the highest binding energies i.e. electrons closest to the nucleus can be excited and studied. The absorption edge energy is mostly influenced by the nucleus that the electron is orbiting, so the XANES spectrum gives valuable information about the nucleus and the atom itself together with the local environment.

5.4 Measurement principle of X-ray absorption spectroscopy

X-ray absorption spectrum is a measure of the absorption of the material as a function of energy. The absorption spectrum can be measured in a transmittance geometry, by measuring the fluorescent radiation (total fluorescence yield, TFY), or by a total-electron-yield (TEY).

The atoms of the material have certain absorption coefficient μ. The coefficient can be obtained from the transmission measurement as a function of photon energy ε (Equation 1). I_t is the intensity of x-ray photons transmitted through the sample with thickness d. I_0 is the intensity of the incident beam and μ(ε) is a material specific absorption coefficient.

$$I_t = I_0 e^{-d\mu(\varepsilon)} \tag{1}$$

The absorption coefficient is different for free atoms $\mu_0(\varepsilon)$ and for atoms in a crystal lattice $\mu_\chi(\varepsilon)$. In XAS analysis it is useful to introduce a dimensionless quantity χ(q) which is dependent on the absorption coefficients as defined in Equation 2. The photoelectron wavenumber q is used when defining the quantity χ(q). The photoelectron wavenumber is related to the photon energy as shown in Equation 3. ħ is the Planck's constant, m_e is the mass of the electron and ω_κ is the angular frequency of the photon beam.

$$\chi(q) = \frac{\mu_x(\varepsilon) - \mu_0(\varepsilon)}{\mu_0(\varepsilon)} \tag{2}$$

$$\frac{\hbar^2 q^2}{2m_e} = \varepsilon - \hbar\omega_K \tag{3}$$

When the absorption measurement is done in a transmission geometry, the absorption coefficient is obtained from Equation 4. The coefficient is a sum of atoms of interest $\mu_\chi(\varepsilon)$ and all the other atoms in the sample $\mu_A(\varepsilon)$.

$$\mu(\varepsilon) = \mu_A(\varepsilon) + \mu_\chi(\varepsilon) = \mu_A(\varepsilon) + \mu_0(\varepsilon)[1 + \chi(q)] \qquad (4)$$

$\chi(q)$ can be subtracted from the data by theoretical knowledge and numerical methods. This becomes easier if reference samples are measured simultaneously under the same conditions.

Another option for determining $\chi(q)$ is to measure the fluorescent radiation. The intensity of the incident beam has been attenuated by a factor of $e^{-\mu x}$. If the fluorescent radiation is created from the depth dx with a probability $\mu_\chi(\varepsilon)dx$, the fluorescence is proportional to

$$\int_0^\infty \mu_\chi(\varepsilon) e^{-\mu(\varepsilon)x} e^{-\mu(\varepsilon_f)x} \mathrm{dx} = \frac{\mu_\chi(\varepsilon)}{\mu(\varepsilon) + \mu(\varepsilon_f)} \qquad (5).$$

The unwanted contribution from scattering processes is diminished by placing the detector to 90° angle from the incident beam. The detector is then measuring radiation from a solid angle $\Delta\Omega$. The $\mu(\varepsilon_f)$ is the inverse absorption length at the fluorescent x-ray energy ε_f. The fluorescent intensity is shown below in Equation 6. The Auger electron process relative to fluorescent radiation is ϵ.

$$I_t = I_0 \epsilon \left(\frac{\Delta\Omega}{4\pi}\right) \frac{\mu_\chi(\varepsilon)}{\mu(\varepsilon) + \mu(\varepsilon_f)} [1 - e^{-(\mu(\varepsilon) + \mu(\varepsilon_f))d}] \qquad (6)$$

The total-electron-yield measurements are direct measurements of the specimen current that yields to accurate $\chi(q)$ functions. The TEY method probes only tens to hundreds of atoms from the surface, so it is a surface sensitive method. The sampling depth is determined by the penetration range of the Auger electrons that are emitted by the absorbing atom.[131]

5.5 X-ray absorption spectroscopy in studying $LiMn_2O_4$

$LiMn_2O_4$ has been studied widely with x-ray methods. As a transition metal oxide, many of the studies have been done on the manganese K- and L-edges as well as on oxygen K-edge.

Figure 16a shows the simplified molecular orbital diagram of the octahedral [MnO_6]. Figure 16b is a molecular orbital diagram of the Mn^{3+} 3d orbital splitting. The first split occurs due to the octahedral coordination in [MnO_6]. The further splitting occurs because of the Jahn-Teller distortion.

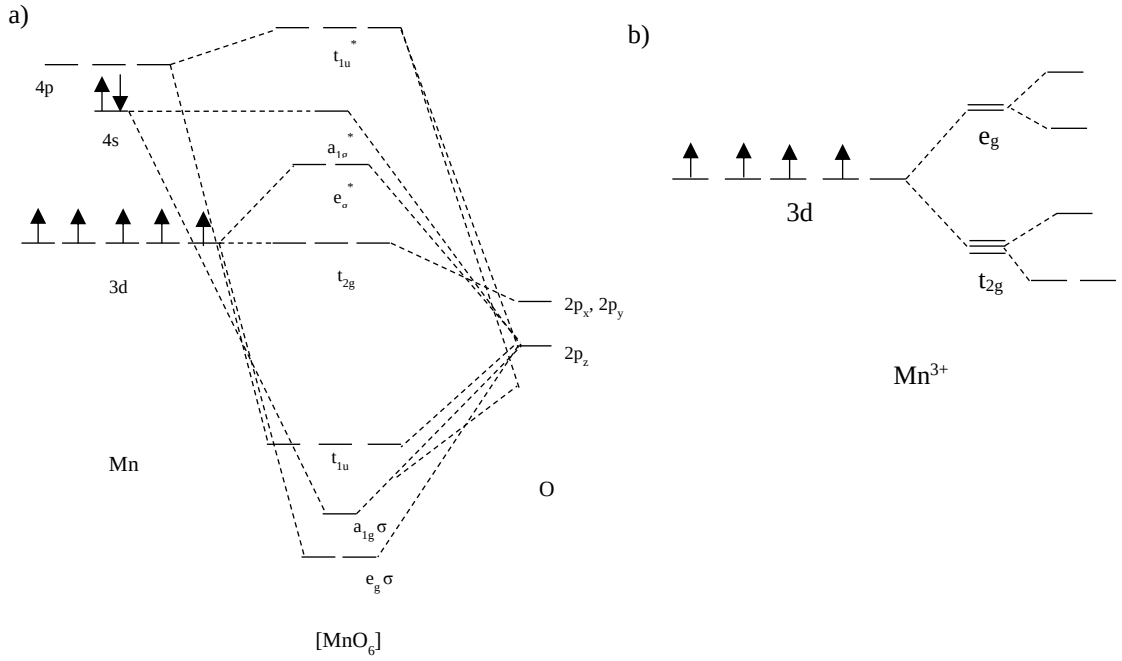

Figure 16. a) Simplified orbital diagram of [MnO_6]. b) Diagram of Mn 3d –orbitals. First 3d split occurs due to the octahedral coordination, the second one because of the Jahn-Teller distortion.

5.5.1 Oxygen K-edge

The K-edge excitation of oxygen means excitation of an electron from the 1s orbital to the 2p orbital. Transition metal oxides can have four types of unoccupied or partially occupied molecular orbitals. As can be seen in Figure 16, the partially filled orbitals have certain order in energy: $t_{2g} < e_g^* < a_{1u}^* < t_{1u}^*$. The t_{2g} and e_g^* orbitals are attributed to the metal 3d-band, whereas the a_{1u}^* and t_{1u}^* orbitals are attributed to the oxygen p-orbital which is hybridized with the metal 4s- and 4p-orbitals.

The unfilled orbitals form two regions with peaks A and B, and C and D in the oxygen K-edge spectra (Figure 17). In transition metal oxides the two regions in the XAS spectrum are around 15 eV apart from each other. The first region of the spectra has two peaks A and B, because of the ligand field splitting. For the octahedral structure, the A peak at lower energy

attributes to the t_{2g} orbital and the peak B attributes to the e_g orbital. The peaks are not symmetric in intensity due to exchange splitting of the t_{2g} and e_g bands. The exchange splitting means that the two bands of for example t_{2g} split further to high spin and low spin bands. In MnO_2 the exchange splitting results in the e_g spin-up and t_{2g} spin-down levels to almost coincide and thereby increase the intensity of the peak A in the XAS spectrum.[132]

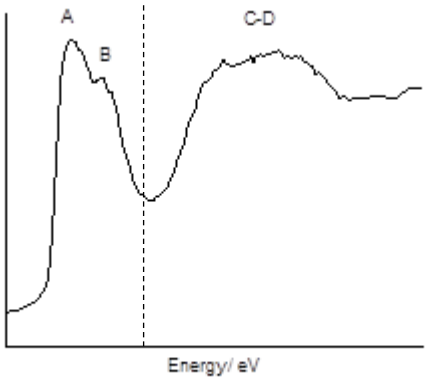

Figure 17. A schematic curve shape of oxygen K-edge XAS in transition metal oxides.

The number of valence electrons i.e. the electron configuration of the metal has an effect on the occupation of the orbitals so it affects the intensities of the peaks in the O K-edge XAS spectrum. The curve is also affected by the crystal structure of the material since the coordination of the oxygen atoms depends on which orbitals are free on the metal.[125] In $LiMn_2O_4$ most changes in the O K-edge XAS occur due to the Mn^{3+}/Mn^{4+} oxidation/reduction or the phase change of the crystal structure.

5.5.2 Manganese K-edge and L-edge

The manganese K-edge absorption means excitation from the 1s orbital. The first peak in the K-edge spectra (Figure 18a) usually appears before the absorption threshold and is the transition of 1s → unoccupied 3d orbitals and/or to hybridized 3d/4p orbitals. The transition from 1s to 3d is dipole-forbidden for octahedral compounds. However weak pre-edge features are commonly observed, because the transition 1s to 3d is quadrupole allowed by selection rules. Some intensity can gain also from the 3d and 4p orbital mixing, since it enables dipole-allowed character.[133,134]

In $LiMn_2O_4$ the manganese ions are a mixture of Mn^{3+} and Mn^{4+}. Their 1s → 3d transition energies mix leading to a broad pre-edge region (A).[135] The main peak, i.e. the absorption threshold corresponds to the excitation from the 1s to the 4p t_{1u} orbital. Usually the absorption threshold itself contains two shoulders (B_1 and B_2) as a result of the two different Mn sites in the spinel $LiMn_2O_4$. Two sharp peaks (C and D) just above the threshold come as a result of excitation to the continuum. The D peak (or sometimes two peaks D_1 and D_2) result from multiple scattering from the neighboring atoms similar to the EXAFS spectrum.

The L-edge means excitation from 2p → 4s and 3d regions. The L-edge of a transition metal has usually two sets of two peaks which come as a result of spin-orbit coupling and the octahedral field splitting of the transition $2p^63d^0$ → $2p^53d^1$ (Figure 18b). The 2p spin-orbit coupling splits the initial state to $2p_{3/2}$, which is called L_{III}, and $2p_{1/2}$, which is L_{II}. The octahedral field splitting causes even further splitting and the L_{III} and L_{II} peaks adopt a doublet shape. The resonances are then called L_{III}-t_{2g} (A), L_{III}-e_g (B) and L_{II}-t_{2g}, L_{II}-e_g (C-D).[125,136-138]

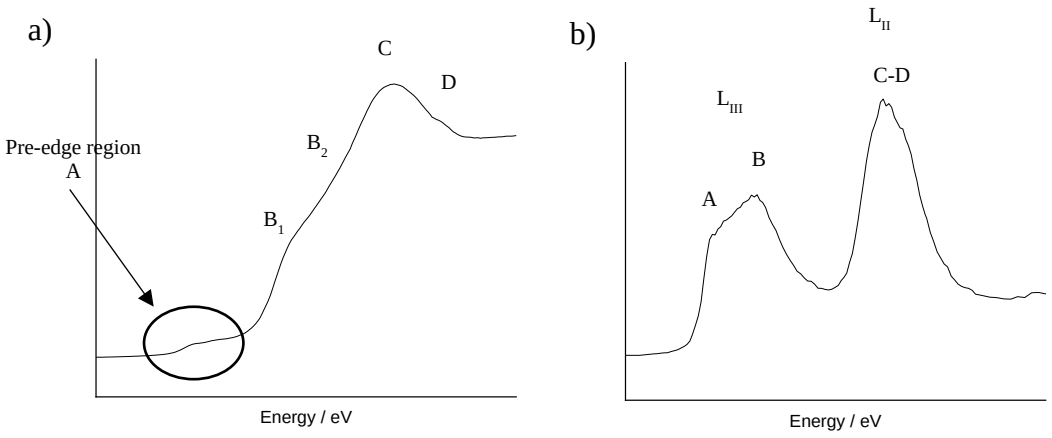

Figure 18. Schematics of a) Mn K-edge and b) L-edge.

The peaks shift to higher energies when the number of valence electrons of metals decreases i.e. when the oxidation state increases. The intensity ratio L_{III}/L_{II} reaches a maximum at d^5 electron configuration and from there it diminishes when moving towards d^0 and d^{10}. The overall intensity decreases when the number of d electrons increases, because when the number of unoccupied d-orbitals decreases, there are less places for the 2p electrons to excite

to. Some electronic factors, like multiplet effects, spin and orbital polarization and spin-orbit coupling, complicate the L-edge curve shape.[125]

6 Lithium insertion/extraction to manganese oxide

Many studies have been done to investigate lithium intercalation into manganese oxide structures. This part of the thesis will describe the lithium insertion and x-ray absorption studies on that. The intercalation mechanism has been studied especially with powder samples. Three separate intercalation steps have been noted for compounds with stoichiometry $Li_xMn_2O_4$, $x < 1$, $LiMn_2O_4$ and $Li_xMn_2O_4$, $1 < x$.

X-ray absorption studies have been done both *in-situ* while the lithium-ion battery is working, as well as the more traditional way in between battery cycles or in the middle of one cycle. Measurements have been done mostly on $LiMn_2O_4$ powder, but also on some thin film materials. XAS spectra of powders should go at least somehow hand in hand with the $LiMn_2O_4$ thin films, because bonding and short range order of the atoms do not differ in thin films compared to crystalline powders. Several XAS studies have been done also on doped lithium manganese oxides.[139-145] The doping element is said to improve the cyclability of the cathode.

6.1 Stoichiometric $LiMn_2O_4$

As stated earlier, lithium ions fill the tetrahedral 8a sites of the manganese oxide spinel network.[12] The placement of lithium in the stoichiometric structure has been approved experimentally[146,147] as well as with computational modeling[148]. Theoretically the stoichiometric $LiMn_2O_4$ has 1:1 relation for Mn^{3+}/Mn^{4+} i.e. the structure is $LiMn^{3+}Mn^{4+}O_4$.[149] The stoichiometric $LiMn_2O_4$ has thus two separate octahedral structures $[Mn^{3+}O_6]$ and $[Mn^{4+}O_6]$ with different Mn – O bond distances.[150]

In Liu et al.[151] study Mn L-edge in $LiMn_2O_4$ indicate that the main peak in Mn L_{III}-edge is close to L_{III}-edge of MnO_2 implying the oxidation state of +4. An explanation for that may be that the Li^+ is substituting Mn atoms in the structure rather than intercalating to the interstitial sites. If the explanation is correct, the structure is not stoichiometric $LiMn_2O_4$ but manganese deficient $LiMn_{2-x}O_4$.

The phase change from the cubic to the tetragonal/orthorhombic structure takes place around room temperature as was discussed earlier. The phase change has been studied and noted in XAS as well. Yamaguchi et al.[149] studied Mn K-edge EXAFS at 200 and 300 K. The local JT distortion (ratio between longer Mn^{3+} – O distance and shorter Mn^{4+} – O distance) decreased from 1.19 at 200 K to 1.17 at 300 K. Above the phase change temperature the $[Mn^{3+}O_6]$ structure has local JT distortion which is relatively large, comparable even to tetragonal structures. Below the phase change temperature, the JT distortion is macroscopic and relatively low.[149]

The change of Mn – Mn bond length during the discharge was larger for the high temperature $LiMn_2O_4$ than for the low temperature phase.[152] Hence the lithium intercalation takes place probably via different pathways in the two phases, which causes the different Mn-Mn bond length changes. Paolone et al.[153] propose that the changes in EXAFS are due to charge ordering rather than JT phenomena.

In a study of Shinshu et al.[152]the Mn K-edge absorption edge was lower in energy for the high temperature $LiMn_2O_4$ compared to the low temperature $LiMn_2O_4$. The absorption edge shifts because the concentration of Mn^{3+} ions is larger in the high temperature phase than in the low temperature phase.

6.2 Insertion/extraction of the first lithium ion, $Li_xMn_2O_4$, x < 1

In order for the lithium batteries to work, the lithium intercalation must be reversible. The Mn – O network allows two lithium ions to intercalate for every MnO_6 octahedron. This chapter will describe the insertion/extraction mechanism for the first Li^+ ion, i.e. when the structure of the compound is $Li_xMn_2O_4$, x < 1.

When lithium is extracted from stoichiometric $Li_xMn_2O_4$, in the composition region $0.5 < x < 1.0$ the phase change is said to be homogeneous, i.e. just a shrinkage of the host matrix.[154] Some studies have been done for the region $x \leq 0.5$ and the phase is said to change to two cubic phases, i.e. an irreversible structural phase change takes place.[154-156] λ-MnO_2 is a cubic phase that describes the original manganese oxide framework after lithium has been extracted.[15] The λ-MnO_2 phase has been reported to have a stoichiometry $Li_xMn_2O_4$ x = 0.13(ref. 154) and x = 0.28(ref. 157,158), so in the range of $x \leq 0.5$. Possibly the irreversible structural phase change takes place after the λ-MnO_2 is formed. Alternately, some structural

changes occur already in the range of x ≈ 0.5. The symmetry of the cubic spinel $Li_xMn_2O_4$ is broken when x = 0.5 which has an effect on the diffusion pathways as will be described later.

The Mn K-edge absorption edge shifted to higher energies when the concentration of Li^+ decreased in unstoichiometric structures $Li_xMn_2O_4$, x < 1.[135,141,152,159-163] Figure 19 is an example of a XANES spectra of Mn K-edge of lithium deficient $Li_{(1-z)}Mn_2O_4$ structures from Okumura et al study.[141] Studies that were done *in situ* while the battery was working also noted the same peak shift in the Mn K-edge.[163] The absorption edge shift indicates that the amount of Mn^{4+} increases as lithium is extracted. When electrons leave the Mn ion, the remaining ones are more tightly bonded and require more energy to be excited which shifts the absorption edge to higher energies.

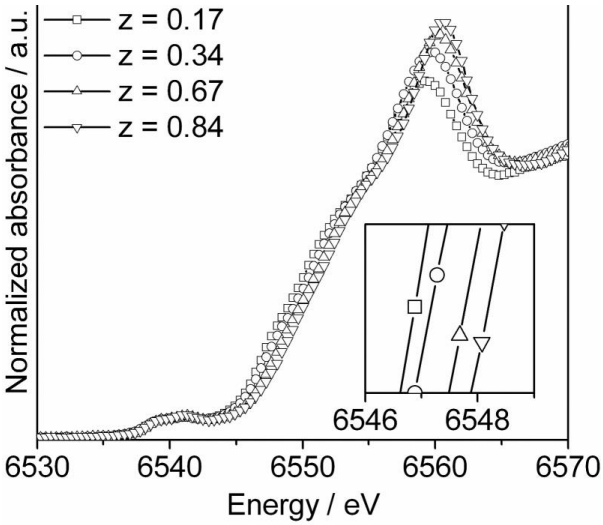

Figure 19. XANES spectra of the Mn K-edge of $Li_{(1-z)}Mn_2O_4$ sample. When Li^+ concentration decreases the abdorption edge shifts to higher energies. Reproduced from Dalton Trans., 2011, 40, 9752 with permission of The Royal Society of Chemistry.

The fine structure of the pre-edge region stayed similar until formation of λ-MnO_2.[135,161] This supports the conclusion that the [MnO_6] framework would not change in the lithium insertion/extraction process. One notable difference in the pre-edge region fine structure is that the peaks are sharper for pure λ-MnO_2 than in the $LiMn_2O_4$.[135] Some studies also noted significant intensity increase in the pre-edge region when lithium was extracted from the material. This is expected, since the features from λ-MnO_2 should increase in intensity when lithium is extracted.[159]

The Mn L-edge XANES absorption edge shifted to higher energy levels when the amount of lithium decreased, which supports the conclusion that the Mn^{3+} ion concentration decreases. [141,164,165] Figure 20a is an example of Mn L-edge XANES spectra of $Li_{(1-z)}Mn_2O_4$ structures. $Li_xMn_2O_4$, x < 1, thin film was reported to have a very similar Mn L-edge XAS as the powder samples.[166]

Changes in the O K-edge XANES have also been noted during lithium extraction. Figure 20b shows O K-edge of $Li_{(1-z)}Mn_2O_4$ structures. The intensity of the first peak A increases with decreasing Li^+ concentration. This means that the electron is released from the hybridized orbital between Mn 3d and O 2p. The shift indicates that the O^{2-} takes part to the charge compensation in the lithium insertion/extraction process.[141,165] Similar behavior has been reported for $Li_xMn_2O_4$, x < 1, thin film as well.[166]

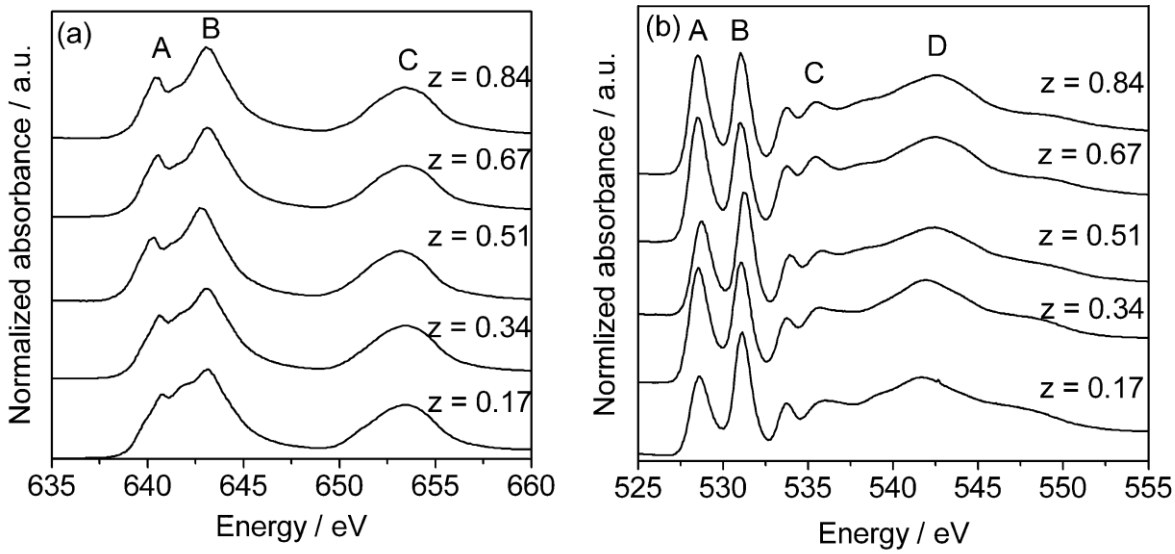

Figure 20. a) Mn L-edge XANES spectra of $Li_{(1-z)}Mn_2O_4$ structures. b) O K-edge XANES spectra of $Li_{(1-z)}Mn_2O_4$ structures. Reproduced from Dalton Trans., 2011, 40, 9752 with permission of The Royal Society of Chemistry.

The peaks corresponding to Mn – O and Mn – Mn distances in the Mn K-edge EXAFS decrease in intensity when lithium concentration increases.[159,160,162,167] This indicates that the Mn – O and Mn – Mn bond distances increase as lithium is inserted to the structure. Figure 21 is an example of EXAFS spectra of $LiMn_2O_4$ in its charged and discharged states. In charged battery most Li^+ ions are on anode and during discharge they transport and intercalate to cathode. Meaning that in charged state the $Li_xMn_2O_4$ cathode has very low Li^+ concentration i.e. $x << 1$ and in discharged state the Li^+ transports to cathode and $x \approx 1$.

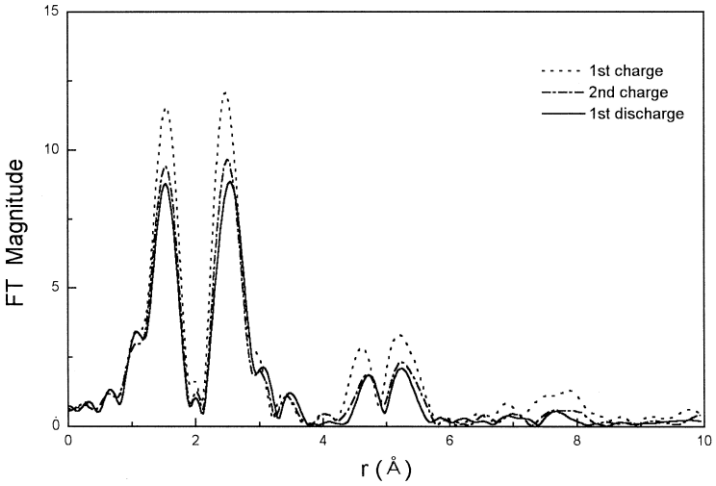

Figure 21. Mn K-edge EXAFS spectra of $Li_xMn_2O_4$ structures. The charged states (dot and dash-dot lines) have the lowest lithium concentration and the discharged state (solid line) has the highest lithium concentration. Reprinted from Journal of Power Sources, Vol. 81-81, Kwon et al, A study on the effect of lithium insertion-extraction on the local structure of lithium manganese oxides using X-ray absorption spectroscopy, pages no. 510-516, Copyright 1999, with permission from Elsevier.

Overall the change from the stoichiometric $LiMn_2O_4$ to λ-MnO_2 occurs without significant phase change. The Mn K-edge shifts to higher values as lithium is extracted and hence when Mn^{3+} is oxidized to Mn^{4+}. The oxygen K-edge XANES showed however that the O^{2-} ions possibly take part to the charge compensation as well. The lithium extraction results in a single phase that consists uniformly of $Mn^{4+}O_6$ octahedrons, which causes shrinkage of the original unit cell. The Mn XANES and EXAFS did not show any remarks of structural phase change of the octahedral Mn ions. However, this does not exclude the possibility that the structure could undergo some irreversible cubic phase changes. Figure 22 is a schematic presentation of the phase change from $LiMn_2O_4$ to λ-MnO_2.

6.2.1 Lithium migration pathway

When lithium is migrating in the λ-MnO_2 structure, the migration is strongly affected by the direction of the Jean-Teller distortion. When lithium is first intercalating to the λ-MnO_2 structure, it fills the 8a interstitial sites. The pathway for lithium to migrate in the structure goes through octahedral 16c sites. The migration activation barrier, in between two 8a sites, is the lowest when the Li-O bond in the migration transition state is parallel with two elongated Mn-O bonds. The energy barrier is the highest when the elongated Mn-O bonds are perpendicular to Li-O bond in the transition state.[168,169]

When the stoichiometry is $Li_{0.5}Mn_2O_4$, the symmetry of the spinel structure is broken. This leads to a higher diffusion energy barrier from one 8a site to the nearest-neighbor 8a site compared to the diffusion inside the symmetrical structure. The broken symmetry is one reason for the $Li_{0.5}Mn_2O_4$ to be less stable than $LiMn_2O_4$.[148]

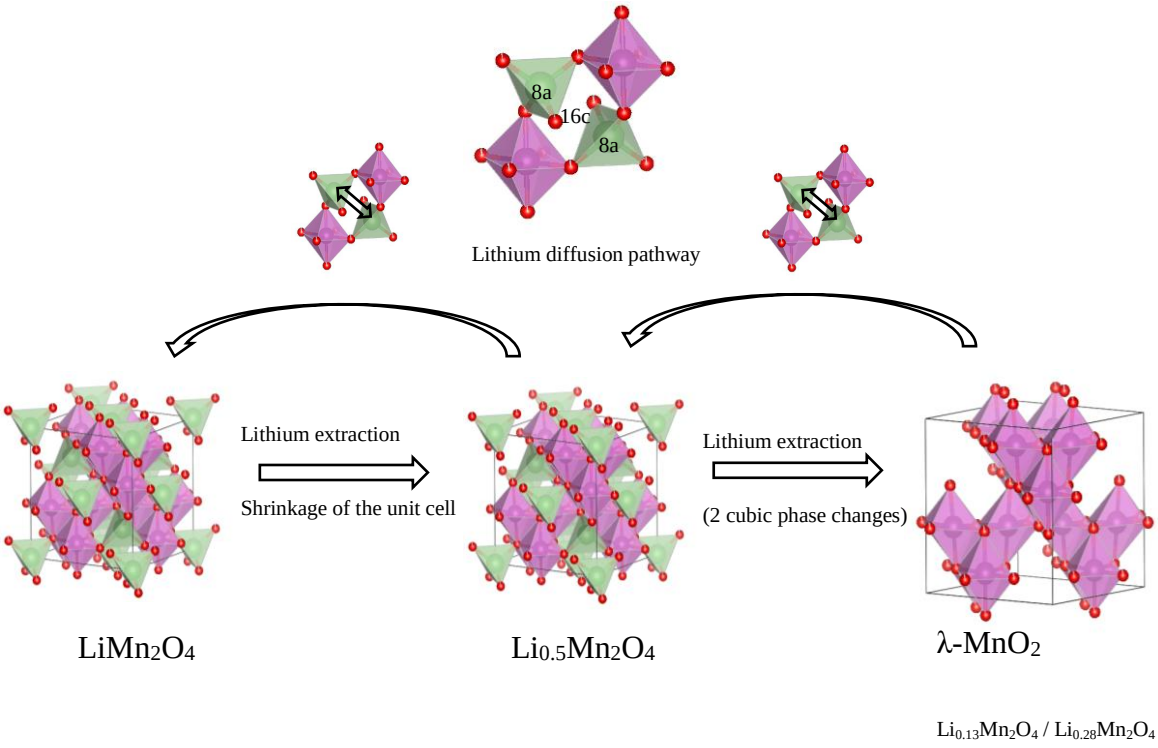

Figure 22. The phase change of the spinel $LiMn_2O_4$ to λ-MnO_2 via lithium insertion/extraction.

6.3 Insertion/extraction of the second lithium ion, $Li_xMn_2O_4$, x > 1

Reports from two phase structures have been made, when the lithium stoichiometry exceeds $LiMn_2O_4$.[147,170] Mn^{4+} reduces to Mn^{3+} when the second lithium is inserted. Experimental[147,170] and computational[171]studies found phases of cubic $Li_{1+x}Mn_2O_4$ when $0 < x \leq 0.1$, and tetragonal $Li_{1+x}Mn_2O_4$ when $0.8 \leq x < 1.25$ in electrochemical lithium extraction. The tetragonal phase is said to still have the spinel framework, but it is distorted from cubic to tetragonal due to the increasing amount of the Jahn-Teller active Mn^{3+} ions.[147,170]

In the Mn K-edge measurements on $Li_xMn_2O_4$, $1 < x$, the absorption edge shifts to lower energies as the amount of lithium increases (Figure 23).[135,172-174] This energy shift goes hand

in hand with the results from the compounds where x < 1. The peak shift to lower energies indicates that lithium is intercalated to the material without replacing Mn atoms. Then the ratio of Mn^{3+} / Mn^{4+} increases and the absorption edge shifts to lower energy.[172] A similar shift would be expected in oxygen non-stoichiometric compounds $Li_{1+x}Mn_{2-x}O_{4-\delta}$. However, this behavior has been said to be untypical for spinel structures.[172]

In addition to the edge shift, the fine structure of the pre-edge region of Mn K-edge XANES changes from cubic to tetragonal as the cubic $LiMn_2O_4$ changes to tetragonal $Li_2Mn_2O_4$ (Figure 23).[135,175] When the structure changed from λ-MnO_2 to cubic $LiMn_2O_4$ the pre-edge region did not have significant changes. This supports the assumption discussed earlier that no significant phase change occurs during the first lithium ion intercalation.

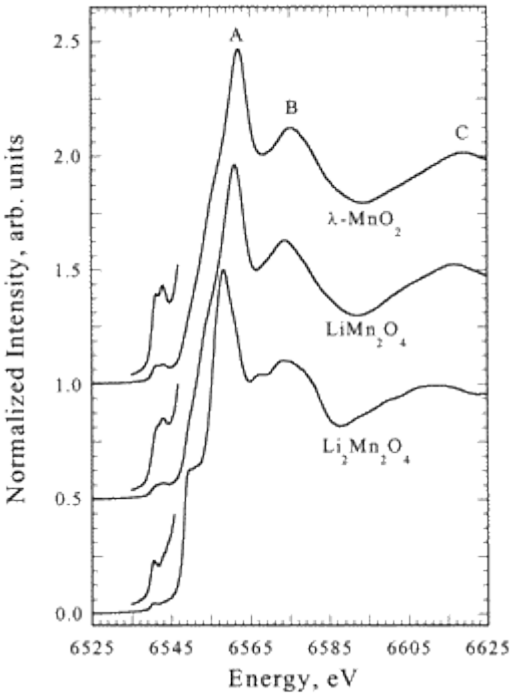

Figure 23. Mn K-edge XANES of λ-MnO_2, $LiMn_2O_4$ and $Li_2Mn_2O_4$. Reprinted with permission from Journal of Physical Chemistry B, Vol 104, Horne et al. Electronic structure of chemically prepared $Li_xMn_2O_4$ determined by Mn x-ray absorption and emission spectroscopies, pages no. 9587 – 9586, Copyright 2000 American Chemical Society.

The EXAFS studies show that the intensities of the Mn – O and Mn – Mn peaks decrease as more lithium is inserted to the structure.[173] The average manganese oxidation state gets closer to +3 when lithium concentration approaches x = 2 in $Li_{1+x}Mn_2O_4$ structure. The JT active Mn^{3+} ion causes distortion and the [Mn – O_6] loses its symmetry. The disorder lowers the intensity in EXAFS data.

If lithium replaces manganese ions as it intercalates, a cation mixed structure $LiMn_{2-x}Li_xO_4$ is formed. [141,174] The absorption edge in Mn K-edge XANES shifts now to higher energy compared to stoichiometric structure (Figure 24). This indicates that the amount of Mn^{4+} increases when more lithium is inserted to the structure, so lithium is replacing Mn atoms in the 16d sites.[141] When Li^+ intercalates to the structure, it "brings" only one electron with it. If at the same time it replaces one manganese ion, the structure is left with less electrons and the oxidation state of manganese needs to increase to balance the charge. A similar shift to higher energy in XAS could be noted if the structure would form cation vacancies *V* and be then $(Li_{1+x}Mn_{2-x})_{1-\delta}V_\delta O_4$. When x is high enough the manganese should oxidize to Mn^{5+} to maintain the charge balance and the absorption peak would shift to even higher energies. However, this kind of behavior have not been observed.[172]

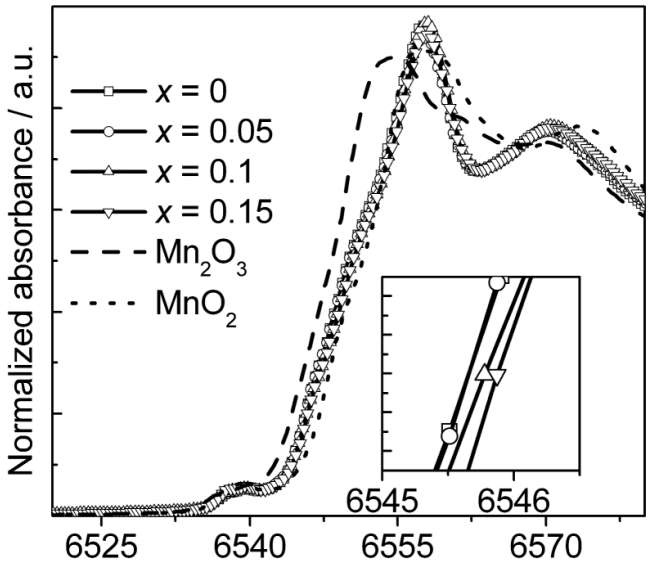

Figure 24. Mn K-edge XANES of a cation mixed structure $LiMn_{2-x}Li_xO_4$. Reproduced from Dalton Trans., 2011,40**,** 9752-9764 with permission of The Royal Society of Chemistry.

EXAFS studies on the cation mixed $LiMn_{2-x}Li_xO_4$ phases show that the Mn – O distance decreases as x increases. The conclusion makes sense since the oxidation state of Mn ions increases when x increases. When the smaller Mn^{4+} ions have higher concentration in the structure, the Mn – O distance decreases.[141,174]

The phase change may appear in multiple ways when the second lithium ion is inserted to the lithium manganese oxide. If Li^+ goes to the interstitial sites, the amount of Mn^{3+} increases, and the Mn K-edge shifts to lower energy in the absorption spectrum. In this case however, the cubic phase does not stay long, but the structure changes to tetragonal as

lithium concentration increases. If the Li^+ ions force out manganese as they intercalate, the structure becomes cation-mixed and the absorption edge in the Mn K-edge XANES shifts to higher energies.

6.3.1 Lithium migration pathway

For the structures that contain the second lithium ion, i.e. structure $Li_xMn_2O_4$, $1 < x$, the lithium ions occupy the 8a sites (as in the stoichiometric compound) and the excess lithium ions are expected to occupy the 16c sites.[18,147,176,177] The manganese oxide framework would allow also intercalation to the 8b interstitial sites, but lithium does not fill these sites because the lithium-manganese distance would become too short.[171]

The order of filling the interstitial sites is not so clear, since observations on first intercalating 8a and then 16c have been reported, as well as first 16c then 8a. In Sharma et al.[177] study the order of the occupancy of the lithium ions was found to depend on whether lithium was inserting or extracting in the structure. When lithium was inserting to $Li_{1+x}Mn_2O_4$, the Li^+ ions first occupied the 16c sites and after that the 8a sites. Upon the lithium extraction, the 8a sites first migrated to the 16c sites and lithium was then extracted from both sites.

In a cation mixed phase, lithium replaces manganese on the 16d sites and produces a manganese deficient structure.[155,178,179] Bianchini et al.[155] presented that lithium ions first occupy the 8a sites and then replace manganese atoms in the 16d sites. With computer modelling the lithium was found to fill the 16d sites when $1 < x < 1.33$ in $Li[Mn_{2-x}Li_x]O_4$ structures.[169]

When the amount of lithium increases even further, the phase is found to change to tetragonal. As said earlier the space group of the spinel is Fd3m. The tetragonal phase has a space group $I4_1/amd$. Figure 25 shows the crystal structures of the cubic $LiMn_2O_4$ and tetragonal $Li_2Mn_2O_4$. The 4a, 8c, 8d and 16h positions of the tetragonal structure correspond to the 8a, 16c, 16d and 32e positions in the cubic structure, respectively.

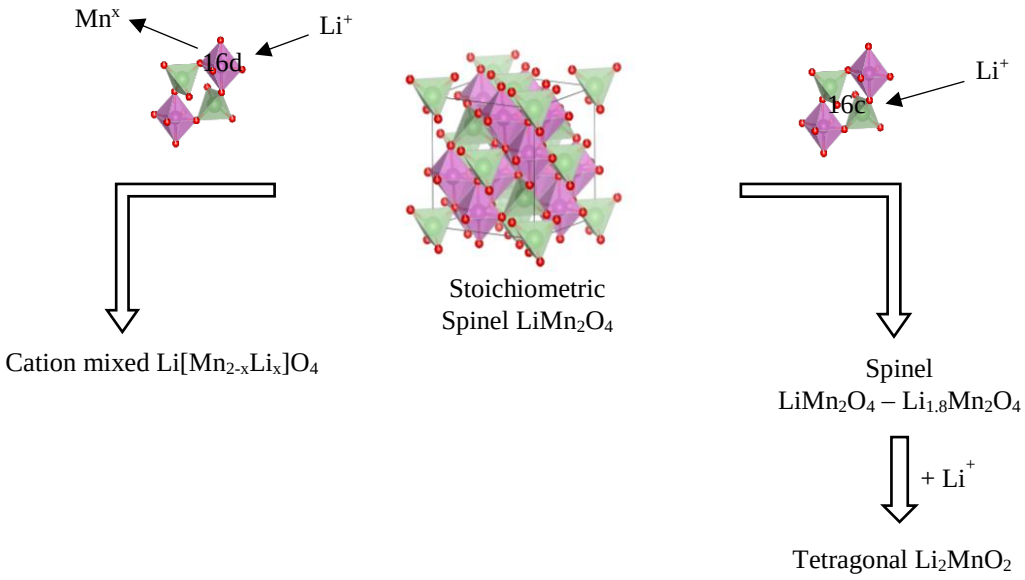

Figure 25. Schematic route of phase change when the second lithium ion intercalates. If Li^+ replaces the Mn atom on 16d site, the phase changes to cation mixed $Li[Mn_{2-x}Li_x]O_4$ (left side). If Li^+ intercalates to 16c sites, the spinel phase remain until $Li_{1,8}Mn_2O_4$ stoichiometry. The phase changes to tetragonal, when the structure exceeds the $Li_{1,8}Mn_2O_4$ stoichiometry (right side).

6.4 Conclusion on lithium insertion to spinel $LiMn_2O_4$

Lithium insertion to $Li_xMn_2O_4$ can be divided roughly to two regions: when $x < 1$, i.e. the first lithium intercalation, and when $x > 1$, i.e. second lithium intercalation. The lithium-less phase is called λ-MnO_2 and the stoichiometric structure is $LiMn_2O_4$.

When lithium is first intercalated to the λ-MnO_2 it fills the 8a interstitial sites and migrates through the 16c sites. Some studies have shown a phase change before the composition $Li_{0.5}Mn_2O_4$ is reached, but the XAS results support the conclusion that no structural change occurs when lithium inserts to λ-MnO_2.

When the lithium insertion continues and the stoichiometry exceeds $x = 1$, lithium can either intercalate to the 16c sites in addition to the already filled 8a sites, or replace manganese ions and intercalate to the 16d sites. If lithium occupies the 8a and 16c interstitial sites and the composition exceeds $Li_{1.8}Mn_2O_4$, the crystal structure changes to tetragonal.

Experimental

7 Sample preparation

7.1 Atomic layer deposition

All $Li_xMn_2O_4$ samples were deposited using atomic layer deposition. The deposition process was published earlier by Miikkulainen et al.[108] and Nilsen et al.[110]The depositions took place in two steps: first MnO_2 was deposited using $Mn(thd)_3$ (manganese - 2,2,6,6-trimethyl-3,5-heptanedionato) and O_3, second lithium was added by pulsing LiO^tBu and H_2O alternately. The amount of lithium was controlled by the number of LiO^tBu – H_2O cycles. All depositions were made in a Picosun Sunale R-150 reactor. The temperature for MnO_2 deposition and for lithium insertion was 225 °C.

The pulsing sequence for the MnO_2 deposition was $Mn(thd)_3 + O_3$ (0.5/3 + 5/5) meaning 0.5 s pulse of $Mn(thd)_3$ followed by 3 s purge, then 5 s pulse of O_3 and 5 s purge. [110] N_2 was used as a purging gas. The sequence was repeated 5000 times resulting in an approximately 100 nm thick MnO_2 film. The source temperature of the $Mn(thd)_3$ powder precursor was 160 °C. The pressure during the O_3 pulse was 14 hPa. A specific nozzle was used in the O_3 inlet to ensure gas distribution over the whole wafer. The nozzle was approximately 3 cm long and the other end of it was tilted towards the substrate.

The sequence for all lithium insertions was $LiO^tBu + H_2O$ (0.5/5 + 0.1/10). [108] N_2 gas was again used for purging. The cycle was repeated 10, 50, 100, 200 and 300 times. The source temperature of the powder LiO^tBu precursor was 160 °C. The water precursor line had a needle valve which was opened one round.

MnO_2 thin films were deposited on 50 mm and 150 mm Si(100) substrates. The 150 mm wafer was cut into smaller pieces, about 30 x 30 mm in size. The sample series of different lithium concentrations were deposited on those pieces. The 50 mm substrates were double-side-polished and they were used for residual stress measurements.

7.1.1 Annealing

The samples that had the highest lithium concentration were annealed. The annealing was done at 400 and 600 °C for 10 minutes under N_2 gas to prevent oxidation. The samples were loaded in the oven a day before and the oven was purged with N_2 overnight. This was done to ensure inert annealing conditions since the oven could not be pumped down into a vacuum and then be filled with N_2 gas.

7.2 List of samples

All together nine different $Li_xMn_2O_4$ samples were prepared in this study. In addition to MnO_2, five samples with different lithium concentrations were deposited. The lithium concentration was varied by changing the number of lithium deposition cycles. The cycle counts were 10, 50, 100, 200 and 300. Furthermore, the samples that were made with 200 and 300 lithium deposition cycles were annealed.

For clarity, the samples are named based on their preparation process. The sample made with 10 lithium deposition cycles is called 10-$Li_xMn_2O_4$, the sample made with 50 lithium deposition cycles is 50-$Li_xMn_2O_4$ and so on. The annealed samples have the annealing temperature after their names. The sample that was made with 200 lithium deposition cycles and was annealed at 600 °C for 10 minutes is 200-$Li_xMn_2O_4$-600, and so on. Table 1 shows a list of all the samples prepared in this study.

Table 1. The list of samples prepared for this study.

Sample name	**Preparation method**
MnO_2	MnO_2 film
10-$Li_xMn_2O_4$	MnO_2 film + 10 lithium deposition cycles
50-$Li_xMn_2O_4$	MnO_2 film + 50 lithium deposition cycles
100-$Li_xMn_2O_4$	MnO_2 film + 100 lithium deposition cycles
200-$Li_xMn_2O_4$	MnO_2 film + 200 lithium deposition cycles
300-$Li_xMn_2O_4$	MnO_2 film + 300 lithium deposition cycles
200-$Li_xMn_2O_4$-400	MnO_2 film + 200 lithium deposition cycles + Annealing in 400 °C for 10 minutes
200-$Li_xMn_2O_4$-600	MnO_2 film + 200 lithium deposition cycles + Annealing in 600 °C for 10 minutes
300-$Li_xMn_2O_4$-600	MnO_2 film + 300 lithium deposition cycles + Annealing in 600 °C for 10 minutes

8 Analysis of the samples

8.1 Time-of-flight elastic recoil detection analysis

Time of flight elastic recoil detection analysis (TOF-ERDA) was done in the Department of Physics in the University of Helsinki by Kenichiro Mizohata. The measurements were done with $^{79}Br^{7+}$ ions obtained from a 5 MV tandem accelerator (Model EGP-10-II).

8.2 Residual Stress

The residual stress of the thin films was determined using curvature measurements done with the Toho Technology FLX-2320-S –instrument and the stress was counted with Toho Technology Thin Film Stress Measurement System –software. The curvature measurements were done in VTT Technical Research Center of Finland Ltd by Oili Ylivaara.

The curvature was measured before and after the film deposition. The stress is counted using Stoney's equation (7).

$$\sigma_f = -\frac{1}{6}\frac{E_s}{1-v_s}\frac{t_s^2}{t_f}\left(\frac{1}{R_1}-\frac{1}{R_0}\right) \quad (7)$$

σ_f is the stress in thin film, E_s is the Young's modulus of the substrate, v_s the substrate's Poisson's ratio, t_s is the thickness of the substrate, t_f is the thickness of the thin film and R_0 and R_1 are the radii of curvature before and after the film deposition.

The stress measurements were done for plain MnO_2 film and after the lithium insertion. All stress measurements were made on films deposited on the 50 mm diameter double-side-polished Si substrates. Stress was measured in two directions along the substrate; x and y. x is the direction parallel to the substrate's flat, y is perpendicular to it. The measurements were made on the backside of the substrate, i.e. the opposite side than where the film was.

8.3 X-ray reflectivity

X-ray reflectivity (XRR) was used for measuring thickness, density and roughness of the MnO_2 films. Thickness was measured also after the lithium insertion. XRR measurements were done using a PANalytical X'pert PRO MPD diffractometer or a Rigaku SmartLab diffractometer.

8.4 X-ray diffraction

X-ray diffraction was measured using the PANalytical X'pert Pro MPD diffractometer as well as with the Rigaku SmartLab diffractometer. Both diffractometers use Cu K_α radiation that have wavelength λ = 1.5419 Å.

Figure 26 shows the measurement geometries for a five axis goniometer. The sample can be rotated around ω, χ and φ rotational axis, and the source and the detector can move through 5 goniometer axes (or similar geometries are achieved by moving the x-ray source and detector). This altogether enables 3D –scanning of the sample's reciprocal space.

In the θ-2θ measurement the sample is at the center of a goniometer circle, along which the source and detector are moving. In the θ-2θ mode the incident beam angle θ and the angle between the detector and the incident beam 2θ increases symmetrically (Figure 26a). Constructive interference from lattice plains parallel to the surface is focused to the receiving slit at the goniometer circle.[180]

Out-of-plane θ-2θ-diffraction was measured from all samples using Bragg Brentano (BB) focusing optics. BB was used because manganese in $Li_xMn_2O_4$ samples makes fluorescent radiation which lowers the signal-to-noise –ratio. BB optics utilize divergent x-rays to obtain high diffraction intensities with high resolution. 1.4 mm anti-scatter slit, 1/4˚ divergence slit, 0.04 soller slits and 0.18˚ parallel beam collimator were used.

Rocking-curve measurement i.e. ω-scan is done by keeping the 2θ angle between the incident beam and the detector constant, while the incident ω angle is changed (Figure 26b). Rocking-curve measurement is done on a particular peak in the θ-2θ diffractogram, hence it measures the orientation distribution of the selected reflection. The smaller the full-width-at-half-maximum is in the ω-scan, the better the crystallites are oriented. The rocking-curve measurement was done using parallel beam optics. The measurement was done on the MnO_2 sample.

In the in-plane $2\theta_\chi$ measurements the ω and 2θ angles are kept constant and below critical angle of total reflection, and the detector moves along the $2\theta_\chi$ direction (Figure 26c). This way the detector scans the lattice planes that are perpendicular to the surface of the sample.[181]

In-plane 2θχ diffraction was measured using a Rigaku Dtex250 detector as well as a scintillator counter (SC). The Dtex250 seemed a better option, because the background increases with SC and the fluorescence of manganese lowers the signal-to-noise –ratio so the diffraction peaks get lost to the background noise. Parallel multilayer mirror and parallel slit collimator (PSC) optical systems were used. Horizontal divergence of the incident beam was 0.5° and 0.1 mm incident slit and 15 mm long length limiting slit were used. The chosen constant 2θ and ω angles were 0.3°. In-plane parallel slit analyzer (PSA) of 0.5° was used together with receiving slits #1, #2 both being 20 mm of width. The attenuator was open. In this study $2\theta_\chi$ measurements were done for every sample.

α-scan is kind of a rocking curve measurement done in-plane. It measures the orientation distribution of a wanted reflection. In α-scan ω and 2θ are fixed and the detector is shifted to the $2\theta_\chi$ angle of wanted reflection (Figure 26d). Then the scanning is done by rising the detector up to 90 ° perpendicular to the sample stage. In the beginning the $2\theta_B$ is the same as $2\theta_\chi$, when after the α-scan the $2\theta_B$ is the same angle as 2θ. The scattering vector rises along with the movement of the detector. φ-scan is when the sample rotates around φ rotational axis and observing the changes in intensity (Figure 26e). The β-scan is similar to φ-scan, but the starting angle is fixed to a certain peak.[182] In this study the α- and $2\theta_B$- scans were made for MnO_2 sample.

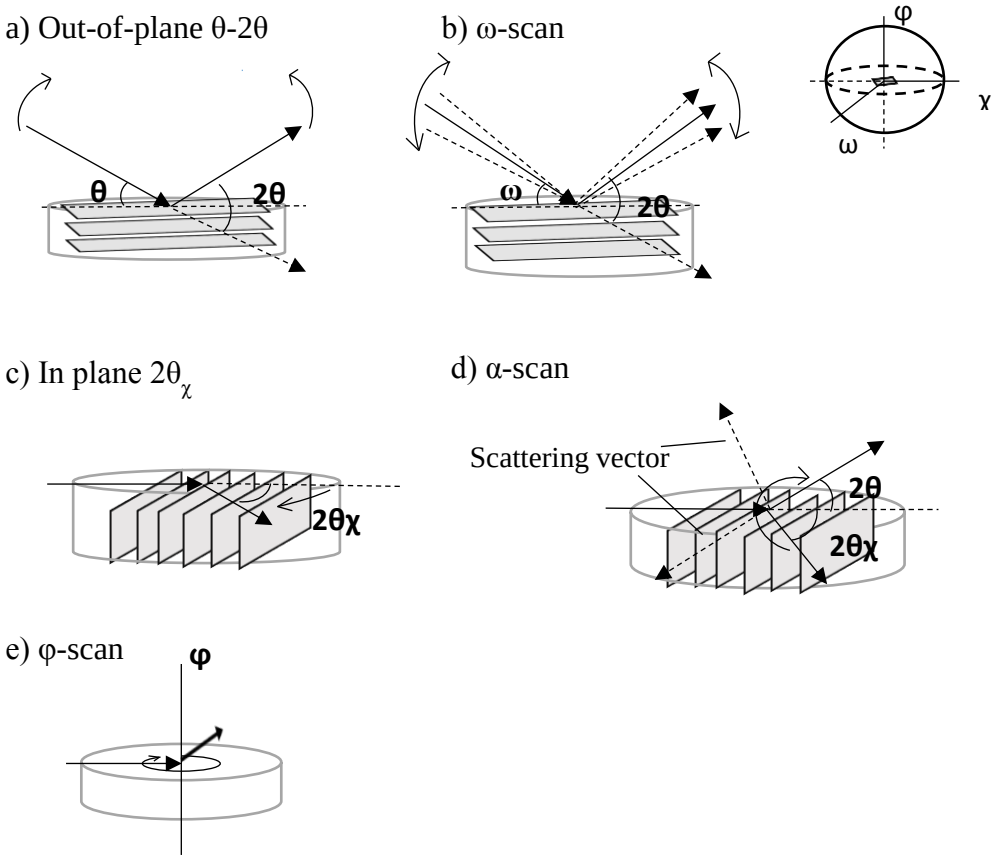

Figure 26. Measurement geometries of 5-axis goniometer.

All the diffraction patterns were compared to powder reference cards in International Centre of Diffraction Data database. The unit cell parameters were calculated using Equations 8 and 9 for orthorhombic and cubic structures respectively.

$$\frac{1}{d^2} = \frac{h^2}{a^2} + \frac{k^2}{b^2} + \frac{l^2}{c^2} \quad (8)$$

$$\frac{1}{d^2} = \frac{h^2 + k^2 + l^2}{a^2} \quad (9)$$

8.5 X-ray absorption

X-ray absorption measurements were done in two synchrotron facilities: in CLÆSS beamline at ALBA synchrotron radiation facility in Barcelona and in Helmholtz-Zentrum Berlin (HZB) synchrotron radiation source BESSY II. The measurements in BESSY II were done by Philipp Hönicke and Claudia Zech from Physikalisch-technische Bundesanstalt (PTB).

8.5.1 Manganese K-edge

EXAFS and XANES K-edge measurements were done for manganese in CLÆSS beamline 22 of ALBA synchrotron. During operation the electrons were accelerated up to 3 GeV in the booster and kept in the storage ring with a current of 148.7 mA. All the measurements were done at room temperature (27.7 °C) in 45° 2θ angle at the Mn K-edge 6.539 keV. Because of the hard X-rays used, the beam is penetrating through the whole thin film.

The radiation was emitted by a multipole wiggler and monochromatized by a Si(111) douple-crystal monochromator. The beam was focused to the sample by a toroidal focusing mirror. This way the achieved beam size was (1.5 x 0.5) mm^2.[183]

The samples were cut into 3 x 5 mm pieces and glued onto a sample holder of a liquid N_2 – cryo setup. All together five samples were mounted to the same batch to decrease the measurement time. Every measurement was done at 10^{-2} bar.

The samples were measured in total fluorescence yield (TFY) and in total electron yield (TEY) modes. TEY gives information only from the surface of the film, because the measured secondary electrons do not have high enough mean-free-path to escape deeper from the sample. TFY gives information throughout the whole film. The three powder

standards MnO (Sigma-Aldrich), $LiMn_2O_4$ (Sigma-Aldrich) and MnO_2 (Sigma-Aldrich) were measured in transmission mode.

The TFY signal was collected with an XR-100SDD detector and TEY by measuring the drain current of the samples. All the measurements were done in a continuous mode and calibrated by fixing the first peak of the measured Mn metal foil to 6.539 keV. The data was collected up to k = 18 $Å^{-1}$ with a scanning sequence: 6400 – 6520 eV with steps of 1 eV (total of 120 points in 60 seconds), 6521 – 6582 eV with steps of 0.2 eV (total of 306 points in 153 seconds) and 6582.2 – 7782.8 with steps of 1 eV (total of 1200 points in 600 seconds). About 10 scans per sample were made to improve the signal-to-noise ratio of the measurement.

The data analysis was done by the Helsinki Electronic Structure, Imaging and X-ray Scattering research group in the physics department of the University of Helsinki.[184] The XANES spectra were analyzed using ATHENA program with an IFEFFIT together with Fityk software packages. The EXAFS data was least-square fitted to a theoretical model using ARTEMIS and also the IFEFFIT package. The theoretical models were MnO_2 pyrolusite $P4_2/mnm$ and $LiMn_2O_4$ spinel (Fd-3m:1).

8.5.2 Manganese L-edge and Oxygen K-edge

Manganese L-edge and oxygen K-edge x-ray absorption measurements were done in planar grating monochromator (PGM) beamline[185] at the Helmholtz-Zentrum Berlin (HZB) synchrotron radiation source BESSY II. The measurements were done in collaboration with Physikalisch-technische Bundesanstalt (PTB) with PTB's XRS instrument.[186]

Mn L-edge XANES was measured for all the samples, except for 200-$Li_xMn_2O_4$-400C. Again, 5 samples were mounted at the same time to reduce the measurement time. Figure 27 shows the setup of the sample holder. The measurement was done at the Mn L-edge 0.6371 keV.

The O K-edge XANES was measured from the MnO_2, 200-$Li_xMn_2O_4$, 300-$Li_xMn_2O_4$, 200-$Li_xMn_2O_4$-600C and 300-$Li_xMn_2O_4$-600C samples. The measurements was done at the O K-edge absorption energy 0.5249 keV. The incident beam energy was changed in a way that the sample chamber was not opened in between the Mn L-edge and O K-edge measurements.

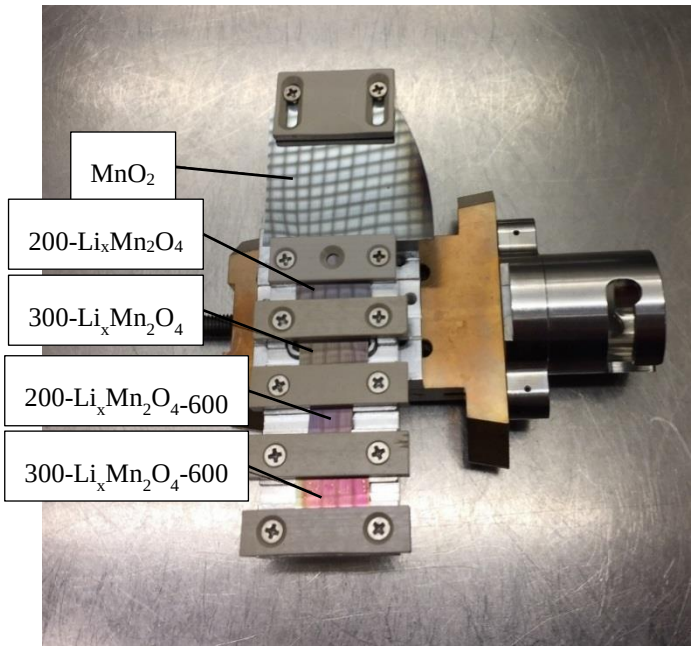

Figure 27. Sample holder in the PGM beamline at BESSY II. From top to bottom samples MnO_2, 200-$Li_xMn_2O_4$, 300-$Li_xMn_2O_4$, 200-$LI_xMn_2O_4$-600 and 300-$Li_xMn_2O_4$-600.

Because the incident X-ray beams are in the soft X-ray region, their penetration depth is a function of the incident angle. In all the measurements the incident angle was varied to make a depth scan of the films. The chosen incident beam angles were 0.5°, 1°, 5° and 45°. The first 0.5° probes only the surface of the film, 1° and 5° penetrate deeper, and 45° angle measures the bulk. The penetration depths at the 1° and 5° angles were estimated to be around 5-10 nm.

8.6 X-ray photoelectron spectroscopy

X-ray photoelectron spectroscopy (XPS) measurement and result analysis was done in the Department of Physics of University of Helsinki by Kristoffer Meinander. The measurement was done using an Argus Spectrometer operating at a pass energy of 20 eV. Spectrometer uses K_α radiation from standard Mg source at a photon energy of 1253.6 eV. The measurement was done in vacuum with 1 x 10^{-10} mbar pressure using 1 eV steps (0.2 seconds/step). The measurement was done for MnO_2 sample. MnO and Mn_2O_3 powders were used as references. The results were analyzed with the CasaXPS software using Biesinger model.[187]

9 Results

In this study the $Li_xMn_2O_4$ samples were prepared using ALD by first depositing MnO_2 with $Mn(thd)_3$ and O_3 and then inserting lithium separately into the film by pulsing LiO^tBu and H_2O.[108,110] The lithium concentration was controlled by the number of LiO^tBu-H_2O cycles (10, 50, 100, 200 and 300). The MnO_2 deposition and lithium insertion were done at 225 °C. The samples are named after lithium insertion cycle counts (10-$Li_xMn_2O_4$, 50-$Li_xMn_2O_4$ and so on). Post-deposition annealing was done for 200-$Li_xMn_2O_4$ at 400 and 600 °C and 300-$Li_xMn_2O_4$ at 600 °C. The annealing temperature is written after the sample name for those particular samples.

9.1 Film thickness

A MnO_2 film was deposited on a 150 mm Si wafer and then cut to 16 pieces (Figure 28) to which lithium was then inserted. The thickness of MnO_2 was measured using XRR. The measured thicknesses from the different pieces of the wafer are in Table 2.

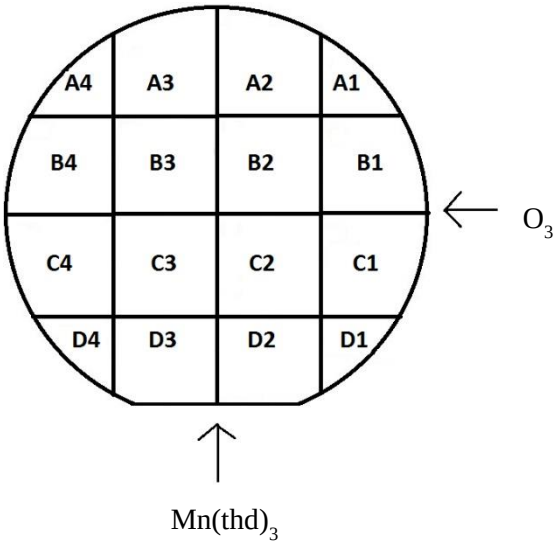

Figure 28. Silicon wafer on which MnO_2 was deposited. After the film deposition the wafer was cut to 16 pieces for the lithium insertion.

Thickness variation across the MnO_2 film on the 150 mm substrate is approximately 17.5 %. The thinnest part of the film is near the edges on the column 4. During the film growth optimization process, around 10 % thickness variation on 150 mm substrate was achieved at best. Ozone is pulsed on the substrate from the right side of the wafer, so it may have some

difficulties to react all the way at the far left. MnO_2 catalyzes decomposition of ozone, so the film destroys the ozone pulse as it tries to distribute. The MnO_2 film deposited on a 50 mm Si substrate for the stress measurements had significantly lower thickness profile than the film on the 150 mm substrate.

The thicknesses of the films were measured also after the lithium insertion. The film thickness increased around 2 - 9 % depending on the amount of lithium. The thicknesses for each sample as well as the percentage difference compared to MnO_2 are in Table 2.

Table 2. Film thickness on different areas of the original MnO_2 wafer before and after lithium insertion.

Sample	**Place**	**Thickness before lithium insertion**	**Thickness after lithium insertion**	**Difference**
		nm	*nm*	*± %*
MnO_2	A2	90	-	-
MnO_2	A3	84.5	-	-
MnO_2	B4	82.5	-	-
MnO_2	C4	85.5	-	-
MnO_2	D3	89.5	-	-
300-$Li_xMn_2O_4$	D2	92	100–103	± 8.7 %
200-$Li_xMn_2O_4$	C2	-	-	-
100-$Li_xMn_2O_4$	C3	100	109	± 9.0 %
50-$Li_xMn_2O_4$	B3	96	100	± 4.2 %
10-$Li_xMn_2O_4$	C3	100	98	± 2.0 %

9.1.1 Annealing

The 200-$Li_xMn_2O_4$-400 sample did not show any changes in the appearance after the annealing at 400 °C. The 200-$Li_xMn_2O_4$-600 and 300-$Li_xMn_2O_4$-600 samples had some milky-like appearance and some inhomogeneities on the surface after the annealing at 600 °C.

9.2 Residual Stress

The residual stress was measured after the MnO_2 thin film deposition as well as after 300 deposition cycles of lithium. The measurements were done on the 300-$Li_xMn_2O_4$ samples,

because the 300-$Li_xMn_2O_4$ was fully converted to the cubic spinel. The stress results for every sample in both measurement directions are in Table 3.

The residual stress of MnO_2 films was around 570 MPa in the x measurement direction and around 550 MPa in the y direction. The total residual stress of MnO_2 film was around 560 MPa. The MnO_2 film was under tensile stress. The stress result is comparable to other ALD grown transition metal oxide films.

The residual stress changes to compressive when lithium is inserted into the film. The compressive stress in 300-$Li_xMn_2O_4$ is around -2300 MPa in the both measurement directions. The stress is opposite and almost four times as large compared to the plain MnO_2 film.

The large compressive stress for in 300-$Li_xMn_2O_4$ formed when lithium ions intercalated to the β-MnO_2 structure. According to the XRR results, films swelled when lithium was inserted. The swelling caused the film to expand and when the substrate did not expand, the film experienced high compressive stress. The unit cell expansion should show a clear peak shift in XRD diffractograms compared to the reference values. This is indeed the case for all the samples in this study as will be discussed later.

Table 3. Residual stress in MnO_2 films as well as 300-$Li_xMn_2O_4$ thin films.

Sample	**Orientation**	**Stress after MnO_2 deposition**		**Stress after lithium insertion**
		MPa		*MPa*
1	x	561.1	556.7	-2311.4
	y	541.6	537.8	-2425.8
2	x	542.9	544.6	-2236.4
	y	503.1	518.1	-2203.1
3	x	569.6	569.4	-2410.6
	y	540.0	542.5	-2373.1
4	x	616.1	620.6	-2226.9
	y	584.7	506.2	-2242.1

9.3 Sample composition

Figure 29 shows the TOF-ERDA depth profiles of MnO_2, 50-$Li_xMn_2O_4$ and 200-$Li_xMn_2O_4$. The depth profiles show that lithium is mostly on the surface of the films in 10-$Li_xMn_2O_4$,

50-$Li_xMn_2O_4$ and 100-$Li_xMn_2O_4$ samples. In the 200-$Li_xMn_2O_4$ and 300-$Li_xMn_2O_4$ samples the lithium is distributed throughout the whole film.

a) MnO_2 b) 50-$Li_xMn_2O_4$ c) 200-$Li_xMn_2O_4$

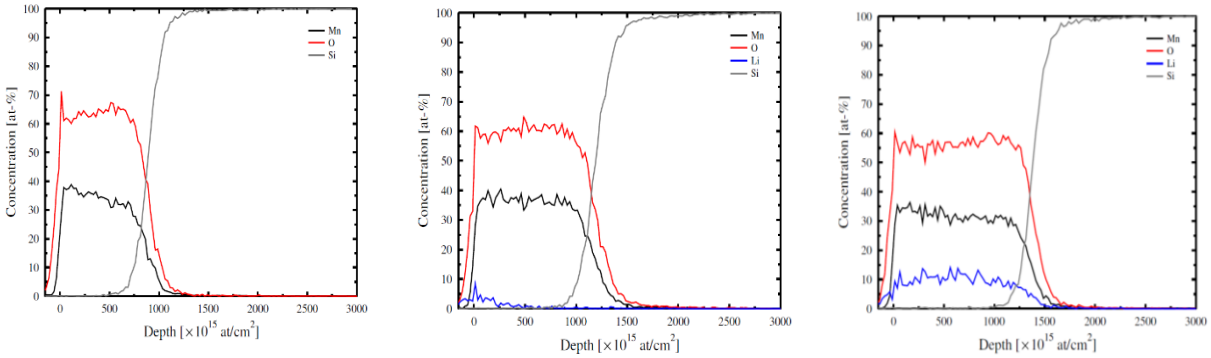

Figure 29. TOF-ERDA depth profiles of a) MnO_2, b) 50-$Li_xMn_2O_4$ and c) 200-$Li_xMn_2O_4$.

Compositional analysis by TOF-ERDA shows that the increase of the lithium content is almost linear as a function of the number of lithium insertion cycles, except for 100-$Li_xMn_2O_4$ sample (Figure 30). The 100-$Li_xMn_2O_4$ sample has more lithium than expected, when compared to the other samples. The stoichiometric compositions of every sample are presented later in Table 4.

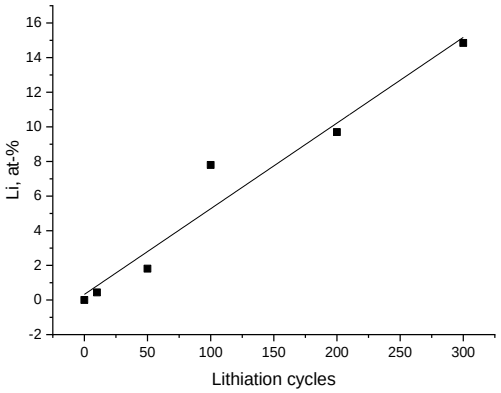

Figure 30. The amount of lithium in the samples as a function of lithium insertion cycles.

9.4 Crystalline phases of the samples

9.4.1 MnO_2

The out-of-plane XRD of MnO_2 is shown in Figure 31. It has three reflections from MnO_2, at 2θ angles 20.3°, 41.3° and 44.5°. The most intense reflection at 41.3° was identified as (200) of the tetragonal pyrolusite β-MnO_2. The sharp and narrow reflections at angles 33.0°, 46.1°, 46.3° and 47.7° are most probably from the Si substrate.

The reflection at 20.3° could be (100) of β-MnO_2 as reported earlier by Nilsen et al.[110,114] The reflection should be forbidden for symmetry reasons for the tetragonal pyrolusite space group $P4_2/mnm$. However, the (100) diffraction can appear if the stress in the film deforms the structure to be slightly orthorhombic instead of tetragonal, as suggested by Nilsen et al.[110] The reflection at 20.3° can also appear as a result of another impurity phase.

The small reflection on angle 44.5° does not fit to the pyrolusite β-MnO_2 diffraction pattern either. As said, because the (100) reflection is visible, the structure may not be perfectly tetragonal, but slightly orthorhombic. This can change the space group of the crystal structure and produce also the additional small peak.

The MnO_2 sample seems to have (*h*00) orientation in the out-of-plane direction. Rocking curve measurements were done for the (200) reflection at 41.3° 2θ angle (Figure 31b). The full-width-at-half-maximum of the rocking curve peak is 7.5° which is comparable to Nilsen et al.[114] results. The rocking-curve of the (200) reflection is wide, so the orientation distribution of (200) is quite wide.

The (301) reflection was also scanned in attempt to get more information on the orientation of the films. The rocking curve for the (301) reflection was measured in 72.3° 2θ angle (Figure 31c). As can be seen from the curve, the reflection (301) is visible, which confirms that the films are not perfectly (*h*00) out-of-plane oriented, but have some orientation distribution.

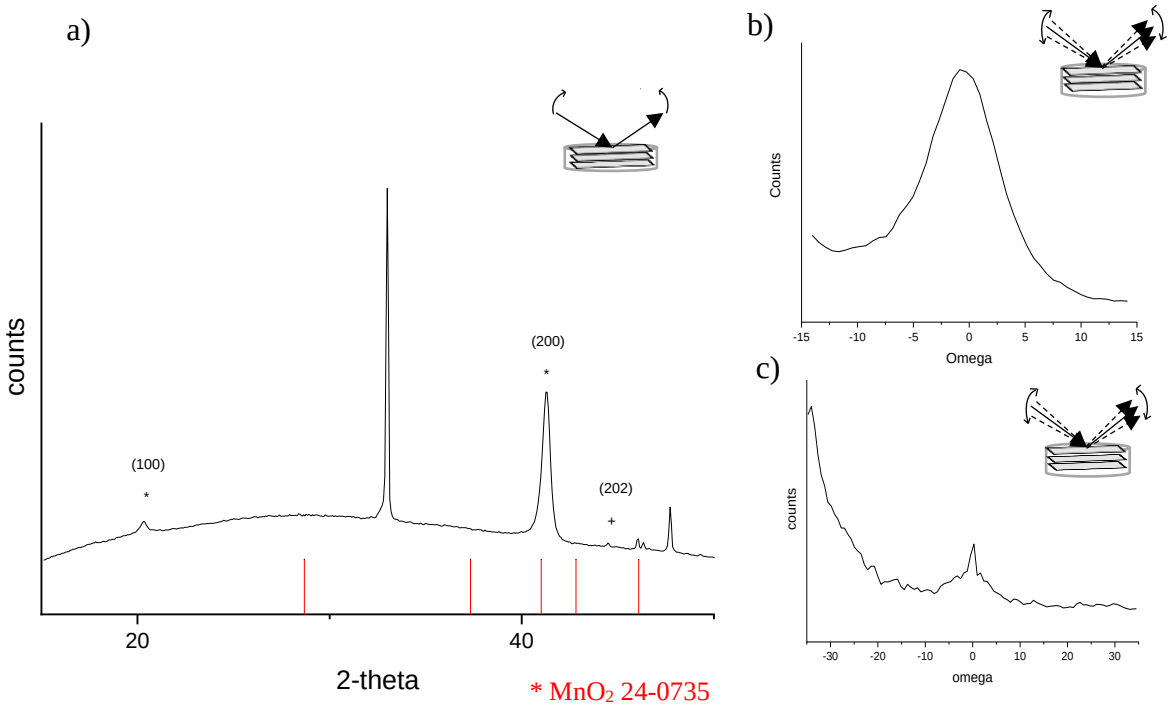

Figure 31. a) An out-of-plane 2θ diffraction pattern of MnO_2. b) A rocking-curve of the (200) reflection. c) A rocking-curve of the (301) reflection.

Nilsen et al. also studied the effect of the substrate on the MnO_2 thin films.[114] MnO_2 was deposited on a Kapton^{TM} foil and on glass capillaries resulting in a polycrystalline β-MnO_2 film. Depositions were done also on Si(100) which had a native oxide layer, as well as on soda-lime glass, and they both had clear (*h*00) orientation with the forbidden (100) reflection. To further investigate the forbidden peak, Nilsen et al. scraped and crushed the deposited films. After the mechanical treatment, the (100) reflection had vanished. However Nilsen et al. stated that even if it would be easy to explain the (100) reflection with stress based on these results, it may not be the only reason.

The in-plane XRD pattern of MnO_2 is shown in Figure 32a. It shows β-MnO_2 (011), (020), (002), (031), (112) and (230) reflections. No (110) reflection was detected. The sharp reflections at angles 34.0°, 58.3° and 77.5° are from the Si substrate.

The (110) reflection missing in the $2\theta_\chi$ in-plane measurement was identified using α- and $2\theta_B$- scans. Both scans had wide (110) peaks (Figures 32b and 32c). Hence the β-MnO_2 has (*h*00) out-of-plane orientation, but no specific in-plane orientation.

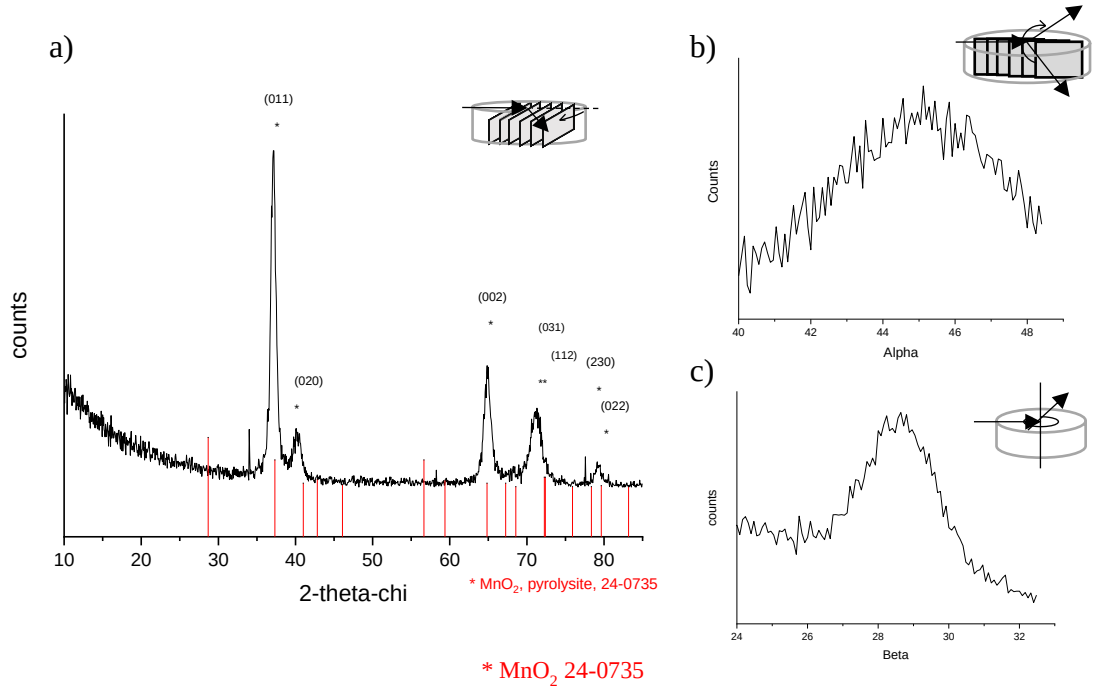

Figure 32. a) An in-plane $2\theta_\chi$ diffraction pattern of MnO_2. b) α –scan of the reflection (110). c) $2\theta_B$ –scan of the reflection (110).

The unit cell parameters were calculated using Equation 8 and they are a = 4.37 Å, b = 4.44 Å and c = 2.88 Å. The space group of the pyrolusite β-MnO_2 is $P4_2/mnm$,[188] but because of the additional (100) reflection, the space group is most probably changed. Nilsen et al.[114] suggested that the space group for the alternative pyrolusite phase β'-MnO_2 is $P4_2/m$ but it has not been firmly established so far.

9.4.2 $LiMn_2O_4$

The phase identification was a challenge for the samples that had not been converted completely to the stoichiometric spinel $LiMn_2O_4$ as will be discussed later. The sample that has the highest lithium concentration, 300-$Li_xMn_2O_4$, was completely converted to the cubic spinel with a space group Fd-3m.[189] The 300-$Li_xMn_2O_4$ sample as well as all the un-annealed samples seemed to be a mixture of two spinel phases. One of the identified was an un-stoichiometric spinel $Li_{1-x}Mn_2O_4$ from reference card 38-0789 and the other one was a stoichiometric spinel $LiMn_2O_4$ from reference card 35-0782.

The out-of-plane XRD diffractogram has (111), (311) and (400) reflections (Figure 33a). The sharp and narrow reflections at the 2θ angels 46.1°, 46.4° and 47.8° are from the substrate. The reflections that correspond to the stoichiometric $LiMn_2O_4$ are shifted to lower

angles compared to the reference pattern. The (111) and (311) reflections are shifted by about 1.4°. The (400) reflection, which is probably from the $Li_{1-x}Mn_2O_4$ phase, is shifted by about 0.32°. The in-plane XRD (Figure 33b) has (111), (331) and (571) reflections that correspond to the $LiMn_2O_4$ phase. The (222) and (571) reflections have shifted 0.65° to lower angles. The peaks are shifted due to high residual stress in the films as discussed earlier.

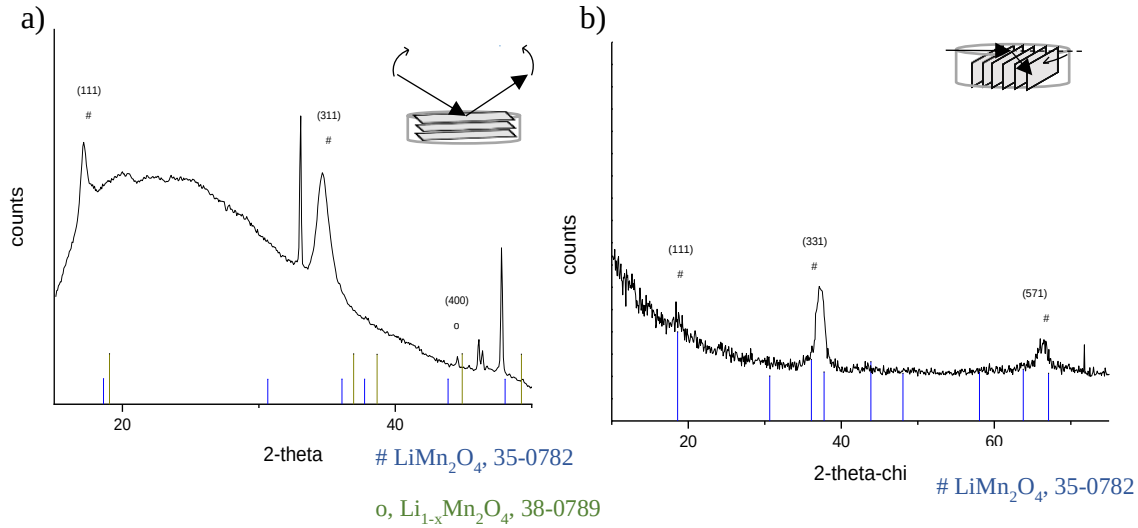

Figure 33. a) An out-of-plane 2θ diffractogram of 300-$Li_xMn_2O_4$. b) An in-plane $2\theta_\chi$ diffraction pattern of 300-$Li_xMn_2O_4$.

9.4.3 Phase evolution

Figure 34 compares the out-of-plane 2θ diffractograms of every sample. The phase change from the pyrolusite β-MnO_2 to the spinel $LiMn_2O_4$ can be identified. The (200) β-MnO_2 reflection around 41.3° diminishes, as well as the forbidden (100) reflection, when the amount of lithium is increased. At the same time the spinel reflections (111), (311) and (400) increase. Reflections that are observed from every sample at the 2θ angles 33.0°, 46.1°, 46.7° and 47.7° are from the Si substrate. At around 32.6° is an "impurity"-peak, which is thought to be caused by an existence of a lithium rich $Li_{2-z}MnO_2$ phase. The reflection is seen in the 10-$Li_xMn_2O_4$ and 100-$Li_xMn_2O_4$ samples next to the Si peak at 33.0°.

Only one reflection from spinel phase is visible at an angle 44.5° in the out-of-plane diffractogram of 10-$Li_xMn_2O_4$. This reflection is indexed as (400) in the $Li_{1-x}Mn_2O_4$ reference card. All the following samples with higher lithium concentrations have three

spinel reflections that are indexed as (111) and (311) for the stoichiometric $LiMn_2O_4$ and (400) for the $Li_{1-x}Mn_2O_4$. The (400) reflection of $Li_{1-x}Mn_2O_4$ diminishes and, in comparison, the (111) and (311) reflections of $LiMn_2O_4$ increase as the lithium concentration increases.

The peaks corresponding to β-MnO_2 phase decrease in a way that in 100-$Li_xMn_2O_4$ sample the (200) reflection of β-MnO_2 has clearly less intensity than (111) and (311) of $LiMn_2O_4$. The 200-$Li_xMn_2O_4$ and 300-$Li_xMn_2O_4$ samples do not have any remarks of the β-MnO_2.

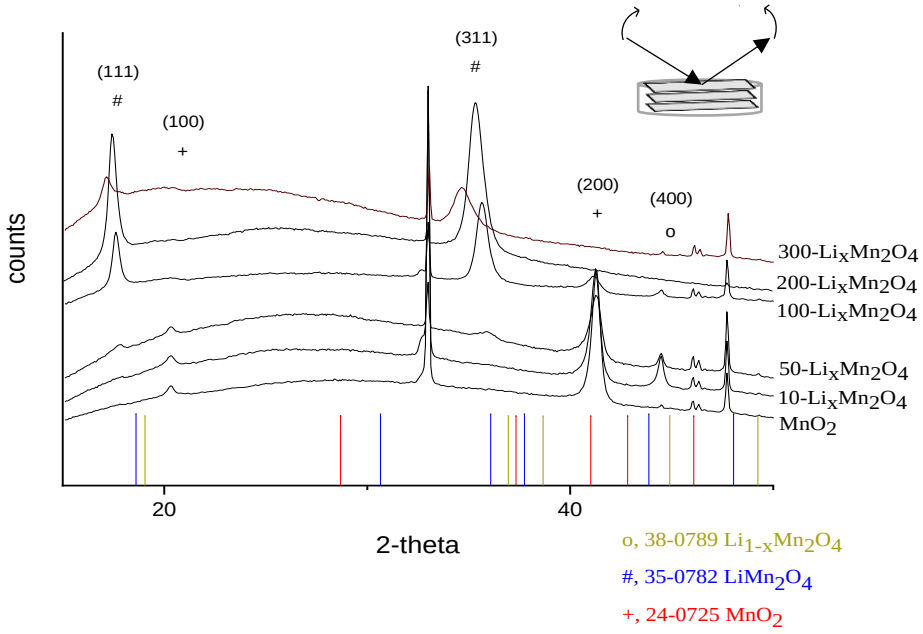

Figure 34. Comparison of out-of-plane 2θ diffraction patterns of every sample.

The reflections shift to lower 2θ angles in the out-of-plane XRD when the lithium concentration increases. The shift indicates that the unit cell expands as the lithium concentration increases. The shift was notable only for the (111) and (311) reflections, so only when the lithium concentration increased above $x \approx 0.5$. The expansion occurs due to an increase of Mn^{3+} ion concentration and the result agrees well with the other studies as described earlier.[154,157,158]

Based on the literature, during the intercalation of the first Li^+ ions to β-MnO_2 the pyrolusite structure can receive only a certain amount of lithium to its square channels. After further lithium insertion, the pyrolusite/spinel phase change takes place. In this study, the samples that have $x < 0.5$ have the same orientation as β-MnO_2 and the lithium is distributed only on the surface of the film. By contrast, the samples which have $x > 0.5$ have clear (111) and

(311) reflections of $LiMn_2O_4$ and the lithium has distributed throughout the whole film. It appears that the pyrolusite/spinel phase change occurs when $x \approx 0.5$, and because of the phase change Li^+ ions are able to intercalate deeper and throughout the whole film. The 100-$Li_xMn_2O_4$ sample has the composition of $Li_{0.52}Mn_2O_4$ where $x = 0.52$, so it represents the composition boundary for the pyrolusite/spinel phase change.

The in-plane x-ray diffraction was measured also on all samples in between $2\theta_\chi$ angles 10-85° (Figure 35). The phase change is again notable when the MnO_2 pyrolusite reflections (011), (002), (103), (113), (230) and (022) diminish and $LiMn_2O_4$ spinel reflections (111), (131), (440) and (351) appear as the lithium concentration increases. The in-plane diffraction patterns fit better to the $Li_{1-x}Mn_2O_4$ reference than to the stoichiometric $LiMn_2O_4$ reference.

In Figure 35 the reflection at 37.2° does not evolve in any way, whereas all the other MnO_2 phase related reflections diminish. For the pyrolusite the (011) reflection is at an angle 37.2° and for the spinel the (131) reflection is at 36.0°. Because of the stress in thin films, the spinel (131) reflection can be shifted to higher angles, and it may overlap with the pyrolusite (011) reflection. The suggestion for the fixed peak position at 37.5° is that pyrolusite changes to spinel that is stressed and therefore its (131) reflection is shifted to higher angles.

200-$Li_xMn_2O_4$ is the first sample that shows only the spinel phase. The samples that have lower lithium concentrations are mixtures of the pyrolusite and spinel. The 200-$Li_xMn_2O_4$ sample has probably some other phases as well, because it shows a peak at around 47.4° in the in-plane XRD. This impurity peak fits with the same $Li_{2-z}MnO_2$ reference card as the earlier discussed impurity peaks in the 10-$Li_xMn_2O_4$ and 100-$Li_xMn_2O_4$ samples.

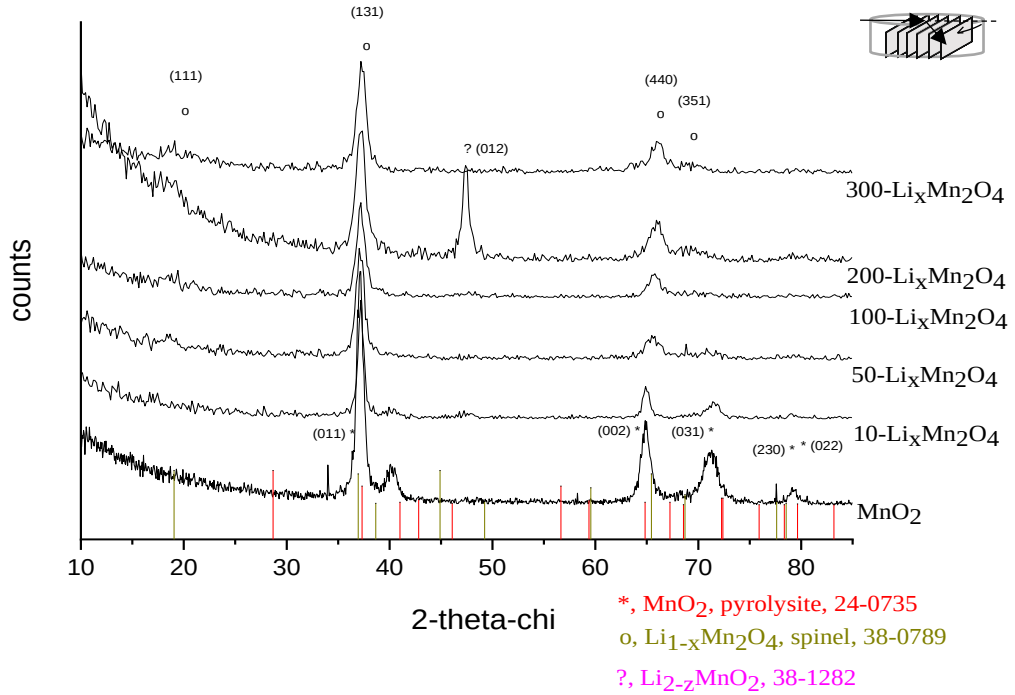

Figure 35. An in-plane $2\theta_\chi$ diffraction patterns of every sample.

The 300-$Li_xMn_2O_4$ sample has a composition $Li_{1.06}Mn_{2.04}O_4$ which is close to the stoichiometric cubic spinel. However, its in-plane diffractogram fits better to the $Li_{1-x}Mn_2O_4$ reference than to the $LiMn_2O_4$ reference. One reason for the nonstoichiometric phase may be that not all lithium goes into the correct interstitial sites of the manganese-oxide network to enable complete phase change. Lithium may also end up in alternative sites or to the grain boundaries of the structure. Lithium is highly mobile and manganese may exist in multiple oxidation states which enables different phases inside the same sample. If this is the case, the TOF-ERDA results can show the $Li_{1.06}Mn_{2.04}O_4$ composition, even when the phase is still non-stoichiometric. However, the out-of-plane XRD had peaks also from the stoichiometric $LiMn_2O_4$ phase. Maybe some parts of the structure have converted to the stoichiometric $LiMn_2O_4$, some are still lithium-deficient, and the excess lithium has found its place in grain boundaries.

As noted earlier, the β-MnO_2 peaks remain at about the same angles in every sample. The unit cell parameters are a = 4.37 Å, b = 4.44 Å and c = 2.88 Å. Some shrinkage occurs for the $Li_{1-x}Mn_2O_4$ phase when lithium concentration increases. The shrinking occurs at least in two dimensions from a = 8.34 Å (10-$Li_xMn_2O_4$) to a = 8.19 Å (300-$Li_xMn_2O_4$) and b = 8.04 Å (10-$Li_xMn_2O_4$) to b = 8.00 Å (300-$Li_xMn_2O_4$). The third direction seems to stay constant

in all samples, c = 8.15 Å. The orthorhombic unit cell is probably a result of the high residual stress in the samples.

The $LiMn_2O_4$ phase is probably strained at least in one direction, since the unit cell had two clearly different dimensions. One dimension varies randomly between a = 8.70 – 8.92 Å (50-$Li_xMn_2O_4$, 100-$Li_xMn_2O_4$, 200-$Li_xMn_2O_4$, 300-$Li_xMn_2O_4$), and the other increases from b = 8.30 Å (50-$Li_xMn_2O_4$) to b = 8.57 Å (300-$Li_xMn_2O_4$). In relation to earlier hypothesis, at the same time when Li^+ ions diffuse deeper to the film, the $Li_{1-x}Mn_2O_4$ unit cell contracts and the stoichiometric $LiMn_2O_4$ unit cell expands. The accurate unit cells, stoichiometries and lithium distributions for every sample are shown in Table 4.

Table 4. Stoichiometry, unit cell parameters and lithium distribution in all samples. (The parameters are calculated utilizing XRD results.)

Sample	Stoichiometry	Phase and unit cell	Li distribution
MnO_2	$Mn_{1,01}O_2$	β-MnO_2 : *a* = 4.37 Å *b* = 4.44 Å *c* = 2.88 Å	No lithium
10-$Li_xMn_2O_4$	$Li_{0,014}MnO_2$	β-MnO_2 : *a* = 4.38 Å *b* = 4.44 Å *c* = 2.87 Å $Li_{1-x}Mn_2O_4$: *a* = 8.15 Å	Surface
50-$Li_xMn_2O_4$	$Li_{0,11}Mn_2O_4$	β-MnO_2 : *a* = 4.38 Å *b* = 4.44 Å *c* = 2.87 Å $Li_{1-x}Mn_2O_4$: *a* = 8.15 Å *b* = 8.34 Å *c* = 8.04 Å $LiMn_2O_4$: *a* = 8.89 Å *b* = 8.30 Å	Surface
100-$Li_xMn_2O_4$	$Li_{0,52}Mn_2O_4$	β-MnO_2 : *a* = 4.39 Å *b* = 4.44 Å *c* = 2.87 Å $Li_{1-x}Mn_2O_4$: *a* = 8.15 Å *b* = 8.30 Å *c* = 8.03 Å $LiMn_2O_4$: *a* = 8.70 Å *b* = 8.35 Å	Surface
200-$Li_xMn_2O_4$	$Li_{0,65}Mn_2O_4$	$Li_{1-x}Mn_2O_4$: *a* = 8.15 Å *b* = 8.28 Å *c* = 8.02 Å $LiMn_2O_4$: *a* = 8.75 Å *b* = 8.38 Å	The whole film
300-$Li_xMn_2O_4$	$Li_{1,06}Mn_{2,04}O_4$	$Li_{1-x}Mn_2O_4$: *a* = 8.15 Å *b* = 8.19 Å *c* = 8.00 Å $LiMn_2O_4$: *a* = 8.92 Å *b* = 8.57 Å	The whole film

9.4.4 Effect of annealing

In general, strain in films relaxes during annealing, which makes the reflections in the out-of-plane XRD to shift to higher 2θ angles in both 200-$Li_xMn_2O_4$-600 and 300-$Li_xMn_2O_4$-600 samples (Figures 36a and 37a). For both samples, the in-plane XRD shows how the peaks split and shift to fit the stoichiometric $LiMn_2O_4$ reference. Furthermore, the out-of-plane XRD shows that the annealing makes the $LiMn_2O_4$ phase split to β-MnO_2 and $LiMn_2O_4$ in 200-$Li_xMn_2O_4$-600 (Figure 36a). However, the in-plane XRD does not show any

β-MnO_2 reflections, or they are overlapping with the cubic spinel peaks. The 200-$Li_xMn_2O_4$-400 sample did not show any differences in XRD compared to the un-annealed sample.

The additional reflection in 300-$Li_xMn_2O_4$-600 at 32.6° can be some kind of impurity, and it fits to the lithium rich $Li_{2-z}MnO_2$ phase similar to the earlier impurity peaks in the other samples. The reflection also fits with the hausmannite Mn_3O_4 phase (reference card 002-1062), but because the composition of the sample is close to $LiMn_2O_4$ (according to TOF-ERDA results) and the MnO_2 sample did not have any signs of Mn_3O_4, the $Li_{1-z}MnO_2$ phase appears more probable. On the other hand, lithium insertion reduces manganese and annealing could help to separate the parts that have high lithium concentration from the Mn_3O_4 phase, so the existence of the Mn_3O_4 cannot be excluded completely.

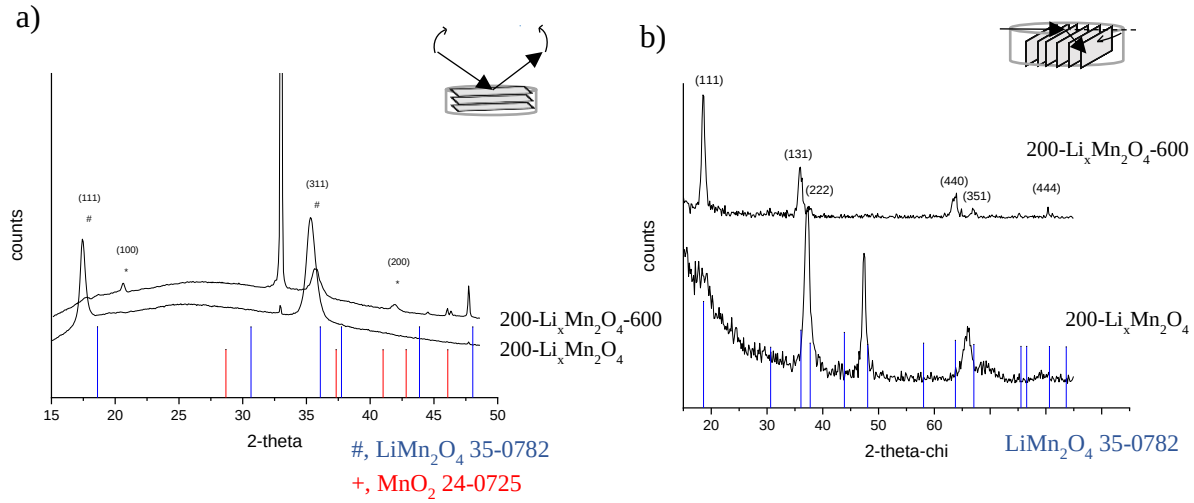

Figure 36. a) Out-of-plane 2θ diffraction patterns of 200-$Li_xMn_2O_4$ and 200-$Li_xMn_2O_4$-600. b) In-plane $2\theta_\chi$ diffraction patterns of 200-$Li_xMn_2O_4$ and 200-$Li_xMn_2O_4$-600.

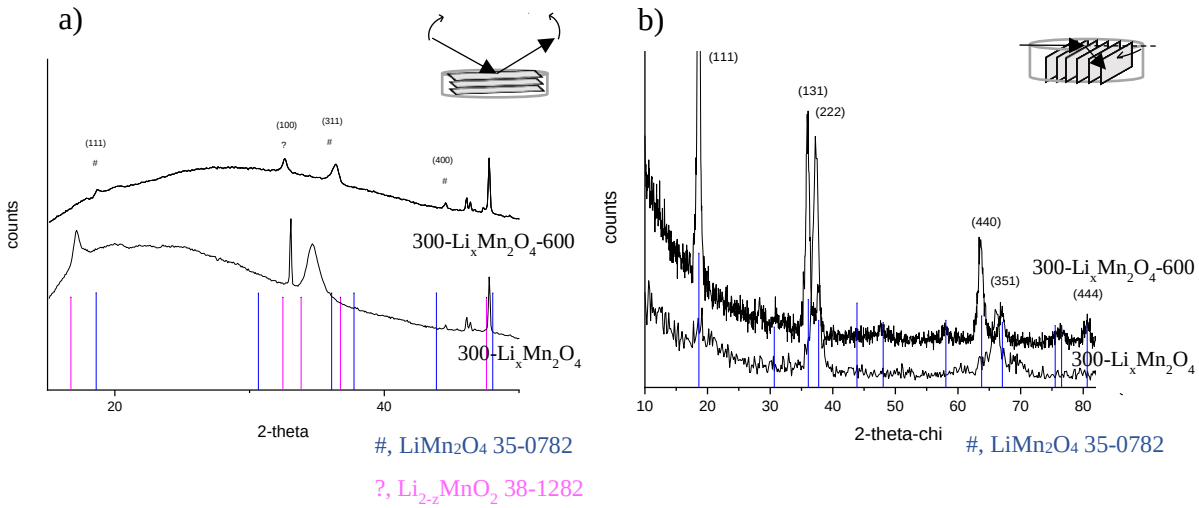

Figure 37. a) Out-of-plane 2θ diffractograms of 300-$Li_xMn_2O_4$ (lower line) and 300-$Li_xMn_2O_4$-600 (upper line). b) In-plane $2\theta_\chi$ diffractograms of 300-$Li_xMn_2O_4$ (lower line) and 300-$Li_xMn_2O_4$-600 (upper line).

The unit cell dimension for the spinel phase of 200-$Li_xMn_2O_4$-600 was a = 8.28 Å. The other visible phase β-MnO_2 had a unit cell parameter a = 4.3 Å which is in line with the reference pattern. No reflections other than (h00) were detected so the other unit cell parameters could not be determined.

The 300-$Li_xMn_2O_4$-600 is cubic spinel and the calculated unit cell parameter is a = 8.27 Å. The space group of the cubic spinel is Fd-3m. In the reference card 35-0782 the dimension of the cubic unit cell is a = 8.25 Å. The 300-$Li_xMn_2O_4$-600 is comparable to the powder reference. The calculated unit cells, stoichiometry and lithium distribution for both annealed samples are in Table 5.

Table 5. Stoichiometry, unit cell parameters and lithium distribution in the annealed samples. (The parameters are calculated using XRD data.)

Sample	Stoichiometry	Phase and Unit cell	Li distribution
200-$Li_xMn_2O_4$-600	$Li_{0.78}Mn_{2.08}O_4$	β-MnO_2 : a = 4.31 Å $LiMn_2O_4$: a = 8.28 Å	The whole film
300-$Li_xMn_2O_4$-600	$Li_{0.96}Mn_{1.84}O_4$	$LiMn_2O_4$: a = 8.27 Å	The whole film

9.4.5 Summary of the phase change from MnO_2 to $LiMn_2O_4$

The MnO_2 sample seems to be modified pyrolusite β-MnO_2. The residual stress causes the structure to be slightly orthorhombic instead of tetragonal. The sample has (*h*00) orientation in the out-of-plane direction.

After the lithium insertion the samples contain two lithium phases: lithium unstoichiometric $Li_{1-x}Mn_2O_4$ and stoichiometric $LiMn_2O_4$ cubic spinel. $Li_{1-x}Mn_2O_4$ shows strong (*h*00) orientation in the out-of-plane direction and is distributed only on the top part of the films. When the lithium concentration increases above $x \approx 0.5$, the pyrolusite β-MnO_2 changes to the spinel $Li_xMn_2O_4$ and lithium is able to intercalate throughout the whole film thickness. The (111) and (311) reflections of $LiMn_2O_4$ become dominant in the 200-$Li_xMn_2O_4$ and 300-$Li_xMn_2O_4$ samples. But it is not until the samples are annealed, when the phase seems to change completely to $LiMn_2O_4$. That is because the annealing enables lithium to overcome the diffusion energy barriers and to complete the pyrolusite/spinel phase change.

The interpretation of the XRD results is challenging since the films have high residual stresses which cause the peaks to shift compared to the reference cards. Especially the 300-$Li_xMn_2O_4$, which has over 2 GPa compressive residual stress, has large peak shifts in the diffractograms.

9.5 Local and electronic structure of the samples

9.5.1 Mn K-edge XANES

Figure 38 shows a total fluorescence yield (TFY) and a total electron yield (TEY) Mn K-edge XANES of all samples (a and b respectively). Both measurements show a shift of the absorption edge to lower energies, which indicates the reduction of manganese.

As is seen in Figure 38, the 10-$Li_xMn_2O_4$ and 50-$Li_xMn_2O_4$ samples resemble the MnO_2 reference. The first observation of the spinel $LiMn_2O_4$ is in the 100-$Li_xMn_2O_4$ curve. The spinel phase shows as a split of 3d to t_{2g} and e_g in the XAS pre-edge region. The peak split corresponding to the spinel phase is clear in the 200-$Li_xMn_2O_4$ curve as well. The results are in good agreement with XRD results.

The measured absorption edge positions are at lower energy compared to the spinel $LiMn_2O_4$ reference. The pre-edge peaks have also higher intensities than the reference. The higher intensity comes as a result of distortion of Jahn-Teller active Mn^{3+} ions. Both features indicate that the average oxidation state in these samples is lower than +3.5 and thus the films contain more Mn^{3+} than Mn^{4+} ions.[184]

The 300-$Li_xMn_2O_4$ sample has overall a different shape compared to the spinel $LiMn_2O_4$ reference. Its absorption edge has shifted to lower energy and the pre-edge shape is different compared to 100-$Li_xMn_2O_4$ and 200-$Li_xMn_2O_4$. This indicates that the environment around Mn is different in 300-$Li_xMn_2O_4$.

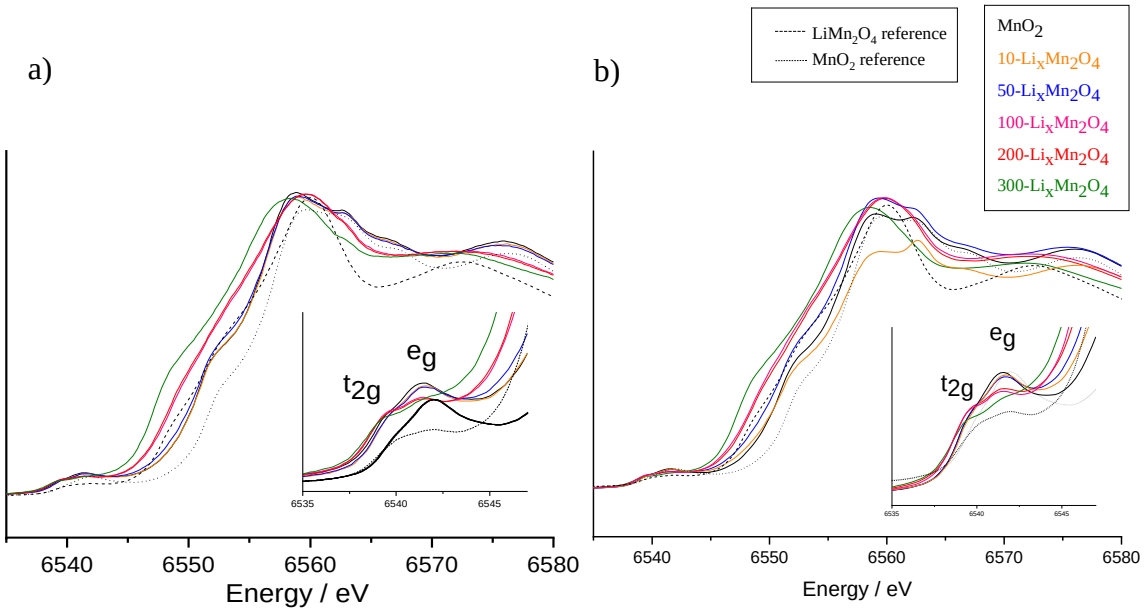

Figure 38. a) Total fluorescence yield of Mn K-edge XANES. b) Total electron yield Mn K-edge XANES and the $LiMn_2O_4$ and MnO_2 references.

The average oxidation state of manganese was determined by Settipani[184]. Comparison of several energy shifts of different absorption features was plotted against formal oxidation state of Mn. As a result, the half-height of the absorption edge had the best linear correlation to the oxidation state of Mn and it was used for determining the average oxidation state. The calculated average oxidation states of Mn are in Table 6.

The average oxidation state diminishes from around +3.6 to around +2.8 with increasing Li content and annealing (Figure 39). The oxidation state decreases through all the samples. The very low oxidation state of 300-$Li_xMn_2O_4$ and 300-$Li_xMn_2O_4$-600 could arise from some unexpected behavior related to 300-$Li_xMn_2O_4$, which was also noticed in the shape of the XAS spectrum.

As described earlier the total electron yield probes only a few nanometers on top of the thin film whereas the total fluorescence yield probes throughout the whole film. A comparison of the oxidation states measured by TFY and TEY (Figure 39) shows that the manganese oxidation states are similar, or at least within the measurement error, for both measurements. This was unexpected since in 10-$Li_xMn_2O_4$, 50-$Li_xMn_2O_4$ and 100-$Li_xMn_2O_4$ lithium is only on the surface of the film, according to the TOF-EDRA results. Hence it was expected that the oxidation state of manganese should be lower in the surface layer than in the bulk of the 10-$Li_xMn_2O_4$, 50-$Li_xMn_2O_4$ and 100-$Li_xMn_2O_4$ films.

Table 6. The average oxidation state of Mn determined from half-height of the absorption edge of Mn K-edge XANES.

Sample	Average oxidation state of Mn (standard deviation 0.05)	
	TFY	TEY
MnO_2	3,64	3,72
10-$Li_xMn_2O_4$	3,64	3,72
50-$Li_xMn_2O_4$	3,59	3,62
100-$Li_xMn_2O_4$	3,22	3,25
200-$Li_xMn_2O_4$	3,19	3,27
200-$Li_xMn_2O_4$-600	3,08	3,08
300-$Li_xMn_2O_4$	2,8	2,93
300-$Li_xMn_2O_4$-600	2,61	2,49

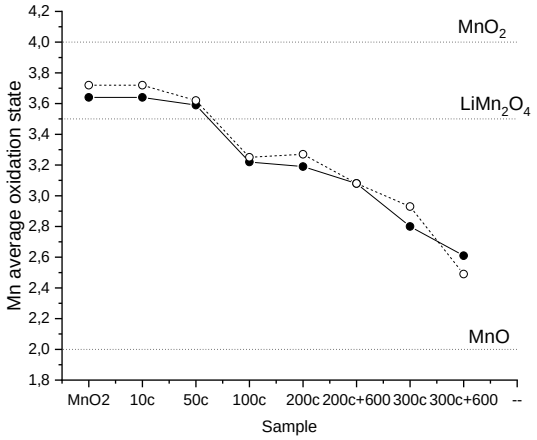

Figure 39. The average oxidation state of Mn determined from Mn K-edge XANES TFY (black dots) and TEY (white dots) measurements. The references MnO_2, $LiMn_2O_4$ and MnO are marked with a dotted line.

XANES spectra of the annealed samples are shown in Figure 40. 200-$Li_xMn_2O_4$-400 (not-shown) and 200-$Li_xMn_2O_4$-600 (Figure 40a) did not have major differences compared to the unannealed sample. The absorption edge has shifted to lower values, but the pre-edge region is similar for both samples. The 300-$Li_xMn_2O_4$-600 sample has a different pre-edge shape compared to the unannealed 300-$Li_xMn_2O_4$. The e_g resonance has diminished and the pre-edge region resembles more of the MnO reference.[184] The 300-$Li_xMn_2O_4$-600 sample had also a recognizable extra phase in the XRD. If the impurity phase was $Li_{2-z}MnO_2$ (as stated earlier), the oxidation state of Mn would be around +2, which would explain the similarity to the MnO reference.

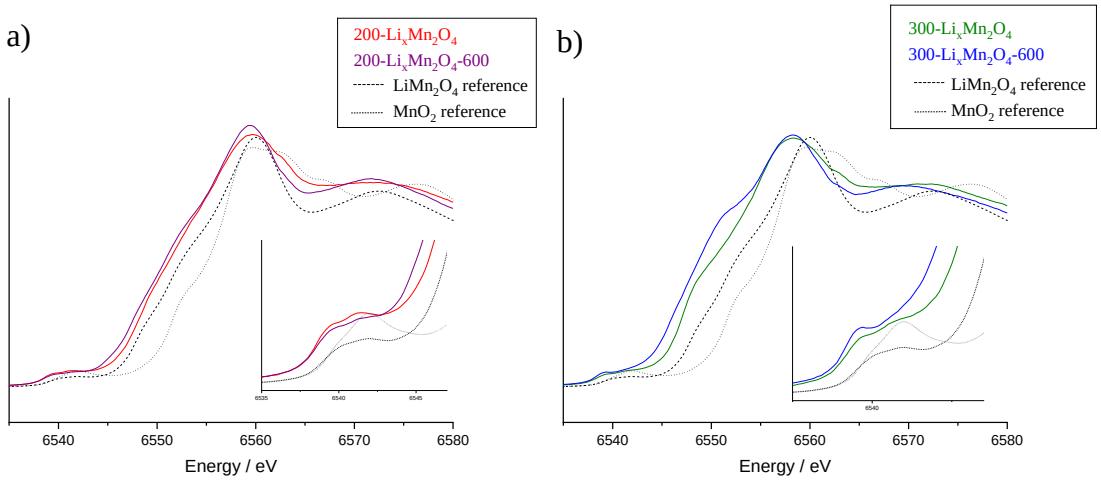

Figure 40. Mn K-edge XANES spectra of a) The 200-$Li_xMn_2O_4$ and 200-$Li_xMn_2O_4$-600 and b) The 300-$Li_xMn_2O_4$ and 300-$Li_xMn_2O_4$-600 with the $LiMn_2O_4$ and MnO_2 references.

9.5.2 Mn K-edge EXAFS

The bonds Mn – O, Mn – Mn1 and Mn – Mn2 are readily detected in Mn K-edge EXAFS of MnO_2 and $LiMn_2O_4$. The Mn – O distance means the bond between Mn and O and it is labeled with A in Figure 41a-c. The Mn – Mn1 distance means the shortest distance between two manganese atoms in the tetragonal pyrolusite structure, labeled with B. This distance is between the Mn atoms in the center of edge sharing octahedrons. The longer Mn – Mn2 distance C means the distance between the Mn atoms at the center of the corner sharing octahedrons. The longer distance does not exist in the cubic spinel structure.

Fourier transformed EXAFS data is shown in Figure 41a. The MnO_2, 10-$Li_xMn_2O_4$ and 50-$Li_xMn_2O_4$ samples have all three peaks A, B and C. By contrast, from 100-$Li_xMn_2O_4$ onward only peaks A and B are visible. XRD and Mn K-edge XANES results showed that the spinel

$LiMn_2O_4$ is the dominant phase in 100-$Li_xMn_2O_4$, 200-$Li_xMn_2O_4$ and 300-$Li_xMn_2O_4$, and the absence of the peak C in the EXAFS results support this conclusion.

The peaks A and B diminish when the number of lithium cycles is increased. This can happen due to increasing local distortion around manganese. The decrease of the A and B peaks is noticeable for 200-$Li_xMn_2O_4$ and 300-$Li_xMn_2O_4$.

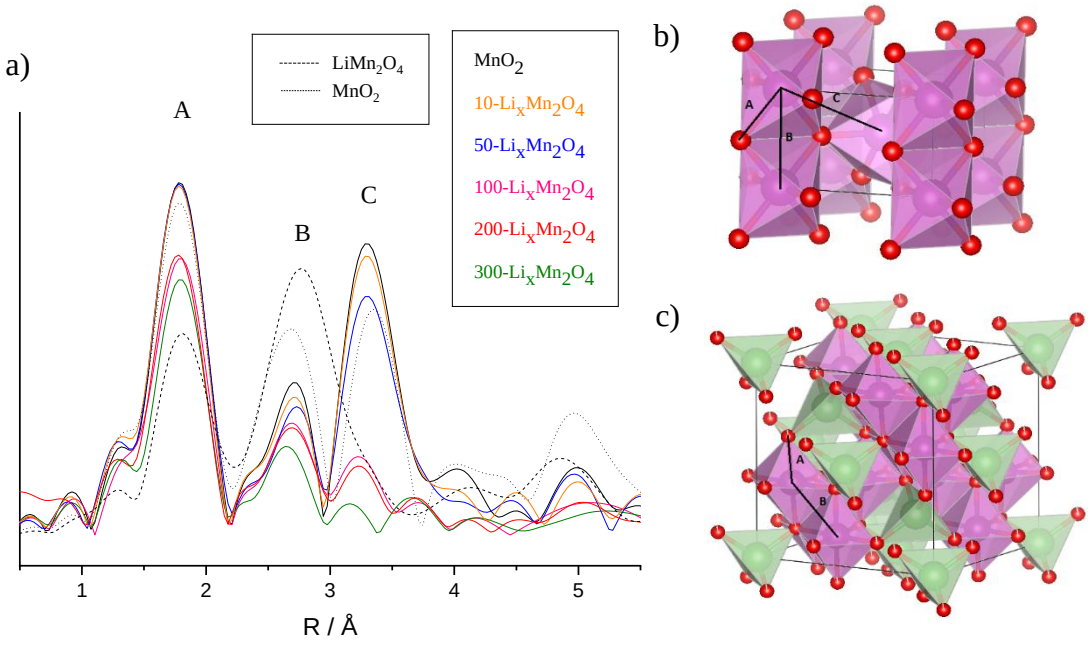

Figure 41. a) Fourier transformed Mn K-edge EXAFS data of all samples and the $LiMn_2O_4$ (dash line) and MnO_2 (dot line) references. b) The unit cell of MnO_2. c) The unit cell of $LiMn_2O_4$.

The B peak in 200-$Li_xMn_2O_4$-400 and 200-$Li_xMn_2O_4$-600 samples have higher intensity compared to the un-annealed 200-$Li_xMn_2O_4$ sample (Figure 42a). The EXAFS spectra of the annealed samples are also closer to the reference $LiMn_2O_4$. This indicates that the crystal structure is ordered better in the annealed samples than in the corresponding unannealed one.

300-$Li_xMn_2O_4$-600 has an additional resonance at around 3.5 Å (Figure 42b). The octahedrally coordinated Mn should not have this third resonance in the spinel $LiMn_2O_4$ structure. The additional resonance is again an indication of an unexpected local structure of the 300-$Li_xMn_2O_4$-600. The resonance could be a result of the $Li_{2-z}MnO_2$ phase, but to

confirm this assumption, more detailed analysis and reference measurements to EXAFS data is needed.

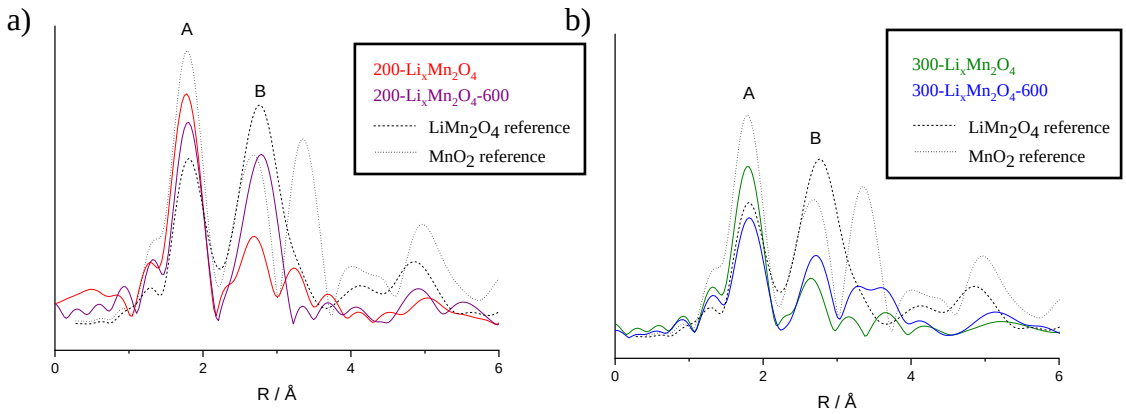

Figure 42. Fourier transformed Mn K-edge EXAFS data of a) 200-$Li_xMn_2O_4$ and 200-$Li_xMn_2O_4$-600 and b) 300-$Li_xMn_2O_4$ and 300-$Li_xMn_2O_4$-600 with the powder references.

Bond length calculations were made by Settipani[184]. The Mn-O bond length increased from 1,887 of MnO_2 to 1,913 of 300-$Li_xMn_2O_4$-600 (Table 7). The lengthening of the Mn-O bond can occur due to a reduction of Mn^{+4} to Mn^{+3}. The ionic radius of the cation increases and JT active Mn^{3+} can distort the structure and lengthen the Mn-O bond distance.

The average oxidation state of Mn was assessed also from the Mn-O bond distance determined from the EXAFS results. The increase in Mn-O bond length correlates to reduction of Mn. However, according to EXAFS analysis the average oxidation state decreases from about +4 to about +3.5, which is clearly different than the average oxidation state determined from the XANES data (from +3,6 to +2,8). The oxidation states determined by XANES are known to be prone to large errors. The average oxidation states got from EXAFS are closer to the theoretical oxidation states.

Table 7. The Mn-O bond distance and the average oxidation state of Mn determined from Mn K-edge EXAFS data.

Sample	Mn-O bond distance	Average oxidation state
MnO_2	1,887 ± 0.005	3.84 ± 0.03
10-$Li_xMn_2O_4$	1,881 ± 0.005	3.88 ± 0.03
50-$Li_xMn_2O_4$	1,881 ± 0.005	3.88 ± 0.03
100-$Li_xMn_2O_4$	1,888 ± 0.003	3.83 ± 0.02
200-$Li_xMn_2O_4$	1,886 ± 0.003	3.85 ± 0.02
200-$Li_xMn_2O_4$-600	1,908 ± 0.004	3.72 ± 0.02
300-$Li_xMn_2O_4$	1,887 ± 0.004	3.84 ± 0.03
300-$Li_xMn_2O_4$-600	1,913 ± 0.005	3.69 ± 003

9.5.3 Mn L-edge XANES

Mn L-edge as well as O K-edge XANES were measured with 0.5°, 1°, 5° and 45° incident angles. Penetration depth of the x-ray is dependent on the incident angle of the x-ray beam. The measurement made with the 45° incident angle probes the whole film, whereas the measurements made with 0.5° and 1° incident angles are highly surface sensitive. The measurement done with the 5° incident angle probes a few nanometers from the surface of the film.

In the Mn L-edge XANES spectrum the first peak in L_{III} region comes as a result of Mn^{3+} and the second peak from Mn^{4+} (Figure 43a). In the earlier XAS measurements on $LiMn_2O_4$ mostly Mn^{4+} was found.[151] The samples as well as the MnO_2, Mn_2O_3 and $LiMn_2O_4$ reference powders measured here had however different fine structures compared to the results in literature. That is why now the focus is on comparing the measured curves to each other and to references rather than to the literature.

The Mn L-edge XANES spectra show moderate changes when the samples are compared to each other. Figure 43a is a comparison of the bulk films i.e. L-edge spectra measured with the 45° angle. The 300-$Li_xMn_2O_4$ is the first sample that has some indication of Mn^{3+} ions being present. The annealing seems to erase the Mn^{3+} contribution since the 300-$Li_xMn_2O_4$-600 does not have Mn^{3+} features.

Figures 43 b-d show the Mn L-edge of the samples compared to different linear combinations of Mn^{3+} and Mn^{4+} references. The measurements have been made with the 45° incident angle, since it probes the whole film and hence gets least influenced by possible contaminants on the surface. The aim was to find out in what relation Mn^{4+} and Mn^{3+} were in the samples i.e. how much the manganese had reduced. The MnO_2 sample resembles the Mn^{4+} reference, as expected (Figure 43b). The 100-$Li_xMn_2O_4$, 50-$Li_xMn_2O_4$ and 10-$Li_xMn_2O_4$ did not show any indications of Mn^{3+} and the curves looked more like the Mn^{4+} reference (Figure 43c). The 300-$Li_xMn_2O_4$ resembles mostly the reference where the relation of Mn^{4+}/Mn^{3+} is 60% / 40%. Hence the bulk of the film has both manganese oxidation states present. The result fits well to the hypothesis that the average Mn oxidation state is +3.5. The 200-$Li_xMn_2O_4$ resembled the reference with the Mn^{4+}/Mn^{3+} relation of 80% / 20% (dash dot line in Figure 43d).

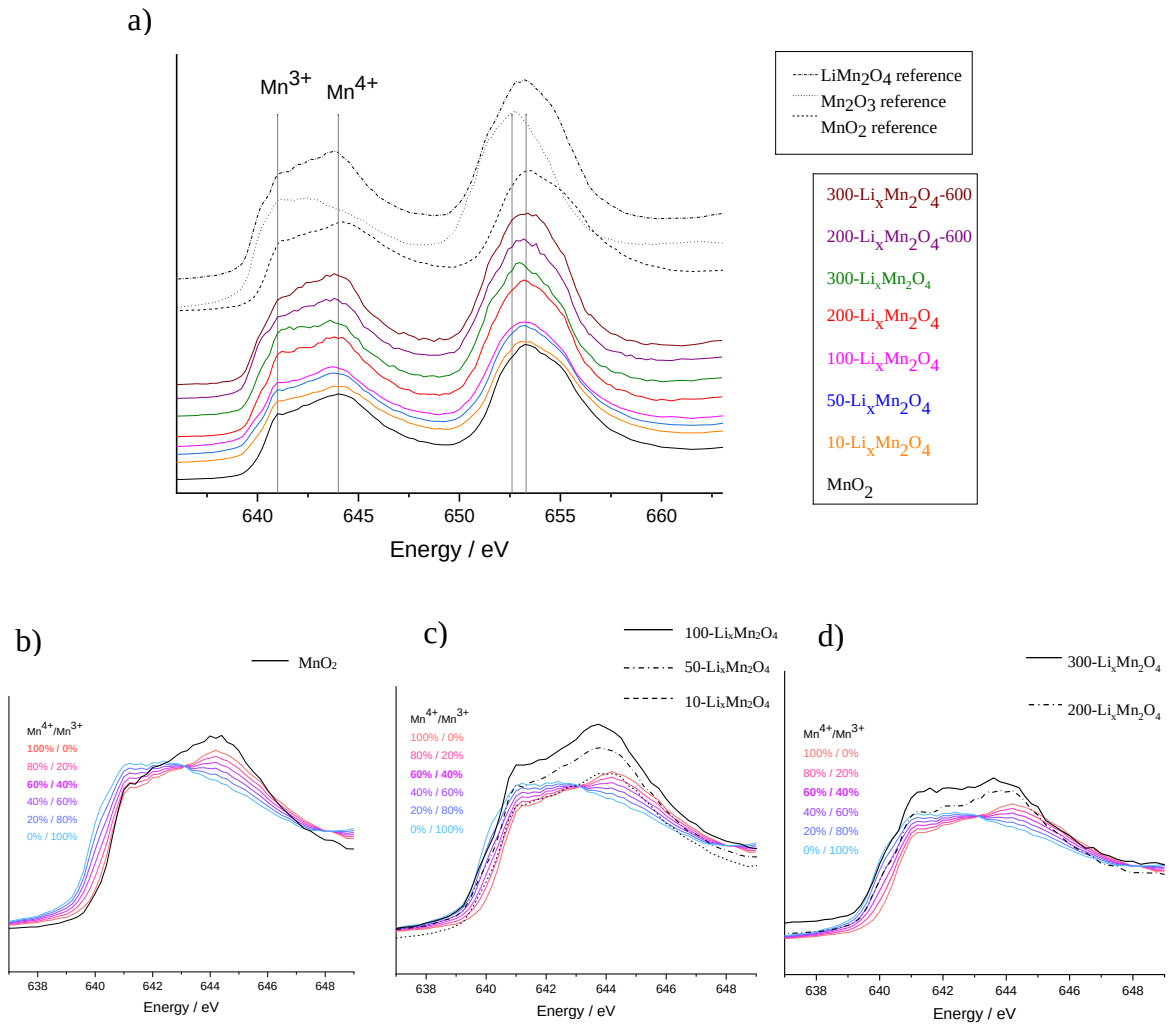

Figure 43. Mn L-edge measured at 45° incident angle. a) A comparison of all the samples and the powder references. b-d) A comparison of the samples to a set of linear combinations of Mn^{4+} and Mn^{3+} references.

Every sample shows minor Mn^{3+} features on the surface of the film. The measurements done with the 0.5° and 1° incident angles are shown in Figures 44 a and b. Even the MnO_2 film has the Mn^{3+} feature, so the appearance of Mn^{3+} can be due to some kind of surface contamination or oxygen vacancies that result in a reduced octahedral symmetry of oxygen atoms at the surface.[190] The measurement done with the 5° incident angle probes approximately 25 nm deep and it shows already the Mn^{4+} features (Figure 44c).

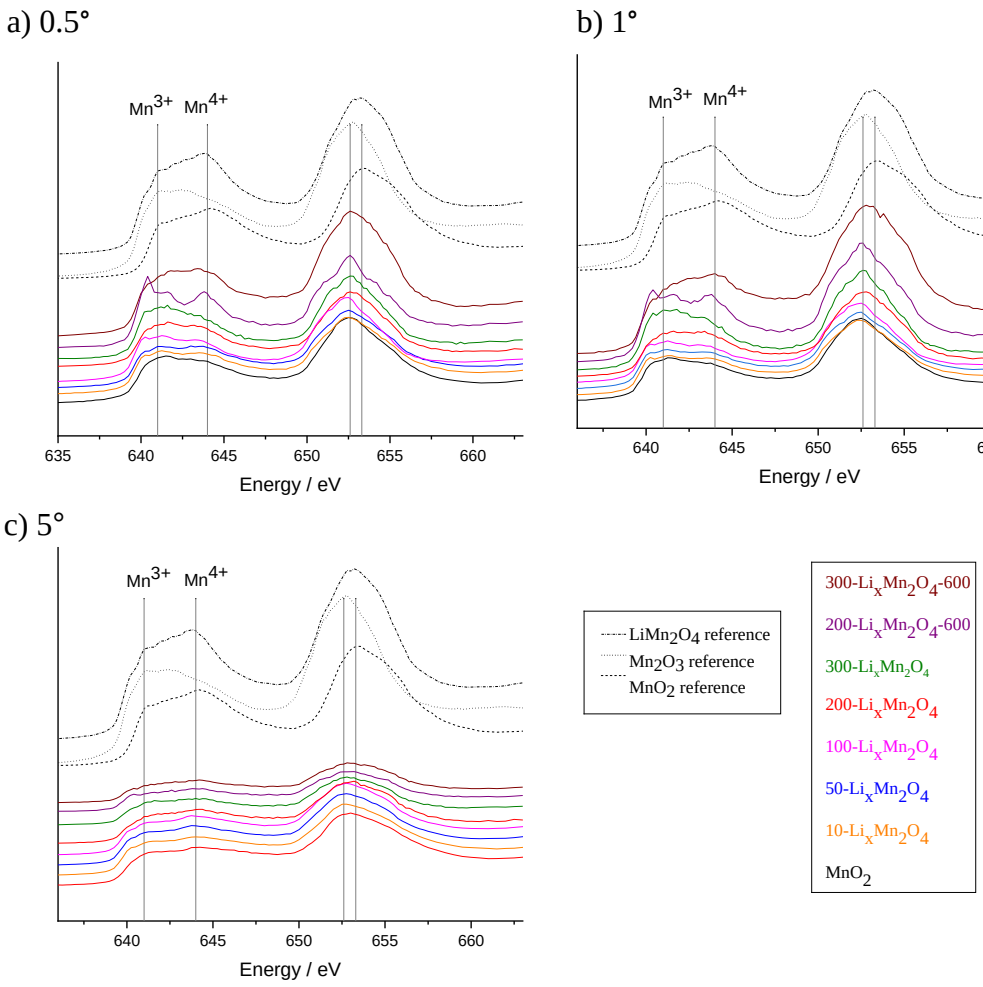

Figure 44. Comparison of Mn L-edge XANES spectra of every sample and the references. Measurements were done at a) 0.5° b) 1° and c) 5° incident angles.

9.5.4 O K-edge XANES

Oxygen K-edge XANES was measured with different incident angles for MnO_2, 200-$Li_xMn_2O_4$, 300-$Li_xMn_2O_4$, 200-$Li_xMn_2O_4$-600 and 300-$Li_xMn_2O_4$-600. The measurements were done with 0.5°, 1°, 5° and 45° incident angles.

The first peaks A and B correspond to the transition from the oxygen 1s orbital to the hybridized orbital between oxygen 2p and manganese 3d. Depending on the occupation of the 3d orbital of Mn, an additional third sharp peak may appear. If the curve has two clear

peaks A and B, the neighboring Mn of oxygen appears on +4 oxidation state. If the additional third peak is seen, the neighboring Mn appears on +3 oxidation state.

All the O K-edges indicate Mn^{4+} in the film bulk (Figure 45a). The 200-$Li_xMn_2O_4$ and 300-$Li_xMn_2O_4$ have some remarks of Mn^{3+} as well, however the annealing removes these features. Both the annealed samples are similar to the $LiMn_2O_4$ reference in the film bulk.

Surfaces of the films seem to have contributions of Mn^{3+} (Figures 45c and d). The absorption edge shifts to higher energy and the fine structure of the K-edge has some features of the Mn^{3+} reference. These features diminish the same way as in the 45° measurement when the samples are annealed.

The 300-$Li_xMn_2O_4$ film has an additional resonance at around 532 eV. According to the peak shape the manganese and oxygen atoms do not form an octahedron. The sample may have contamination, for example carbon bonded oxygen changes the fine structure to look like that of the 300-$Li_xMn_2O_4$ surface.[191]

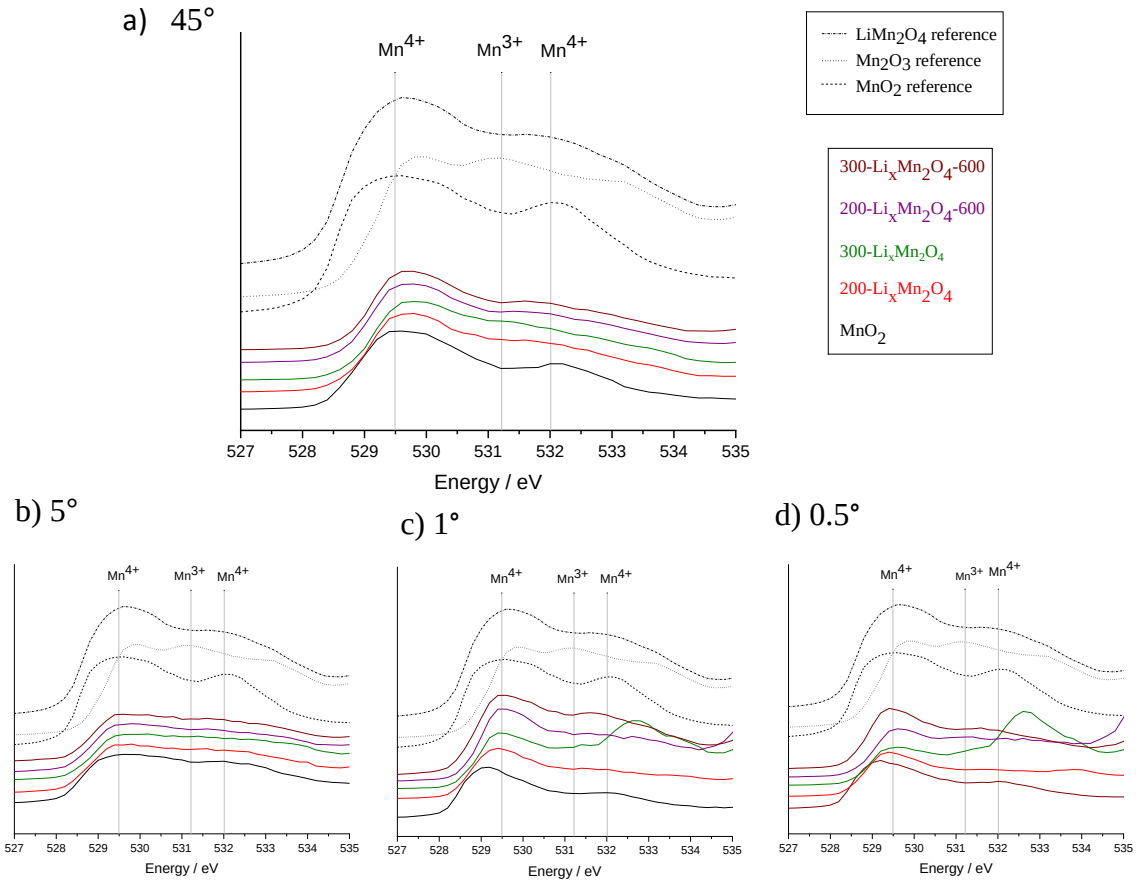

Figure 45. Oxygen K-edge XANES spectra for MnO_2, 200-$Li_xMn_2O_4$, 300-$Li_xMn_2O_4$, 200-$Li_xMn_2O_4$-600 and 300-$Li_xMn_2O_4$-600 measured with a) 45°, b) 5°, c) 1° and d) 0.5° incident angles.

9.5.5 X-ray photoelectron spectroscopy

The oxidation state of manganese on the surface of the MnO_2 film was measured with XPS. High-resolution Mn 3s spectra of a MnO_2 film with the powder MnO and Mn_2O_3 references are in Figure 46a. The peak fitting of the Mn 2p, O 1s, C 1s and Mn 3s are in the Figure 46b.

The shape of the Mn 2p peak indicates that manganese occurs at +II, +III and +IV oxidation states, but mostly on the +III state. XPS is a highly surface sensitive technique and hence the result is in line with the Mn L-edge XANES. The samples may have some contamination or oxygen vacancies, which causes the reduction of manganese. The spectral shape of the C 1s peak resembles a typical surface contaminated carbon.

a)

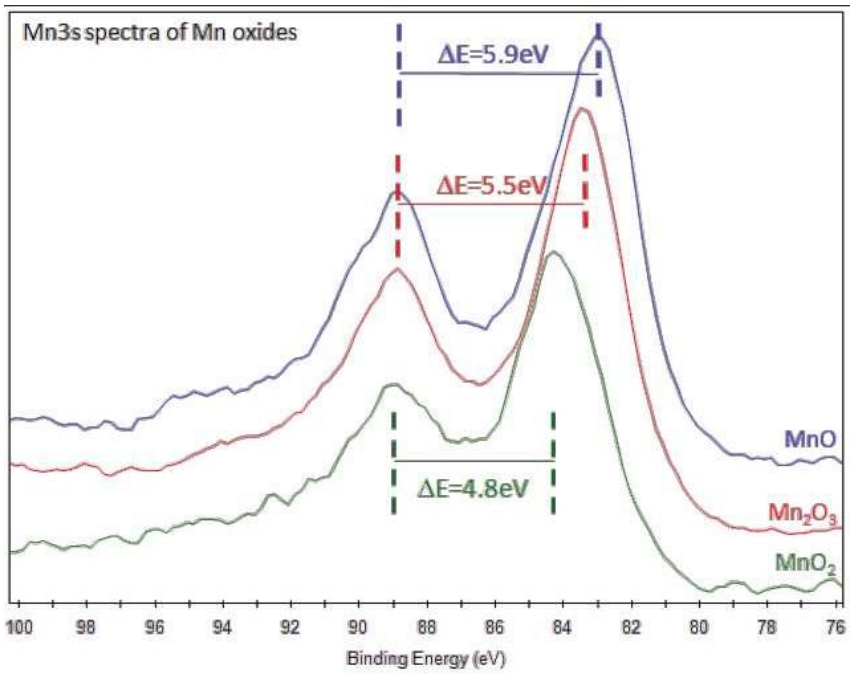

b)

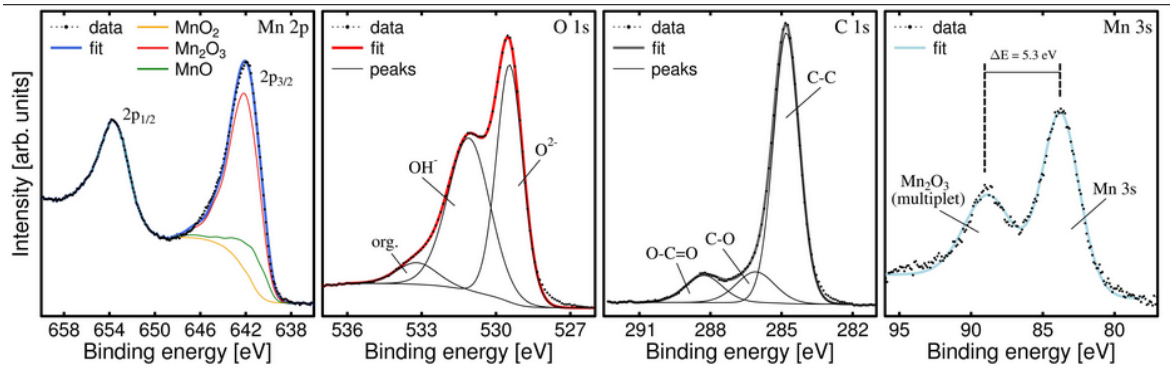

Figure 46. a) High resolution spectra of MnO_2 film and the MnO and Mn_2O_3 powder references. b) Peak fitting of (from left to right) Mn 2p, O 1s, C 1s and Mn 3s in the XPS spectrum of the MnO_2 film.

10 Conclusions

The films were deposited by ALD in two steps: first the MnO_2 films were deposited starting from $Mn(thd)_3$ and O_3 and second lithium was intercalated by pulsing LiO^tBu and H_2O on top of the MnO_2 film. The phase change and lithium intercalation were studied by preparing a set of samples with increasing lithium concentration from $Li_{0.014}MnO_2$ to $Li_{1.06}Mn_2O_4$. The conversion was studied with XRD, TOF-ERDA, EXAFS and XANES to get clearer vision of the electronic and structural changes taking place when lithium intercalates. Residual

stress measurements were done to get complementary information. XPS of MnO_2 was measured also for supporting information.

According to literature, as soon as lithium intercalates into the structure, it reduces Mn^{4+} ions to Mn^{3+}. The first intercalation site of lithium is sharing edges of oxygen octahedron with the Mn^{3+} ions. This intercalation site causes strong repulsive force and pushes the cations to the cubic close packed structure and the lithium into 8a interstitial sites, where it is tetragonally coordinated. This oxygen tetrahedron around Li^+ ion is only sharing corners with oxygen octahedron around Mn^{3+} ions and is hence more favorable structure energetically. The β-MnO_2 changes therefore to the spinel [Mn_2O_4] framework already at low lithium concentrations.

The present results indicated that the phase change seems to take place via two spinel lithium manganese oxide phases: $Li_{1-x}Mn_2O_4$ and $LiMn_2O_4$. When the lithium insertion began, i.e. in samples 10-$Li_xMn_2O_4$ and 50-$Li_xMn_2O_4$, strongly (*h*00) oriented $Li_{1-x}Mn_2O_4$ phase appeared. TOF-ERDA showed that in this state lithium had distributed only on the top part of the films. The EXAFS of Mn K-edge showed still all three bonds Mn-O, Mn-Mn1 and Mn-Mn2 that are characteristic for β-MnO_2.

When the lithium insertion proceeded, and the stoichiometry exceeded x = 0.5, the (111) and (311) peaks from the spinel $LiMn_2O_4$ appeared in the out-of-plane XRD and the stoichiometric $LiMn_2O_4$ became more significant than the $Li_{1-x}Mn_2O_4$ phase. The Mn K-edge EXAFS showed only the Mn-O and Mn-Mn1 bonds, which are related to the spinel $LiMn_2O_4$. TOF-ERDA depth profiles revealed that the lithium had distributed throughout the whole film thickness. The samples showed both lithium manganese oxide phases until they were annealed. After the annealing the samples were phase pure $LiMn_2O_4$ according to XRD.

The Mn K absorption edge shifted to higher energy as soon as lithium was inserted. This indicates immediate reduction of Mn^{4+} to Mn^{3+}. The fine structure of the Mn K-edge XANES resembled that of the MnO_2 at the beginning of the lithium insertion (in samples 10-$Li_xMn_2O_4$ and 50-$Li_xMn_2O_4$). In agreement with XRD, features from $LiMn_2O_4$ started to appear in the fine structure when the lithium insertion continued (in the samples 100-$Li_xMn_2O_4$ and onward).

The average oxidation state of manganese determined from the Mn K-edge XANES decreased from already low +3.6 to +2.8 when lithium was inserted into the MnO_2 film. The oxidation state determined from the EXAFS data of the same edge showed a decrease from about +4 to +3.5. The fine structure of the Mn L-edge showed mostly Mn^{4+} features in the bulk of the film. The O K-edge did not have significant features from Mn^{3+} either. Hence as a conclusion of this study the average oxidation state of manganese is reducing when lithium is inserted and the oxidation state is assumed to be in between +3.5 and +4 in all samples in the bulk of the films.

The XAS measurements revealed possibility of some Mn^{3+} on the surface of the films. Mn^{3+} was found also on the surface of MnO_2 in the XPS studies. This could be a result of oxygen vacancies at the surface of the film or a sign of some surface contamination. The features of Mn^{3+} disappeared when the samples were annealed.

$LiMn_2O_4$ is a potential cathode material for a lithium ion battery. It has however rather complex lithium exchange mechanism. It is noted that the manganese oxide framework can balance the lithium insertion/extraction by utilizing the many oxidation states of manganese or the ability to develop vacancies and the possibility to exploit oxygen for the charge compensation. Despite the challenges concerning the subject, the details of the lithium exchange are crucial for understanding the working principle of LIBs.

References

1. Miikkulainen V., Leskelä M., Ritala M. and Puurunen RL. *J Appl Phys*. **113** (2013) 2 021301

2. Johnson RW., Hultqvist A., and Bent SF. *Mater. Today* **17 (**2014) 5 236 doi:

3. Balbuena PB. and Wang Y. *Lithium-ion batteries: Solid-electrolyte interface* Imperial College Press, 2004.

4. Yoshino A. in *Lithium-ion batteries*, ed. Pistoia G., Elsevier, Amsterdam, 2014, chapter 1, pages 1-20.

5. Bhatt MD. and O'Dwyer C. *Phys. Chem. Chem. Phys*. 1**7** (2015) 4799.

6. Sun C., Liu J., Gong Y., Wilkinson DP. and Zhang J. *Nano Energy* **33** (2017) 363.

7. Kanno R., Takeda Y., Ichikawa T., Nakanishi K. and Yamamoto O. *J. Power Sources* **26** (1989) 3 535.

8. Mohri M., Yanagisawa N., Tajima Y., Tanaka H., Mitate T., Nakajima S., Yoshida M., Yoshimoto Y., Suzuki T. and Wada H. *J. Power Sources*. **26** (1989) 3 545.

9. Tarascon JM., and Guyomard D. *Electrochim. Acta* **38** (1993) 9 1221.

10. Daniel C. and Besenhard JO. *Handbook of battery materials* John Wiley & Sons 2008.

11. Haghi AK., Zachariah AK. and Kalarikkal N. *Nanomaterials: Synthesis, characterization, and applications,* Apple Academic Press Inc., Canada, 2013.

12. Paulsen JM. and Dahn JR. *Chem Mater*. **11** (1999) 11 3065.

13. Thackeray MM. *Prog. Solid State Chem*. **25** (1997) 1 1.

14. Gummow RJ., de Kock A. and Thackeray MM. *Solid State Ionics* **69** (1994) 1 59.

15. Hunter JC. *J. Solid State Chem*. **39** (1981) 2 142.

16. Devaraj S. and Munichandraiah N. *J. Phys. Chem. C* **112** (2008) 11 4406.

17. Liu Y., Wei J., Tian Y. and Yan S. *J. Mater. Chem. A* **3** (2015) 37 19000.

18. David WIF., Thackeray MM., Bruce PG. and Goodenough JB. *Mater. Res. Bull*. **19** (1984) 1 99.

19. Davoglio RA., Irikura K., Biaggio SR., Bocchi N. and Rocha-Filho RC. *J. Solid State Electrochem*. **20** (2016) 7 2019.

20. Ouyang CY., Shi SQ. and Lei MS. *J Alloys Compd*. **474** (2009) 1–2 370.

21. Yamada A. and Tanaka M. *Mater. Res. Bull*. **30** (1995) 6 715.

22. Tomeno I., Kasuya Y. and Tsudona Y. *Phys. Rev. B: Condens. Matter* **64** (2001) 094422.

23. Wills AS., Raju NP., Greedan JE. *Chem. Mater*. **11** (1999) 6 1510.

24. Rodríguez-Carvajal J., Gwenaëlle R. and Masquelier C. *Phys. Rev. Lett*. **81** (1998) 21 4660.

25. Masquelier C., Tabuchi M., Ado K., Kanno R., Kobayashi Y., Maki Y., Nakamura O. and Goodenough JB. *J. Solid State Chem*. **123** (1996) 2 255.

26. Takada T., Hayakawa H., Enoki H., Akiba E., Slegr H., Davidson I. and Murray J. *J. Power Sources*. **81-82** (1999) 505.

27. Rousse G., Masquelier C., Rodriguez-Carvajal J., Elkaim E., Lauriat JP. and Martinez JL. *Chem. Mater*. **11** (1999) 12 3629.

28. Oikawa K., Kamiyama T., Izumi F., Chakoumakos BC., Ikuta H., Wakihara M., Li J. and Matsui Y. *Solid State Ionics*. **109** (1998) 1–2 35.

29. Sun Y., Jeon Y. and Leeb HJ. *Electrochem. Solid-State Lett*. **3** (2000) 1 7.

30. Li X., Xu Y. and Wang C. *J Alloys Compd*. **479** (2009) 1–2 310.

31. Liu Q., Yu L., and Wang H. *J. Alloys Compd*. **486** (2009) 1 886.

32. Hashem AMA. *Ionics*. **10** (2004) 3 206.

33. Wang GG., Wang JM., Mao WQ., Shao HB., Zhang JQ. and Cao CN. *J. Solid State Electrochem*. **9** (2005) 7 524.

34. Wei Y., Kim KB., Chen G. and Park CW. *Mater Charact*. **59** (2008) 9 1196.

35. Ju SH., Kim DY., Jo EB. and Kang YC. *J. Ceram. Soc. Jpn*. **115** (2007) 241 1340.

36. Geng S., Geng S. and Zhai Y. *Mater. Manuf. Processes* **32** (2017) 16 1856.

37. Li S., Lei D., Xue Y., Geng S. and Cui X. *Ionics*. **23** (2017) 8 1979.

38. Jeong WT., Joo JH. and Lee KS. *J. Alloys Compd*. **358** (2003) 1 294.

39. Choi HJ., Lee KM., Kim GH. and Lee JG. *J. Am. Ceram. Soc*. **84** (2004) 1 242.

40. Fadzil AFM., Bustam MA., Aziz NDA., Yahya NF. and Zainol NH. Conference paper in *AIP Conference Proceedings*. **1877** (2017) 1 040006.

41. Wu XM., Li XH., Xiao ZB., Liu J., Yan WB. and Ma MY. *Mater. Chem. Phys*. **84** (2004) 1 182.

42. Hon YM., Lin SP., Fung KZ. and Hon MH. *J. Eur. Ceram. Soc*. **22** (2002) 5 653.

43. Hon YM., Fung KZ. and Hon MH. *J. Eur. Ceram. Soc*. **21** (2001) 4 515.

44. Lee Y., Sun Y. and Nahm K. *Solid State Ionics*. **109** (1998) 3 285.

45. Sun YK., Oh IH. and Kim KY. *Ind. Eng. Chem. Res*. **36** (1997) 11 4839.

46. Prabaharan SRS., Michael MS., Kumar TP., Mani A., Athinarayanaswamy K. and Gangadharan R. *J. Mater. Chem*. **5** (1995) 7 1035.

47. Li X., Xiang R., Su T. and Qian Y. *Mater. Lett*. **61** (2007) 17 3597.

48. Wang X., Chen X., Gao L., Zheng H., Ji M., Shen T. and Zhang Z. *J. Cryst. Growth* **256** (2003) 1 123.

49. Wan C., Nuli Y., Wu Q., Yan M. and Jiang Z. *J. Appl. Electrochem*. **33** (2003) 1 107.

50. Vivekanandhan S., Venkateswarlu M. and Satyanarayana N. *J. Alloys Compd*. **441** (2007) 1 284.

51. Lu C. and Saha SK. *J. Sol-Gel Sc. Technol*. **20** (2001) 1 27.

52. Hwang K., Um W., Lee H., Song J. and Chung K. *J. Power Sources*. **74** (1998) 2 169.

53. Putra TYSP., Yonemura M., Torii S., Ishigaki T. and Kamiyama T. *Solid State Ionics* **262** (2014) 83.

54. Vivekanandhan S., Venkateswarlu M., Satyanarayana N., Suresh P., Nagaraju DH. and Munichandraiah N. *Mater. Lett*. **60** (2006) 27 3212.

55. He B., Zhou W., Bao S., Liang Y. and Li H. *Electrochim. Acta* **52** (2007) 9 3286.

56. Noerochim L., Sapputra G., Panca A. and Widodo A. Conference paper in *AIP Conference Proceedings*. **1725** (2016) 1 020054.

57. Fu Y., Lin C., Su Y., Jean J. and Wu S. *Ceram. Int*. **30** (2004) 7 1953.

58. Yao J., Lv L., Shen C., Zhang P., Aguey-Zinsou K. and Wang L. *Ceram. Int*. **39** (2013) 3 3359.

59. Wu HM., Tu JP., Yuan YF., Chen XT., Xiang JY., Zhao XB. and Cao GS. *J. Power Sources*. **161** (2006) 2 1260.

60. Izumi T., Keigo M., Hiroki F. and Shinya N. *AIChE J*. **52** (2006) 7 2413.

61. Taniguchi I., Lim CK., Song D. and Wakihara M. *Solid State Ionics*. **146** (2002) 3 239.

62. Zhang X., Zheng H., Battaglia V. and Axelbaum RL. *J. Power Sources* **196** (2011) 7 3640.

63. Hirose S., Kodera T. and Ogihara T. *J. Alloys Compd*. **506** (2010) 2 883.

64. Yi JH., Kim JH., Koo HY., Ko YN., Kang YC. and Lee J. *J. Power Sources* **196** (2011) 5 2858.

65. Helan M. and Berchmans LJ. *Mater. Manuf. Processes* **26** (2011) 11 1369.

66. Helan M., Berchmans LJ., Jose TP., Visuvasam A. and Angappan S. *Mater. Chem. Phys*. **124** (2010) 1 439.

67. Koao LF., Motloung SV., Motaung TE. and Kebede MA. *Physica B: Condensed Matter*. **535** (2018) 323.

68. Widiatmoko P., Khaemba DN. and Lenggoro W. *J. Ceram. Soc. Jpn*. **122** (2014) 12 976.

69. Zhu C., Nobuta A., Saito G., Nakatsugawa I. and Akiyama T. *Adv. Powder Technol*. **25** (2014) 1 342.

70. Park H., Kim J. and Lee C. *J. Power Sources*. **92** (2001) 1 124.

71. Zhou X., Chen M., Bai H., Su C., Feng L. and Guo J. *Vacuum*. **99** (2014) 49.

72. Park JP., Kim SK., Park J., Hwang CH., Choi N., Kim JE., Ok KM., Kwak HY. and Shim IW. *Mater. Lett*. **63** (2009) 26 2201.

73. Hwang B., Kim S., Lee Y., Park H., Kim D. and Park K. *Mater. Chem. Phys*. **158** (2015) 138.

74. Roeder M., Beleke AB., Guntow U., Buensow J., Guerfi A., Posset U., Lorrmann H., Zaghib K. and Sextl G. *J. Power Sources* **301** (2016) 35.

75. Park BG., Kim S., Kim I. and Park YJ. *J. Mater. Sci*. **45** (2010) 14 3947.

76. Liang H., Zhao X., Yu Z., Cao M. and Liu H. *Solid State Ionics*. **192** (2011) 1 339.

77. Matsuo Y., Sugie Y., Sakamoto K. and Fukutsuka T. *J. Solid State Electrochem*. **15** (2011) 3 503.

78. Shih F. and Fung K. *J. Power Sources* **159** (2006) 1 179.

79. Ma M., Xiao Z., Li X., Wu X., He Z. and Chen S. *Trans. Nonferrous Met. Soc. China* **16** (2006) 3 545.

80. Shih F., Fung K. and Wang J. *J. Alloys Compd*. **407** (2006) 1 282.

81. Tsumura T., Shimizu A. and Inagaki M. *J. Mater. Chem*. **3** (1993) 9 995.

82. Quan Z., Ohguchi S., Kawase M., Tanimura H. and Sonoyama N. *J. Power Sources* **244** (2013) 375.

83. Karthick SN., Prabhu R., Gnanakan S., Subramania A. and Kim H. *J. Alloys Compd*. **489** (2010) 2 674.

84. Subramania A., Karthick SN. and Angayarkanni N. *Thin Solid Films* **516** (2008) 23 8295.

85. Chiu K. and Chen C. *Thin Solid Films* **519** (2011) 15 4705.

86. Chen CC., Chiu K., Lin KM. and Lin HC. *Thin Solid Films* **517** (2009) 14 4192.

87. Chen CC., Chiu KF., Lin KM., Lin HC., Yang CR. and Wang FM. *Phys Scr*. **T129** (2007).

88. Fischer J., Adelhelm C., Bergfeldt T., Chang K., Ziebert C., Leiste H., Stüber M., Ulrich S., Music D., Hallstedt B. and Seifert HJ. *Thin Solid Films* **528** (2013) 217.

89. Hwang BJ., Wang CY., Cheng MY. and Santhanam R. *J. Phys. Chem. C* **113** (2009) 26 11373.

90. Proell J., Kohler R., Mangang A., Ulrich S., Ziebert C. and Pfleging W. *J. laser micro/nanoengineering* **7** (2012).

91. Babu KJ., Kumar PJ. and Hussain OM. *Appl. Nanosci*. **2** (2012) 4 401.

92. Put B., Vereecken PM., Labyedh N., Sepulveda A., Huyghebaert C., Radu IP., Stesmans A. *ACS Appl. Mater. Interfaces* **7** (2014) 40 22413.

93. Tang SB., Lai MO., Lu L. *Philos. Mag*. **87** (2007) 22 3249.

94. Tang SB., Lai MO., Lu L. and Tripathy S. *J. Solid State Chem*. **209** (2006) 12 3831

95. Dumont T., Lippert T., Döbeli M., Grimmer H., Ufheil J., Novak P., Würsig A, Vogt U. and Wokaun A. *Appl. Surf. Sci*. **252** (2006) 13 4902.

96. Julien C., Haro-Poniatowski E., Camacho-Lopez MA., Escobar-Alarcon L. and Jimenez-Jarquin J. *Mater. Sci. Eng., B* **72** (2000) 1 36.

97. Inaba M., Doi T., Iriyama Y., Abe T. and Ogumi Z. *J. Power Sources*. **81-81** (1999) 554.

98. Xie J., Kohno K., Matsumura T., Imanishi N., Hirano A., Takeda Y. and Yamamoto O. *Electrochim. Acta* **54** (2008) 2 376.

99. Matsumura T., Imanishi N., Hirano A., Sonoyama N. and Takeda Y. *Solid State Ionics* **179** (2008) 35 2011.

100. Tang SB., Xia H., Lai MO. and Lu L. *J. Alloys Compd*. **449** (2008) 1 322.

101. Tang SB., Lai MO. and Lu L. *Mater. Chem. Phys*. **111** (2008) 1 149.

102. Ouyang C., Deng H., Ye Z., Lei M. and Chen L. *Thin Solid Films* **503** (2006) 1 268.

103. Hirayama M., Hedekazu I., Kim KS., Cho W., Tamura K., Mizuki J. and Kanno R. *J. Am. Chem. Soc*. **132** (2010) 43 15268.

104. Tang SB., Lai MO. and Lu L. *J. Power Sources*. **164** (2007) 1 372.

105. Fehse M., Trócoli R., Hernández E., Ventosa E., Sepulveda A., Morata A., Tarancon A. *Thin Solid Films* **648** (2018) 108.

106. Fragnaud P., Nagarajan R., Schleich DM. and Vujic D. *J. Power Sources* **54** (1995) 2 362.

107. Tadanaga K., Yamaguchi A., Sakuda A., Hayashi A., Tatsumisago M., Duran A. and Aparacio M. *Mater. Res. Bull*. **53** (2014) 196.

108. Miikkulainen V., Ruud A., Østreng E., Nilsen O., Laitinen M., Sajavaara T. and Fjellvåg H. *J. Phys. Chem. C* **118** (2014) 2 1258.

109. Young MJ., Schnabel H., Holder AM., George SM. and Musgrave CB. *Adv. Funct. Mater*. **26** (2016) 43 7895.

110. Nilsen O., Fjellvåg H. and Kjekshus A. *Thin Solid Films* **444** (2003) 1 44.

111. Li YW., Qiao Q., Zhang JZ., Hu ZG. and Chu JH. *Thin Solid Films* **574** (2015) 115.

112. Mattelaer F., Vereechen PM., Dendooven J., Detavernier C. *Chem. Mater*. **27** (2015) 10 3628.

113. Foss S., Nilsen O., Olsen A. and Taftø J. *Philos. Mag*. **85** (2005) 23 2689.

114. Nilsen O., Foss S., Fjellvåg H. and Kjekshus A. *Thin Solid Films* **468** (2004) 1 65.

115. Jin H., Hagen D. and Karppinen M. *Dalton Trans*. **45** (2016) 46 18737.

116. Burton BB., Fabreguette FH. and George SM. *Thin Solid Films* **517** (2009) 19 5658.

117. Young MJ., Hare CD., Cavanagh AS., Musgrave CB. and George SM. *ACS Appl. Mater. Interfaces* **8** (2016) 28 18560.

118. Sun Y., Xu C., Li B., Xu J., He YB., Du H. and Kang F. *Int. J. Electrochem. Sci*. **9** (2014) 11 6387.

119. Chen Z., Huang K., Liu S. and Wang H. *Trans. Nonferrous Met. Soc. China* **20** (2010) 12 2309.

120. Zhao H., Li F., Liu X., Xiong W., Chen B., Shao H., Que D., Zhang Z. and Wu Y. *Electrochim. Acta* **166** (2015) 124.

121. Li F., Xiong X., Han L. and Cui J. *Integr. Ferroelectr*. **167** (2015) 1 211.

122. Bai Z., Fan N., Ju Z., Sun C. and Qian Y. *Mater. Lett*. **76** (2012) 124.

123. Xiuqiang X., Dawei S., Bing S., Jinqiang Z., Chengyin W. and Guoxiu W. *Chem. Eur. J*. **20** (2014) 51 17125.

124. Als-Nielsen J. and McMorrow D. *Elements of modern x-ray physics.* 1st ed. John Wiley & Sons, LTD, 2001.

125. Chen JG. *Surf. Sci. Rep*. **30** (1997) 1 1

126. Attwood D. and Sakdinawat A. *X-rays and extreme ultraviolet radiation: Principles and applications* Cambridge University Press; 2016.

127. Hahner G. *Chem. Soc. Rev*. **35** (2006) 12 1244

128. Stöhr J. *NEXAFS spectroscopy.* 1st ed. Springer, 1992.

129. Diaz J., Monteiro OR. and Hussain Z. *Phys. Rev. B* **79** (2008) 9 094201.

130. Yano J. and Yachandra VK. *Photosynth. Res*. **102** (2009) 2-3 241.

131. Erbil A., Cargill GS., Frahm R. and Boehme RF. *Phys. Rev. B* **37** (1988) 5 2450.

132. de Groot FMF., Grioni M., Fuggle JC., Ghijsen J., Sawatzky GA. and Petersen H. *Phys. Rev. B* **40** (1989) 8 5715.

133. Bajt S., Sutton SR. and Delaney JS. *Geochim. Cosmochim. Acta*. **58** (1994) 23 5209.

134. Pickering IJ., George GN., Lewandowski JT. and Jacobson AJ. *J. Am. Chem. Soc*. **115** (1993) 10 4137.

135. Horne CR., Bergmann U., Grush MM., Perera RCC., Ederer DL., Callcott TA., Cairns EJ. and Cramer SP. *J. Phys. Chem. B* **104** (2000) 41 9587.

136. de Groot FMF., Hu ZW., Lopez MF., Kaindl G., Guillot F. and Tronc M. *J. Chem. Phys*. **101** (1994) 8 6570.

137. de Groot FMF. *Physica B* **208-209** (1995) 15-18.

138. de Groot FMF., Fuggle JC., Thole TB. and Sawatzky GA. *Phys. Rev. B* **41** (1990) 2 928.

139. Shin DW., Choi J., Choi W., Cho YS. and Yoon S. *Electrochem. Commun*. **11** (2009) 3 695.

140. Nakai I., Yasaka K., Sasaki H., Terada Y., Ikuta H. and Wakihara M. *J. Power Sources* **97-98** (2001) 412.

141. Okumura T., Fukutsuka T., Matsumoto K., Orikasa Y., Arai H., Ogumi Z. and Uchimoto Y. *Dalton Trans*. **40** (2011) 38 9752.

142. Lee J., Tsai Y., Santhanam R., Hwang BJ., Yang M. and Liu D. *J. Power Sources* **119-121** (2003) 721.

143. Shen CH., Liu RS., Jang LY., Lee JF. and Chen JM. *J. Chin. Chem. Soc*. **49** (2013) 5 841.

144. Ammundsen B., Islam MS., Jones DJ. and Rozière J. *J. Power Sources*. **81-82** (1999) 500.

145. Grush MM., Horne CR., Perera RCC., Ederer DL., Cramer SP., Cairns EJ. and Callcott TA. *Chem. Mater*. **12** (2000) 3 659.

146. Baehtz C., Buhrmester T., Bramnik NN., Nikolowski K. and Ehrenberg H. *Solid State Ionics* **176** (2005) 17 1647.

147. Thackeray MM., David WIF., Bruce PG. and Goodenough JB. *Mater. Res. Bull*. **18** (1983) 4 461.

148. Ouyang CY., Shi SQ., Wang ZX., Li H., Huang XJ., and Chen LQ. *Europhys. Lett*. **67** (2004) 1 28.

149. Yamaguchi H., Yamada A. and Uwe H. *Phys. Rev. B* **58** (1998) 8.

150. Ohzuku T., Kitagawa M. and Hirai T. *J. Electrochem. Soc*. **137** (1990) 3 769.

151. Liu RS., Jang LY., Chen JM., Tsai YC., Hwang YD. and Liu RG. *J. Solid State Chem*. **128** (1997) 2 326.

152. Shinshu F., Kaida S., Nagayama M. and Nitta Y. *J. Power Sources*. **68** (1997) 2 609.

153. Paolone A., Castellano C., Cantelli R., Rousse G. and Masquelier C. *Phys. Rev. B* **68** (2003) 014108.

154. Kanamura K., Naito H., Yao T. and Takehara Z. *J. Mater. Chem*. **6** (1996) 33.

155. Bianchini M., Fauth F., Suard E., Leriche J., Masquelier C. and Croguennec L. *Acta Crystallogr., Sect. B: Struct. Sci.* **71** 2015 688.

156. Bianchini M., Suard E., Croguennec L. and Masquelier C. *J. Phys. Chem. C* **118** (2014) 45 25947.

157. Berg H. and Thomas JO. *Solid State Ionics*. **126** (1999) 3 227.

158. Berg H., Rundlöv H. and Thomas JO. *Solid State Ionics*. **144** (2001) 1 65.

159. Kwon O., Kim M. and Kim K. *J. Power Sources*. **81-82** (1999) 510.

160. Choy J., Kim D., Kwon C., Hwang S. and Kim Y. *J. Power Sources*. **77** (1999) 1 1.

161. Ammundsen B., Jones DJ. and Rozière J. *J. Solid State Chem*. **141** (1998) 1 294.

162. Shiraishi Y., Nakai I., Tsubata T., Himeda T. and Nishikawa F. *J. Solid State Chem*. **133** (1997) 2 587.

163. Braun A., Seifert S., Thiyagarajan P., Cramer SP. and Cairns EJ. *Electrochem. Commun*. **3** (2001) 3 136.

164. Zhuo Z., Olalde-Velasco P., Chin T., Battaglia V., Harris SJ., Pan F. and Yang W. *Appl. Phys. Lett*. **110** (2017) 9 093902.

165. Kobayashi S., Usui T., Ikuta H., Uchimoto Y. and Wakihara M. *J. Am. Ceram. Soc*. **87** (2004) 6 1002.

166. Yoon W., Chung K., Oh K. and Kim K.. *J. Power Sources*. **119-121** (2003) 706.

167. Ammunden B., Jones DJ. and Roziere J. *Chem. Mater*. **8** (1996) 12 2799.

168. Ning F., Xu B., Shi J., Shu H., Wu M., Liu G., Ouyang C. *J. Mater. Chem. A* **5** (2017) 20 9618.

169. Ammundsen B., Islam MS., Jones DJ. and Roziere J. *Mol. Cryst. Liq. Cryst. Sci. Technol., Sect. A* **311** (1998) 1 109.

170. Thackeray MM., Johnson PJ., de Picciotto LA., Bruce PG. and Goodenough JB. *Mater. Res. Bull*. **19** (1984) 2 179.

171. Berg H., Goransson K., Nolang B. and Thomas JO. *J. Mater. Chem*. **9** (1999) 11 2813.

172. Buhrmester T. and Martin M. *Solid State Ionics*. **135** (2000) 1 267.

173. Braun A., Shrout S. and Fowlks AC., Osaisai BA., Seifert S., Granlund E. and Cairns *J. Synchrotron Rad*. **10** (2003) 4 320.

174. Nakai I., Shiraishi Y. and Nishikawa F. *Spectrochim. Acta, Part B* **54** (1999) 1 143.

175. Okumura T., Yamaguchi Y., Shikano M. and Kobayashi H. *J. Mater. Chem. A* **2** (2014) 21 8017.

176. Berg H., Kelder ME. and Thomas JO. *J. Mater. Chem*. **9** (1999) 2 427.

177. Sharma N., Yu D., Zhu Y. and Peterson VK. *Chem. Mater*. **25** (2013) 5 754.

178. Takada T., Akiba E., Izumi F., and Chakoumakos BC. *J. Solid State Chem*. **130** (1997) 1 74.

179. Ammundsen B., Jones DJ., Roziere J. *Chem. Mater*. **10** (1998) 6 1680.

180. Mitsunaga T. *The Rigaku J*. **25** (2009) 1.

181. Kobayashi S. *The Rigaku J*. **26** (2010) 1.

182. Nagao K. and Kagami E. *The Rigaku J*. **27** (2011) 2.

183. Simonelli L., Marini C., Olszewski W., Perez MA., Ramanan N. and Guilera G. *Cogent Phys*. **3** (2006) 1.

184. Settipani DA. *ALD -grown cathode material for thin-film li-ion batteries: Structural and electronic analysis of lithium manganese oxide spinel ($li_xmn_2O_4$) by X-ray absorption spectroscopy*. M.Sc. thesis, University of Rennes, 2017.

185. Senf F., Flechsig U., Eggenstein F., Gudat W., Klein R., Rabus H., Ulm G. *J. Synchrotron Rad*. **5** (1998) 3 780.

186. Lubeck J., Beckhoff B., Fliegauf R., Holfelder I., Hönicke P., Müller M., Pollakowski B., Reinhardt F. and Weser J. *Rev. Sci. Instrum*. **84** (2013) 4 045106.

187. Biesinger MC., Payne BP., Grosvenor AP., Lau LWM., Gerson AR. and Smart RSC. *Appl. Surf. Sci*. **257** (2011) 7 2717.

188. Wyckoff RWG. *Crystal Structures* 1 (1963), 239.

189. Tateishi K., Suda K., du Boulay D., Ishizawa N. and Oishi S. *Acta Crystallogr., Sect. E*. **60** (2004) 18.

190. Ouyang CY., Zeng XM., Sljivancanin Z. Baldereschi A. *J. Phys. Chem. C* **114** (2010) 10 4756.

191. Kim K., Zhu P., Li N., Ma X. and Chen Y. *Carbon* **49** (2011) 5 1745.